Enabling High Performance III-V Thin-Film Photodetectors on Unconventional Surfaces

by

Dejiu Fan

A dissertation submitted in partial fulfillment
of the requirements for the degree of
Doctor of Philosophy
(Electrical Engineering)
in the University of Michigan
2020

Doctoral Committee:

Professor Stephen Forrest, Chair
Assistant Professor Andrej Lenert
Professor Wei Lu
Professor Zetian Mi

Dejiu Fan

fandejiu@umich.edu

ORCID iD: 0000-0002-7374-134X

© Dejiu Fan 2020

To a better world

ACKNOWLEDGEMENTS

The work presented in this thesis could not have been accomplished without the contributions of many others. First, I would like to express my most sincere gratitude to my advisor, Professor Stephen Forrest, for his mentorship during these years. I started as an undergraduate student in his OCM group in 2012. His passion and enthusiasm toward science and engineering inspired me to begin my Ph.D. career in September, 2013. During this six-and-half-year journey, he has shown exceptional patience to my million failures, and always guided me to the positive path with his deep insight and great relish of scientific research. His incentive mentoring of *"Seek and You Shall Find"* has promoted me to become a critical thinker and a qualified researcher. The most important lesson I learned is that the horizon of research is beyond publishing papers and earning a degree; the ultimate accomplishment is to make a better world.

Next, I would like to thank all my mentors and collaborators. Jeramy Zimmerman was my first mentor when I joined the group and I appreciate his great help when instructing me on solution process techniques and organic deposition equipment. I would like to thank Kyusang Lee for being a supportive mentor who introduced me to the growth of III-V materials using MBE and basic inorganic fabrication techniques. I would also like to thank my mentee Byungjun Lee who has collaborated with me on almost all the projects that I have worked on and helped me a great amount on device fabrication and machine maintenance. I am also thankful for the collaboration with Caleb Coburn on hemispherical FPA and organic CCD, Tobias Burger, Sean McSherry, and Andrej Lenert on multiple TPV projects, Xiaozhou Che on multijunction OPV, Xiao Liu on Organic/2D

heterojunction, Xiaheng Huang on ultra-thin OLED, and Xinjing Huang on solution-processed tandem OPV.

I am also grateful to have overlap with many other OCM group members with whom I have spent a lot of enjoyable time, including Greg McGraw, Brian Lassiter, Nana Wang, Kyle Renshaw, Cedric Rolin, Yifan Zhang, Xiaoran Tong, Michael Slootsky, Xiaomi Zhang, Kevin Bergemann, Xin Xiao, Olga Griffith, Ardavan Oskooi, Qi Wang, Jaesang Lee, Anurag Panda, Quinn Burlingame, Yue Qu, Claire Arneson, Kan Ding, Jeffrey Horowitz, Jongchan Kim, Boning Qu, Hafiz Sheriff, Yongxi Li, and Shaocong Hou. Especially, I would like to thank Eva for being supportive and attentive on the administration and logistics. I would also like to acknowledge many of the LNF staff for being great help including Pilar, Dennis, Sandrine, Matt, Brian, Shawn, Kevin, Vishva, etc. In addition, many thanks to my friends Muzhi Wang, Yue Zheng, Tianhua Zhang, Yixing Lu, Fuxi Cai, Shaopin Song, and many others for spending joyful times with me outside the lab.

Finally, I would like to thank my parents and girlfriend for their eternal love and care that encourage me to walk through tough moments during these years. I have been feeling the confidence of *"You'll Never Walk Alone"* with their company and support they have given me along the way and till the end of this journey.

Dejiu Fan

Ann Arbor, MI

March, 2020

TABLE OF CONTENTS

DEDICATION ii

ACKNOWLEDGEMENTS iii

LIST OF TABLES viii

LIST OF FIGURES ix

ABSTRACT xiii

Chapter 1 Introduction 1

1.1. Thesis Overview 1

1.2. Overview of III-V Compound Semiconductors 3

1.2.1. Crystalline Structure of Compound Semiconductors 3

1.2.2. Epitaxial Growth 6

1.3. Optoelectronic Devices 8

1.3.1. LED and Laser 9

1.3.2. Photodetector 10

1.3.2.1. Light Detection 10

1.3.2.2. Energy Harvesting 12

1.4. Device Fabrication 15

1.4.1. Lithography 15

1.4.2. Metal Patterning 16

1.4.3. Etching 17

Chapter 2 Thin Film Technologies and Non-Planar Architectures 21

2.1. Thin-Film Optoelectronics 22

2.1.1. Mechanical Spalling 23

2.1.2. Epitaxial Lift-Off 24

2.1.3. Laser Lift-Off 26
2.1.4. 2D Material-Assisted Lift-Off 27
2.2. Non-Planar Architectures 28
2.2.1. Developable vs. Non-Developable Surfaces 29
2.2.2. Methods for Deformation 31
2.2.2.1. Rolling 31
2.2.2.2. Folding 32
2.2.2.3. Curving 33
2.2.2.4. Buckling 34
2.2.3. Bio-Inspired Artificial Imaging Systems 35
2.2.3.1. Compound Eye Type Imaging Systems 36
2.2.3.2. Single-Chambered Eye Type Imaging Systems 38
2.3. Summary 40
Chapter 3 A Flexible Thin-Film InGaAs Photodiode Focal Plane Array 47
3.1. Introduction 47
3.2. Photodiode Focal Plane Array Fabrication 49
3.3. Photodiode Characterization 54
3.4. Array Yield and Reliability 57
3.5. Application 1: 2π Imager 60
3.6. Application 2: High Resolution Spectroscopy 63
3.7. Conclusion 70
Chapter 4 A Retina-Like Hemispherical Focal Plane Array 75
4.1. Introduction 76
4.2. Hemispherical Focal Plane Array (HFPA) Fabrication 78
4.3. Device characterization 87
4.4. Imaging with HFPA 91
4.5. Conclusion 96

Chapter 5 Thin-Film Architectures with High Spectral Selectivity for Thermophotovoltaic Cells 101

5.1. Introduction 102

5.2. Device Fabrication 104

5.3. Optical Properties 106

5.4. Energy Conversion Simulation 108

5.5. Evaluating Strategies for Enhanced Selectivity 110

5.6. Structure Optimization 112

5.7. Conclusion 113

Chapter 6 Nearly Perfect Photon Utilization in an Air-Bridge Thermophotovoltaic Cell 118

6.1. Introduction 119

6.2. Device Fabrication 122

6.3. Spectral Properties 125

6.4. Power Conversion Efficiency 129

6.5. Conclusion 137

Chapter 7 Conclusion and Outlook 142

7.1. Conclusion 142

7.2. A High Throughput, Linear Molecular Beam Epitaxy System 143

7.3. Tandem Thermophotovoltaic Cell 149

7.4. Thin-Film Air-Bridge Si Thermophotovoltaic Cell 151

LIST OF TABLES

Table 5.1: Optimized architecture and performance for InGaAs structures (Th = 1500 K)....... 112

Table 6.1: Parameters of Au reflector cell and air-bridge cell under illuminations. 133

Table 7.1: Calculated out-of-band power reflectance of the air-bridge Si TPV cell with 2 μm Si epi for various air cavity thicknesses when operated using a 1500 K blackbody source. 152

LIST OF FIGURES

Figure 1.1: Interatomic energy in a solid. 4
Figure 1.2: Types of solids based on periodic arrangement of atoms. 5
Figure 1.3: Zincblende lattice unit cell (GaAs). 5
Figure 1.4: Schematics of an MBE chamber. 7
Figure 1.5: Energy gap vs. lattice constant for some common elementary and binary semiconductors. 8
Figure 1.6: Schematic of a photoconductor. 10
Figure 1.7: Schematic of a *p-i-n* photodiode. 12
Figure 1.8: Schematic to compare non-concentrator solar PV and TPV conversion. 14
Figure 1.9: Schematic of (left) an evaporation system and (right) a sputtering system. 17
Figure 2.1: Schematic demonstration of light absorption. 23
Figure 2.2: Illustration of mechanical spalling process. 24
Figure 2.3: Illustration of epitaxial lift-off (ELO) process. 25
Figure 2.4: Illustration of laser lift-off (LLO) process. 27
Figure 2.5: Illustration of 2D assisted lift-off process. 28
Figure 2.6: Schematic illustration of developable deformation vs. non-developable deformation process. 30
Figure 2.7: Illustration of the rolling process based on heteroepitaxial crystalline bilayer. 32
Figure 2.8: Illustration of folding process. 33
Figure 2.9: Illustration of the curving process based on transfer printing. 34
Figure 2.10: Illustration of the buckling process. 35
Figure 2.11: Schematic illustrations of the major components of bio-inspired imaging systems. 36
Figure 2.12: Demonstrations of artificial compound eye type imaging systems. 37
Figure 2.13: Demonstrations of artificial single-chambered eye type imaging systems. 39
Figure 3.1: Schematic of fabrication flow of *p-i-n* thin-film photodiode. 50

Figure 3.2: Process flow for fabrication of the thin-film InGaAs *p-i-n* photodiode array........... 53
Figure 3.3: Images of an 8×100 thin-film InGaAs photodiode array fabricated on flexible Kapton® foil. 54
Figure 3.4: The normalized simulated optical intensity distribution. 55
Figure 3.5: Simulated and measured external quantum efficiencies. 56
Figure 3.6: Histograms of dark current of detectors. 57
Figure 3.7: Image of the 10×10 InGaAs photodiode array fabricated on Si and Kapton substrates. 58
Figure 3.8: Dark current and *EQE* mapping of 10×10 InGaAs array. 59
Figure 3.9: Reliability Tests... 60
Figure 3.10: Field of view (FOV) measurement setup. 61
Figure 3.11: Photocurrent map of laser output profiles on a convex cylindrical 8×100 photodiode array. 62
Figure 3.12: Imaging Test.. 63
Figure 3.13: Spectroscopy Test.. 65
Figure 3.14: Shape mismatch vs. the position of the array. 65
Figure 3.15: Resolution Improvement. 67
Figure 3.16: Wavelength coverage comparison... 68
Figure 4.1: Microscopic image of photodiodes array connected in rows. 79
Figure 4.2: Schematic illustration of the key steps of fabricating a hemispherical photodiode array. 80
Figure 4.3: Simulated meridional and circumferential strain. 81
Figure 4.4: Schematic illustration of the key steps of deformation. 82
Figure 4.5: SEM image of individual pixels around the center of a fully fabricated (dummy) hemispherical focal plane array. 83
Figure 4.6: Schematic illustration of transferring a second layer of detector rows. 85
Figure 4.7: Metalized Kapton® pads for column connections. 86
Figure 4.8: Schematics of the batch fabrication of multiple hemispherical focal plane arrays (FPAs). 86
Figure 4.9: Images of a 15×15 pixel GaAs *p-n* junction FPA fabricated on a concave hemispherical surface.. 87

Figure 4.10: Schematic of a single pixel in the array. 88
Figure 4.11: *EQE* and *I-V* characteristics. 89
Figure 4.12: Dark current mapping.. 90
Figure 4.13: Photocurrent vs. input optical power of a single photodetector. 91
Figure 4.14: Ray tracing simulation.. 92
Figure 4.15: Ray tracing simulation spot diagram of a curved image surface using ZeMax. 93
Figure 4.16: Photograph of the HFPA mounted on testing stage. 94
Figure 4.17: Schematics of the image acquisition mechanism. 95
Figure 4.18: Normalized photocurrent map. 96
Figure 5.1: Energy flows in a parallel plate TPV system with sub-bandgap photon recycle. 103
Figure 5.2: Schematics of the thin-film structures. 105
Figure 5.3: Simulated and measured absorption spectra. 107
Figure 5.4: Measured optical response of MgF_2/ZnSe ARC on Au. 108
Figure 5.5: Combined structure. 113
Figure 6.1: Photon utilization in air-bridge thermophotovoltaics (TPVs). 121
Figure 6.2: Air-bridge TPV cell fabrication. 122
Figure 6.3: Structure of the air-bridge cell. 124
Figure 6.4: Air-bridge bowing. 125
Figure 6.5: Spectral properties of the Au reflector and the air-bridge TPVs. 126
Figure 6.6: Absorption spectra of Au reflector and air-bridge TPV. 126
Figure 6.7: External quantum efficiency (EQE) of the air-bridge cell. 127
Figure 6.8: Spectral efficiency. 129
Figure 6.9: Schematic of the TPV efficiency measurement setup. 131
Figure 6.10: TPV power conversion efficiency (PCE) 132
Figure 6.11: Current density (*J*)-voltage (V) characteristics of the air-bridge TPV measured under 1500 K SiC globar illumination with varying view factors. 132
Figure 6.12: *J-V* characteristics of the air-bridge TPV under dark condition. 134
Figure 6.13: *J-V* and power density-voltage curves of the air-bridge TPV at maximum measured PCE. 135
Figure 6.14: Open circuit voltage and fill factor. 136
Figure 6.15: Power conversion efficiency (*PCE*) vs. source temperature (*T*). 137

Figure 7.1: Schematic illustration of a conventional production scale MBE vs. a linear MBE. 144
Figure 7.2: Schematic illustration of a rack and pinion linear transfer system.......................... 146
Figure 7.3: Schematic illustration of a linear transfer system. 147
Figure 7.4: An analysis of an inverted single junction GaAs photovoltaic cell. 148
Figure 7.5: InGaAsP / InGaAs tandem TPV design. 150
Figure 7.6: Schematic of an air-bridge Si TPV cell. 152
Figure 7.7: Simulated spectral properties of the air-bridge Si TPV cell with 2 µm Si epi and 500 nm air gap. 152

ABSTRACT

High performance optoelectronic devices made of III-V compound semiconductors are preferred over elemental semiconductors due to their superior optical and electronic properties. With the development of semiconductor fabrication technology, thin-film optoelectronics on *unconventional surfaces* have drawn attention due to the benefits of enhanced absorption/reflection, reduced fabrication cost, superior mechanical flexibility, opportunities for integration with dissimilar materials, etc.

In this thesis, we demonstrate novel fabrication techniques that transfer the III-V optoelectronic devices, especially high-performance photodetectors focal plane arrays, from their bulky and rigid crystalline substrates, to unconventional lightweight, flexible, conformal, and non-developable surfaces without performance degradation. The demonstrations include a cylindrical and bendable 8×100 thin-film $In_{0.53}Ga_{0.47}As$ *p-i-n* photodiode array fabricated on a thin flexible plastic foil, and a hemispherical GaAs *p-n* junction focal plane array that mimics the size, form, and function of the human eye.

In addition, we integrate an energy harvesting photodetector comprising an InGaAs-based thin-film thermophotovoltaic (TPV) cell with low index dielectrics and even air for enhanced out-of-band photon recycling. Specifically, an unconventional TPV cell is fabricated over an air cavity, showing 8% (absolute) power conversion efficiency improvement compared to conventional thin-film TPV cells, leading to a record-high TPV power conversion efficiency of > 30% at 1500K emitter temperature. The demonstrated high performance III-V thin-film photodetectors on

unconventional surfaces unlock possibilities for future optoelectronics that are beyond current planar and lattice-matched substrates, and provide paths to their ubiquitous applications.

Chapter 1

Introduction

III-V compound semiconductors, as the name suggests, are semiconductor materials that are made from group III and group V elements in the periodic table. These elements are covalently bonded together to form crystalline structures. Compound semiconductors offers many superior properties over conventional elemental semiconductor materials (Si, in particular) due to their direct bandgap, energy tunability and strong light absorption. Therefore, high performance optoelectronic components such as photodetectors, light emitting diodes (LEDs), semiconductor lasers, etc., are mostly made of compound semiconductors. Photodetectors, in particular, are devices that convert light to electricity. It can be divided into two categories: light detection devices (photoconductors, photodiodes, focal plane arrays, etc.) and energy harvesting devices (photovoltaics, thermophotovoltaics, etc.). Most optoelectronic devices require combined or sequenced processing techniques to be produced. This chapter gives a brief introduction to III-V compound semiconductors, their growth methods, applications of optoelectronic devices, and their processing techniques.

1.1. Thesis Overview

High performance optoelectronic devices made of III-V compound semiconductors such as photodetectors, light emitting diodes (LEDs), semiconductor lasers, etc. have been widely used

in all aspects of our daily life. The development of new technologies during recent years, however, posts more demands on optoelectronics besides performance. Examples are wearable sensing devices[1–3], conformal light absorption modules[4–7], and head-up and virtual reality (VR) displays that are often needed on curved or folded surfaces[8]. Optoelectronic devices that are lightweight, flexible, stretchable, and even bio-compatible without loss of performance are urgent needed in these applications. One of the critical challenges facing current epitaxial growths and device fabrication techniques of III-V compound semiconductors is the requirement of processing on conventional crystalline substrates. The commercially available substrates are limited to GaAs, InP, GaN, GaSb, and InAs. Devices fabricated on these *conventional surfaces* are usually bulky, rigid, brittle, and expensive. The demand for improved optoelectronic devices necessitates thin-film optoelectronics on *unconventional surfaces* with mechanical flexibility, conformability, and opportunity for integration with other materials such as metals or dielectrics for enhanced performance, and without their parent growth substrates. Thin-film optoelectronics and current techniques to lift-off, transfer, and deform the devices, as well as the most intensively studied detector applications that can benefit from fabrication on non-planar architectures, bio-inspired artificial imaging systems, will be discussed in Chapter 2.

The major goal of this thesis is to focus on potential solutions to address the above challenges and enable high performance III-V thin-film detectors on *unconventional surfaces*. The first part is to develop methods that shape compound semiconductor thin films into non-planar architectures. Specifically, application of photodiode focal plane arrays are demonstrated on both developable flexible and non-developable hemispherical surfaces. We first demonstrate a flexible thin-film InGaAs focal plane array fabricated on thin Kapton substrates that can be curved to a very small radius, with approaching 100% quantum efficiency and nearly perfect fabrication yield.

Furthermore, we demonstrate a general approach for fabricating optoelectronic devices on non-developable surfaces that overcomes the topological change by introducing shear-slip of thin-film components relative to the distorting substrate. In particular, we demonstrate retina-like imagers that allow for a topological transformation from a plane to a hemisphere without changing the relative positions of the pixels from that initially laid out on a planar surface. The second part will be focused on integrating compound semiconductor thin films to dissimilar materials such as dielectrics and even air to gain more optical advantages, with the application to TPV as a demonstration. By transferring the thin-film InGaAs structures on MgF_2 dielectric spacer, exceptional spectral selectivity is achieved with a predicted TPV power conversion efficiency above 50%. We further demonstrate nearly perfect photon utilization by suspending a thin-film InGaAs TPV cell over wide air cavities. An 8% absolute gain in efficiency compared to the state-of-the-art TPV architecture and a record-high power conversion efficiency exceeding 31% is achieved with this TPV-on-air structure. Lastly, we summarize the results, propose a high-throughput III-V materials growth system for the production cost reduction, and preview some of the potential applications including multijunction, and Si-based TPV cells.

1.2. Overview of III-V Compound Semiconductors

1.2.1. Crystalline Structure of Compound Semiconductors

In the solid state, atoms are held together by two types of interatomic bonding forces: attractive and repulsive forces. As can be seen from Figure 1.1, attractive (Coulombic) forces dominate when atoms are separated by large distances, while when separations are small, repulsive forces dominate. At equilibrium, these two forces balance each other, resulting in a zero net force and a stable atomic spacing[9]. To break the bonding, it requires a minimum energy of E_b, which is

the binding energy of the system. In III-V compound semiconductors solid, the bonding is mostly covalent, which arises from electron sharing between neighboring atoms, and partially ionic, when one atom yields outer shell electrons to its neighbor[9].

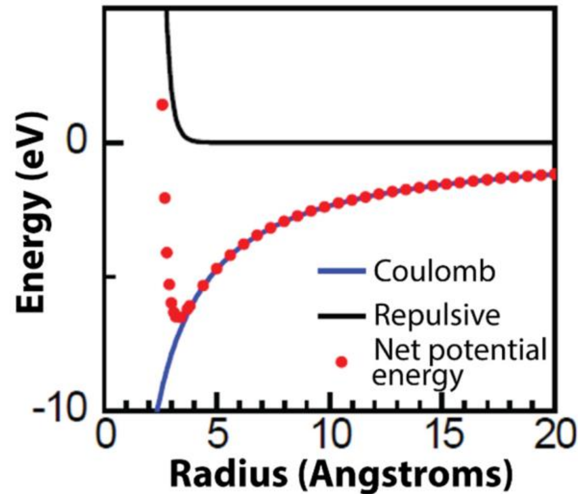

Figure 1.1: Interatomic energy in a solid.

Attractive, repulsive, and total energy as a function of interatomic distance. Reproduced from reference 17.

Depending on the periodic arrangement of atoms, solids can be classified into three types: crystalline, polycrystalline, and amorphous (Figure 1.2). The atoms in crystalline solids exhibit long range periodicity. If the atoms have a periodic arrangement over a small region, and show distinct boundaries from other regions, the solids are polycrystalline. If the atoms have no periodicity, the solids are amorphous[9].

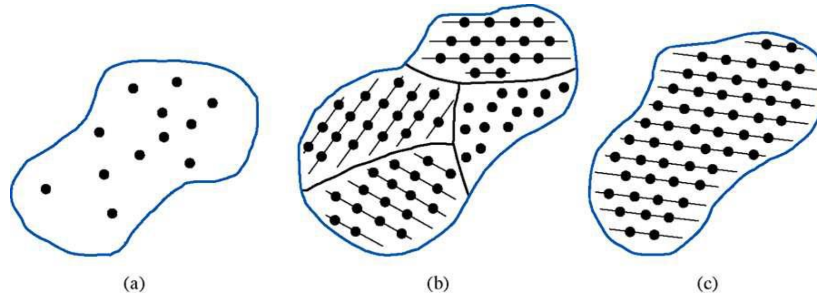

Figure 1.2: Types of solids based on periodic arrangement of atoms.
(a) Amorphous, (b) polycrystalline, and (c) crystalline. Reproduced from reference 10.

Most of III-V compound semiconductors are crystalline solids with a zincblende structure, which is essentially identical to the diamond structure of Si or Ge, except that lattice sites in III-V semiconductors are separated equally between different atoms. For example, in GaAs, as shown in Figure 1.3, Ga atoms occupy one of the two interpenetrating face-centered cubic (fcc) sublattices, while As atoms fill up the other fcc sublattice[10]. Figure 1.3 shows a GaAs zincblende lattice unit cell, which is a small portion of a GaAs crystal that could be used to reproduce the entire crystal[10]. The length of a side of the smallest unit cell is called the lattice constant, *a*. The lattice structure is important in determining the crystal potential and band structure of the material, which in turn determines its electronic and optical properties[9].

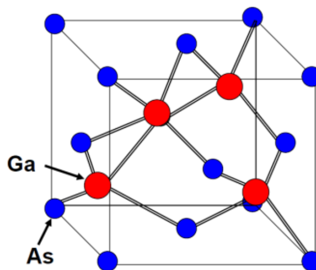

Figure 1.3: Zincblende lattice unit cell (GaAs).
Reproduced from reference 10.

1.2.2. Epitaxial Growth

The crystalline materials can be synthesized through bulk crystal growth or epitaxial crystal growth[9]. Bulk crystal growth is mainly used to prepare substrates. We will be focused on epitaxial material growth of III-V semiconductors in this section. The term "epitaxy" comes from the Greek root "*epi*", meaning "above" and "*taxis*", meaning "in the form of". Epitaxial growth refers to the oriented and extended growth of a single crystal over a similar single crystal substrate[9]. The first successful epitaxial process used to grow compound semiconductors is liquid phase epitaxy (LPE). It grows a crystal layer on a parent substrate by participation of a crystalline phase from a saturated solution of the constituents. Vapor phase epitaxy (VPE), or chemical vapor deposition (CVD) is another epitaxial growth technique that forms crystals on substrates through chemical reactions of gas source constituents. The VPE processes for compound semiconductors can be categorized in halide, hydride, and metal-organic CVD processes.

Besides LPE and VPE, molecular beam epitaxy (MBE) is another important epitaxial crystal growth technique. In fact, most of the compound semiconductor samples that are the focus of this thesis are grown using MBE. MBE is a thermal evaporation process under ultra-high vacuum (UHV), where source molecular beams from Knudsen effusion cells are directionally incident on the substrate, react with the surface of the substrate material, and epitaxially grow new crystal layers. Elemental materials are usually used as group III sources (Al, Ga, and In), while As, P, or compound GaP (solid source MBE), and gaseous AsH_3 and PH_3 (gas source MBE) are used as group V sources. Because of vacuum deposition, MBE growth is accomplished under nonequilibrium conditions and is principally governed by surface kinetic processes[11]. MBE has the advantages of precise control of the beam fluxes using beam flux monitor, and in situ surface

diagnosis by employing methods like Reflection High-Energy Electron Diffraction (RHEED)[11]. Figure 1.4 presents a schematic of an MBE chamber.

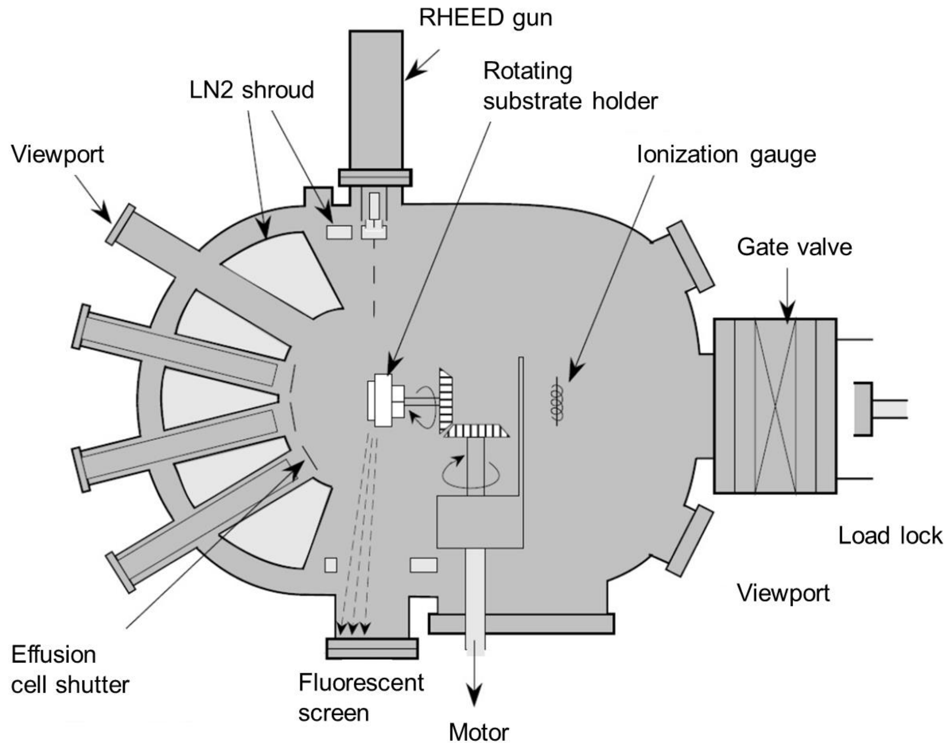

Figure 1.4: Schematics of an MBE chamber.
Reproduced from reference 12.

Due to the precise control of the constituent species, it is possible to epitaxially grow alloy semiconductors with various group III and group V compositions using the above techniques. Figure 1.5 depicts the energy gaps and lattice constants for some common elementary semiconductors, and binary and ternary III-V compound semiconductors. The different alloy compositions of these binary, ternary, and even quaternary compounds are extremely important to realize high performance optoelectronic devices. With engineered compositions, III-V compound semiconductors have enabled LEDs and lasers that illuminate a wide range of wavelengths,

detectors that are sensitive to visible and infrared light for imaging and optical communication, and photovoltaic cells that harvest energy from radiation sources with varying temperatures.

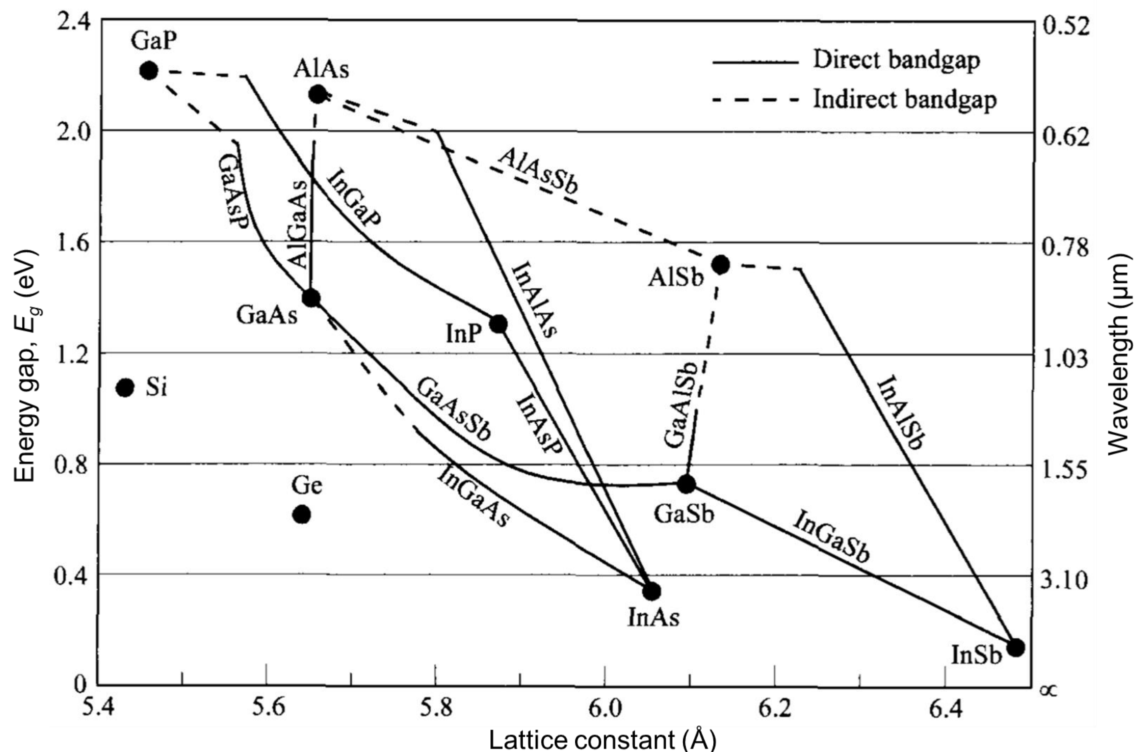

Figure 1.5: Energy gap vs. lattice constant for some common elementary and binary semiconductors. Reproduced from reference 13.

1.3. Optoelectronic Devices

Optoelectronic devices exploit the interaction of electronic processes with light, accompanied by energy conversion from electrical to optical phenomena or vice versa[9]. Although Si is the most widely used elemental semiconductor material in the electronics industry, its indirect bandgap limits its capability for electron-photon interactions. Direct bandgap III-V compound semiconductors are especially suitable for making such devices due to their flexible bandgap-

tuning and strong light absorption/emission abilities over Si. Here, we will introduce some of the optoelectronic applications accessible to III-V compound semiconductors.

1.3.1. LED and Laser

The LED is an optoelectronic device that emits photons at near bandgap energy through electroluminescence, in which a large population of electrons and holes are injected through contacts under forward bias to the active materials. The charge pair then radiatively recombines[9]. The devices usually have heterojunction structures, and the emission wavelengths are mainly determined by the bandgap energy of the active materials. Conventional As and P based materials are often employed in LEDs to achieve visible (GaP-green, AlInGaP-green, GaAsP-red, AlGaAs-red) and infrared (InGaAs, InGaAsP) emission. Recently, GaN based blue LEDs enable the applications for efficient displays and lighting.

Semiconductor junction lasers are another important optoelectronic device that are widely used in high intensity illumination, navigation, and fiber optical communications. They operate similar to an LED by carrier injection to active materials with homo or heterojunction structures, but in addition, they require stimulated emission due to population inversion rather than spontaneous emission and optical feedback provided by reflective mirrors[9]. Heterojunction structures are often employed to reduce the threshold of lasing, while quantum well or multiple quantum well structures improve the gain by enhancing the overlap between the optical modes and gain medium. For a specific active material, the emission wavelength can also be tuned by modifying the width and the depth of the quantum wells. External mirrors are usually not required in semiconductor diode lasers[9], since the cleaved sidewall in edge emitting lasers, or the atomically flat epitaxial surfaces composed of multiple pairs of compound semiconductor layers with

different refractive indices to form distributed Bragg reflectors (DBR) in vertical-cavity surface emitting lasers (VCSELs), can provide enough reflection to form the cavity.

1.3.2. Photodetector

1.3.2.1. Light Detection

The photodetector is another important optoelectronic application that absorbs light and generates electricity. Depending on specific applications, photodetectors can operate under voltage bias for light detection or under photovoltaic mode (no external bias) for energy harvesting purposes. There are, in general, four types of light detection photodetectors: photoconductors, junction photodiodes, avalanche photodiodes (APD), and phototransistors. The photoconductor is the simplest light detection device (Figure 1.6). It operates based on the increased conductivity in the semiconductor absorption region under illumination. With an applied a voltage, the photogenerated carriers are collected at the opposite contacts.

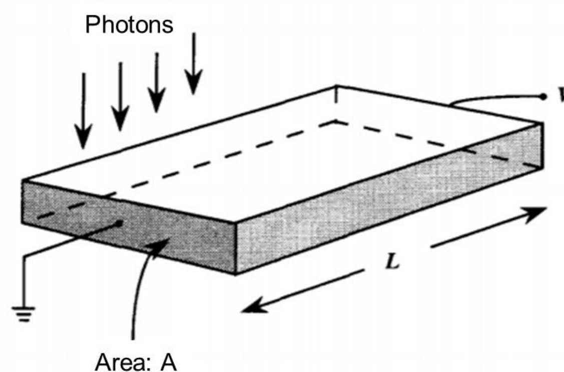

Figure 1.6: Schematic of a photoconductor.

Reproduced from reference 12.

The junction photodiode is the most widely used photodetection device in countless applications such as imaging, spectroscopy, optical communication, etc. It can be based on *p-n* or *p-i-n* junctions with homo or heterojunction structures, and sensitive to the spectral range from the ultraviolet to the far infrared depending on the semiconductor materials used. The operation is also simple. Upon proper illumination, photoexcited carriers in the absorption region of a *p-n* junction are diffused to the depletion region, or drift in the depletion region under an electric field (in a *p-i-n* junction), and are subsequently collected at the opposite contacts under reverse bias.

Figure 1.7 shows a schematic of a *p-i-n* photodiode and its operation. The fully depleted intrinsic, or *i*-region, is sandwiched between highly doped *p*- and *n*-regions. Under reverse voltage with no illumination, the dark saturation current is low due to the low free carrier density and in the *i*-region. When photons impinge on the device, they are absorbed mostly in the *i*-region and excite free carriers. These photoexcited carriers are then rapidly swept out to the contacts due to the high electric field in the depletion region and generate photocurrent. The *p-i-n* photodiode can be very sensitive to small light signals due to its low dark current. The thickness of the *i*-region can be tailored for applications that require fast operational speed up to 10 GHz (a thin *i*-region)[12], or high quantum efficiency up to 100% (a thick *i*-region)[9].

The avalanche photodiode is a reverse-biased *p-n* junction that operates at voltages close to breakdown voltage. It uses the impact ionization or avalanche process to obtain very high gain so that extremely low levels of light can be detected[12]. The phototransistor, as the name suggests, is a bipolar transistor excited by external optical signals. It can have high gain through the internal bipolar transistor action. Compared to an APD, the phototransistor eliminates the high voltage required and high noise associated with avalanche, yet provides reasonable photocurrent gain[13].

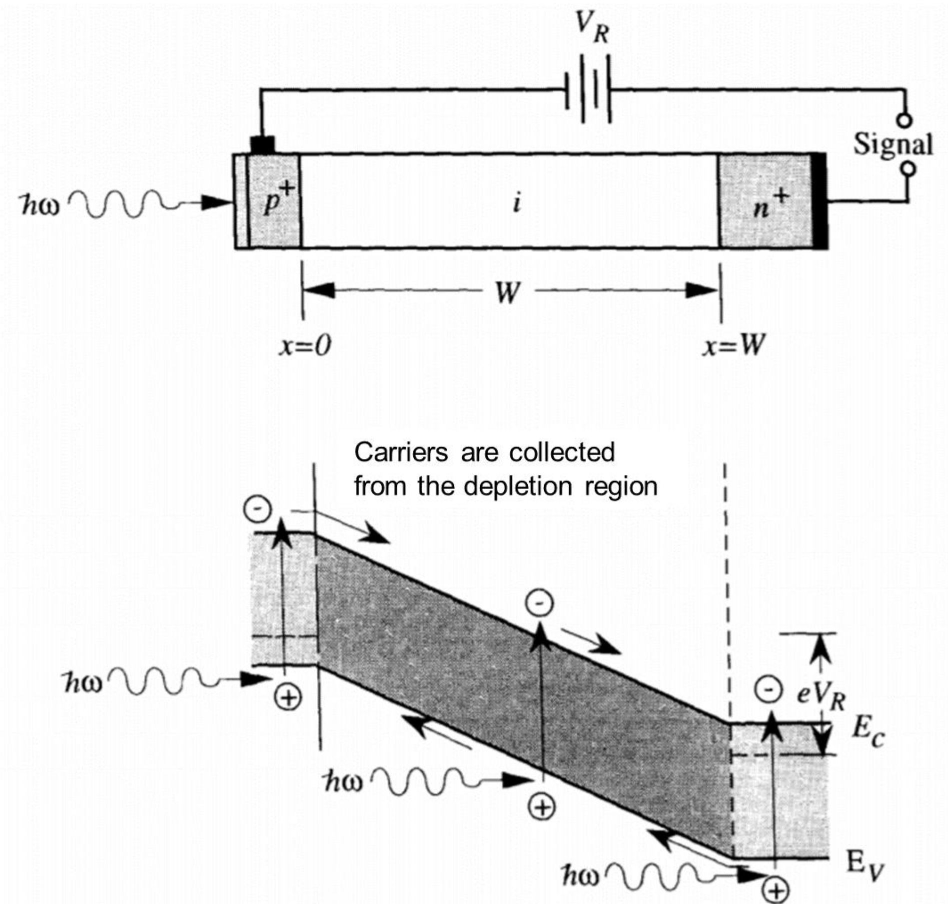

Figure 1.7: Schematic of a *p-i-n* photodiode.

Reproduced from reference 12.

1.3.2.2. Energy Harvesting

Another important type of photodetector is the energy harvesting photovoltaic (PV) cells that operate in the photovoltaic mode (no applied voltage), and convert optical energy to electrical energy. The cells are large surface area *p-n* junctions that receive radiation from high temperature sources. The photoexcited minority carriers diffuse to the junction and are collected to deliver power to an external load. The most widely used PV cells are the well-known solar cells that collect photons radiated from the sun to generate electricity. Although over 95% of solar cells in the global market employ Si due to its low production cost, solar cells made of compound semiconductors

are considered to be the best materials for high efficiency solar energy conversion due to their bandgap matching to the solar spectrum and high mobilities and lifetimes of charge carriers[9]. In addition, the bandgaps of compound semiconductors can be tuned to harvest energy from different parts of the solar spectrum, which enables the stacking of multiple single-junction cells to minimize thermalization loss. A power conversion efficiency of 47.1% has been achieved in a six-junction cell composed of AlGaInP/AlGaAs/GaAs/InGaAs under 143 suns illumination, representing the highest solar power conversion efficiency to date among all solar cell technologies[14].

Thermophotovoltaic (TPV) cells are a special type of PV cells that generate electricity from the radiation of high-temperature thermal sources. The key differences between solar cells and TPV cells are the source temperature and the geometry[15]. Figure 1.8 shows a schematic to compare non-concentrator solar PV and TPV conversion. Solar cells utilize the radiation from the sun, which is approximated by a 5800 K blackbody radiation 150×10^9 meters from the earth, while in a TPV system, a variety of heat sources (chemical, nuclear, solar, waste heat energy, etc.) are employed to heat up thermal radiators (SiC, micro-structured tungsten, etc.) to temperature ranging from 1300 to 2000 K[15]. The emission spectra of these radiators are mostly in the infrared, which requires TPV cells to employ low-bandgap absorption materials such as InGaAs, GaSb, InAs, etc. to achieve high efficiency. Because the TPV cell can be located very close to the radiator (less then several centimeters), it is possible to achieve very high output electrical power density (1 to 100 W/cm^2) compared to that of solar cells (0.02 to 0.04 W/cm^2), which only collect a small portion of the solar radiation. TPV cells have another advantage over solar cells through spectral control to recycle photons with energies below the cell bandgap (out-of-band radiation). In a solar PV cell, out-of-band radiation energy is lost, while in a TPV cell, the radiation of the emitters can be

engineered to spectrally match the absorption spectra of the TPV cell in accordance with the cell bandgap[15], Thus, the out-of-band radiation can be recovered to improve the efficiency. Spectral control can be achieved by suppressing out-of-band radiation from the emitter (the selective emission method), or by reflecting the low-energy photons from the TPV cells back to the emitter (the selective absorption method) using an infrared front surface filter, back surface reflector, etc. The latter has enabled the TPV power conversion efficiency of > 30%.

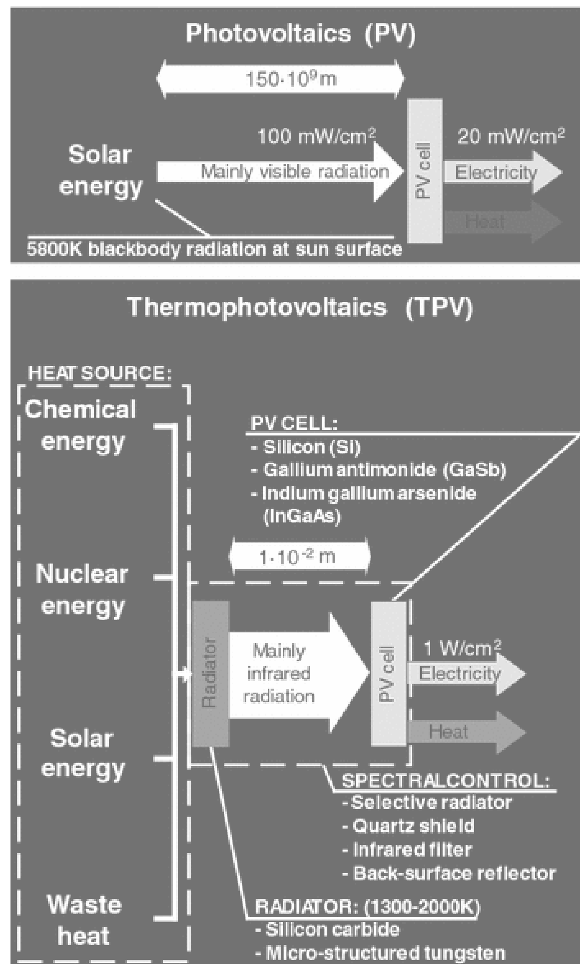

Figure 1.8: Schematic to compare non-concentrator solar PV and TPV conversion.
Reproduced from reference 15.

1.4. Device Fabrication

Fabrication of III-V compound semiconductor devices after the epitaxial growth generally involves lithography, metal or dielectric deposition, wet or plasma etching, annealing, packaging, etc. These steps are, in general, very similar to those used in the Si integrated circuit (IC) industry. This section gives a brief introduction to these techniques, and processes used to fabricate most optoelectronic devices.

1.4.1. Lithography

Lithography is the universal first step to pattern features. It starts with the application of photoresists (PRs) on the epitaxial surface. PRs are mostly organic polymers whose chemical properties or molecular weight change after exposure to radiation (photons, electrons, or ions)[16]. Usually, liquid PR is spin-coated to uniformly cover the wafer surface and soft-baked to remove most solvents and improve adhesion to the wafer by relieving film sheer stress from the spinning process[16]. Then, optical radiation (usually ultra-violet) is incident on the wafer through an optical shadow mask with pre-defined features to expose the PR. In positive PR, for example, the exposure causes chemical transformation (carboxylic acid formation) so that the exposed area can be selectively removed by developer (base solutions). The features are thus transferred from the mask to the PR. For patterning small features, it usually requires a post exposure baking step before developing to reduce the standing wave patterns on the sidewall of the exposed PR caused by reflective surfaces underneath. Finally, a post development bake is required to improve the adhesion, etching resistance, and prevent the swelling of the PR.

1.4.2. Metal Patterning

Most III-V optoelectronic devices have vertical junction configurations, and thus require top and bottom ohmic contacts. One of the unique distinctions of III-V processing from that of Si, is that metal contacts are rarely patterned by chemical etching due to very low etching selectivity between metal etchants (mixture of acids) and III-V compounds, and the difficulty of etching multiple layers of metals (Ti/Pt/Au for *p*-type and Au/Ge/Ni for *n*-type contacts)[9]. Metal patterns are, therefore, defined through the PR lift-off process. This is done by photolithographically patterning the PR to expose the area where the metals are to be deposited, deposit metals over the entire wafer, and dissolve the PR to lift off the excessive metal by soaking in organic solvents. The lift-off process usually requires a double-layer PR structure because the edge profile of the patterned metals is highly sensitive to that of the patterned PR. A thin lift-off resist (LOR) layer is often needed beneath the regular PR to create a slight development undercut around the exposed feature.

Metals can be deposited using vacuum thermal evaporation (VTE), e-beam evaporation, or sputtering. In VTE deposition, metals to be deposited are placed in boats or crucibles, resistively heated through filaments, and subsequently melted and vaporized. E-beam evaporation is similar to VTE, while source heating is achieved through ejection of high energy electron beams directly toward the source materials. These metal sources are usually evaporated in high vacuum chambers ($< 10^{-5}$ torr) such that mean free path of the atomic fluxes exceed the chamber dimensions, resulting in a highly directional line-of-sight deposition on the target wafers (Figure 1.9 (left)). The deposition rate, limited by the emitted flux of the source and the geometry of the target, is usually low (<10 Å/s). Because the deposition rate is proportional to the arrival angle of the vaporized atoms (when surface migration is low), the step-coverage of VTE and e-beam evaporation is not

ideal. This issue, however, can be alleviated through planetary rotation (rotation and spin, to improve line-of-sight) or substrate heating (to improve surface mobility of adatoms).

Sputtering is another commonly used deposition technique. Generated by high energy plasma, ionized Ar, O_2, or N_2 gases eject atoms from a source target, which subsequently travel through the plasma to deposit on the wafers (Figure 1.9 (Right)). Compared to evaporation, sputtering provides better step-coverage due to less directional source flux, and more surface diffusion induced by ion collisions. It also provides better material coverage uniformity over large areas and a more controlled alloy composition by co-deposition process. Ion bombardment, however, may cause damage to the wafer.

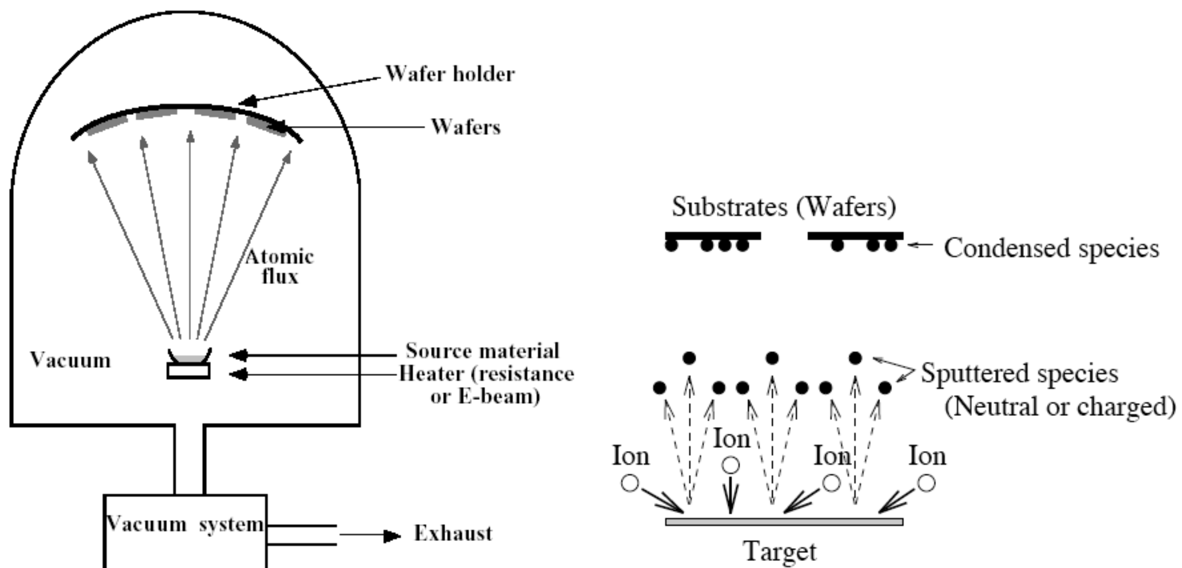

Figure 1.9: Schematic of (left) an evaporation system and (right) a sputtering system.
Reproduced from reference 16.

1.4.3. Etching

Mesa etching is an important step to define the device area and isolate multiple devices. This can be done by either wet or plasma etching. Wet etching uses a chemical solution to remove

epitaxial device layers. The reactants in the wet etchant are transported to the wafer surface and involved in chemical reactions with the surface material. The etch products are then desorbed from the surface and transported into solution[16]. Depending on the composition of etchant mixtures, the etching can be highly selective between different materials. In addition, wet etching can be batch-processed with a large number of wafers for high-throughput and low-cost production. When small and high aspect ratio features are required, however, wet etching is not the best choice because it is usually an isotropic etching process that undercuts the layer underneath the PR mask, resulting in a loss of resolution in the etched pattern. Typical wet etchants for GaAs and InGaAs compounds are H_3PO_4:H_2O_2:H_2O and citric acid:H_2O_2, while H_3PO_4:HCl and HCl:H_2O are typical wet etchants for InP and AlInP compounds.

Dry plasma etching, on the other hand, provides more directional anisotropic etching using plasma. It is similar to sputtering replacing the source target with the target substrate to be etched. The etching process can be accelerated by reactive ion etching (RIE), which utilizes ionized gases to chemically react with the materials to be removed. In this case, both chemical (isotropic) and physical (anisotropic, ion bombardment) etching do not always act independently. Ion bombardment enhances steps in chemical etching such as surface adsorption, etching reaction, and formation or removal of byproducts, while chemical etching byproducts act as inhibitors to physical etching[16]. The combined processes in RIE result in increased etching rate, anisotropy, and selectivity.

CHAPTER 1

Bibliography

1. Miyamoto, A. *et al.* Inflammation-free, gas-permeable, lightweight, stretchable on-skin electronics with nanomeshes. *Nat. Nanotechnol.* **12**, 907–913 (2017).

2. Someya, T. *et al.* A large-area, flexible pressure sensor matrix with organic field-effect transistors for artificial skin applications. *Proc. Natl. Acad. Sci.* **101**, 9966–9970 (2004).

3. Someya, T. *et al.* Conformable, flexible, large-area networks of pressure and thermal sensors with organic transistor active matrixes. *Proc. Natl. Acad. Sci.* **102**, 12321–12325 (2005).

4. Xu, X. *et al.* Thermally stable, highly efficient, ultraflexible organic photovoltaics. *Proc. Natl. Acad. Sci. U. S. A.* **115**, 4589–4594 (2018).

5. Park, S. *et al.* Ultraflexible Near-Infrared Organic Photodetectors for Conformal Photoplethysmogram Sensors. *Adv. Mater.* **30**, 1802359 (2018).

6. Park, S. *et al.* Self-powered ultra-flexible electronics via nano-grating-patterned organic photovoltaics. *Nature* **561**, 516–521 (2018).

7. Wu, Y. L. *et al.* Low-Power Monolithically Stacked Organic Photodiode-Blocking Diode Imager by Turn-On Voltage Engineering. *Adv. Electron. Mater.* **4**, 1800311 (2018).

8. Richards, E. Curved electronic display element. (2017).

9. Bhattacharya, P. *Semiconductor optoelectronic devices*. (Prentice Hall, 1997).

10. Pierret, R. F. *Semiconductor device fundamentals*. (Addison-Wesley, 1996).

11. Herman, M. A. & Sitter, H. *Molecular Beam Epitaxy : Fundamentals and Current Status*. (Springer Berlin Heidelberg, 1996).

12. Singh, J. *Electronic and Optoelectronic Properties of Semiconductor Structures*. (Cambridge University Press, 2003).

13. Sze, S. M. & Ng, K. K. *Physics of semiconductor devices*. (Wiley-Interscience, 2007).

14. Green, M. A. *et al.* Solar cell efficiency tables (Version 55). *Prog. Photovoltaics Res. Appl.* **28**, 3–15 (2020).

15. Bauer, T. *Thermophotovoltaics*. *Green Energy and Technology* vol. 7 (Springer Berlin Heidelberg, 2011).

16. Plummer, J. D., Deal, M. D. & Griffin, P. B. *Silicon VLSI technology : fundamentals, practice, and modeling*. (Prentice Hall, 2000).

17. Renshaw, C. K. Hybrid Organic/Inorganic Optoelectronics. *Doctoral dissertation* (2013).

Chapter 2

Thin Film Technologies and Non-Planar Architectures

With the development of semiconductor fabrication technology, thin-film optoelectronics draw enormous attention due to the benefits of enhanced absorption/reflection, reduced fabrication cost, superior mechanical flexibility, opportunities for integration with dissimilar materials, etc., compared to conventional devices fabricated on rigid, bulk, and crystalline substrates. Various lift-off and transfer techniques have been employed to transplant thin-film active device epilayers from their parent epitaxial growth substrates to host substrates for applications in advanced optoelectronic devices. These thin-film devices are in some cases further deformed into non-planar architectures to enable superior performance inaccessible to conventional planar devices based on 2D geometries. One such example is the light sensing focal plane array used in imagers that fabrication on curved surfaces reduces the off-axis aberrations, and the field of view is concomitantly enlarged with simple optical components. Advanced artificial imaging systems have been intensively studied and demonstrated by mimicking the compound eye commonly found in insects, and the hemispherical shape of the retina in a human eye. Optoelectronics on *unconventional surfaces* enabled by these thin film technologies have brought exciting innovations to the current electronics industry.

2.1. Thin-Film Optoelectronics

As described in the previous chapter, III-V compound semiconductors are especially suitable for making optoelectronic devices. These devices are routinely grown over their parent crystalline substrates that are usually bulky, rigid, brittle, and expensive, to achieve a high epitaxial quality. In most cases, however, the epitaxial layers (usually a few nm to several μm thick) are the only useful part that contributes to the optical and electronic functions of the device. In some cases, the substrates even limit the device performance. For example, in a GaAs solar cell, a highly doped substrate can have substantial absorption of the incident light when the active layers are thin (< 2 μm), reducing quantum efficiency and short circuit current[1]. In a surface emitting LED, the light emission from the active layers is omni-directional. Photons that travel into the substrate have a high chance to be absorbed through either band-to-band or free carrier absorption, resulting in a low outcoupling efficiency[2].

Thin film technology provides paths for the grown epitaxial layers to be lifted off from the parent substrates and transferred to external substrates of interest. By doing so, optoelectronic devices can be integrated with dissimilar materials for advanced applications without the limitation of their lattice-matched platforms. For example, thin-film solar cells are often integrated with highly reflective materials (metals, DBRs, etc.) that act as a back surface reflector (BSF). The BSF enables light trapping[3] by increasing the path traveled by photons inside the active layers[4]. The active layer thickness can thus be reduced by at least half, resulting in reduction of source materials and growth time without a loss in performance. Figure 2.1 shows a schematic of light absorption in thin-film devices and substrate devices with and without light trapping. In addition, thin-film solar cells with a BSF provide photon recycling that extends minority carriers lifetime and increases open circuit voltage[5,6]. On the other hand, it is also possible to recycle the parent growth

substate if the crystalline surface can be restored to its original epi-ready quality. Growing devices on the recycled substrate multiple times is a critical step for the cost reduction in device production[7,8].

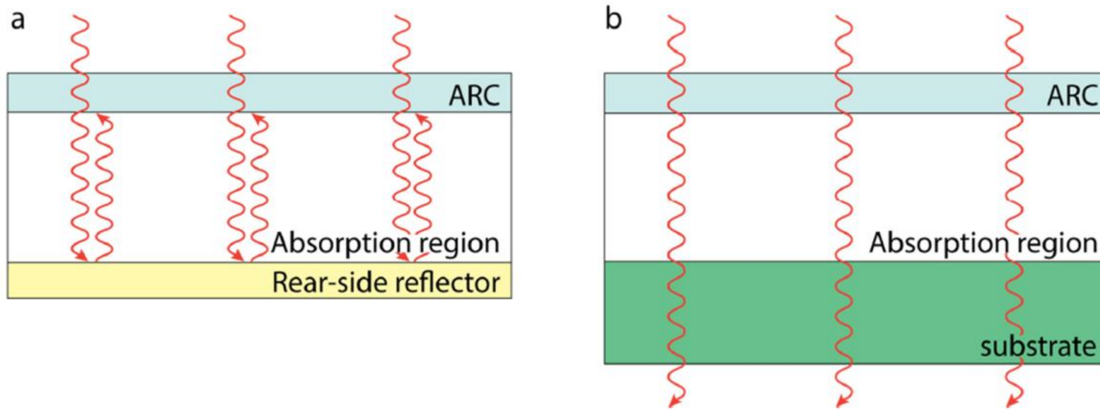

Figure 2.1: Schematic demonstration of light absorption.
(a) In thin-film devices and (b) in substrate devices with and without light trapping mechanism

2.1.1. Mechanical Spalling

Various lift-off and layer transfer technologies have been developed. Mechanical spalling is a simple physical method that separates epitaxial thin films from their growth substrates by controlling fracture propagation along certain interfaces[9,10]. Tensile stressor layers and external handles are usually required to initiate a crack running parallel to the substrate[11]. Figure 2.2 (a) illustrates a schematic of the mechanical spalling process. Flexible thin-film solar cells [9] and LEDs[10] separated from III-V parent substrates like GaAs and GaN and elemental semiconductor parent substrates such as Si and Ge have been demonstrated on external plastic substrates by this process (Figure 2.2 (b) and (c)). The problem with spalling is that the surface where the epilayer and the substrate separate is usually very rough so that lifting off very thin epitaxial layers (< 1µm) is challenging.

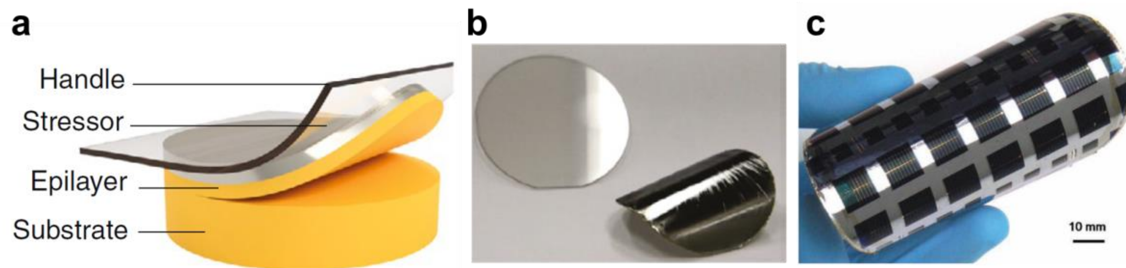

Figure 2.2: Illustration of mechanical spalling process.

(a) Schematic of mechanical spalling using a metal stressor layer and (b) resulting single-crystalline epitaxial membrane. (c) Photograph of fabricated thin-film tandem solar cells on plastic substrate. Reproduced from reference 9.

2.1.2. Epitaxial Lift-Off

Epitaxial lift-off (ELO) is currently the most widely used technique that produces III-V thin-film optoelectronic devices at the industrial scale. It is a chemical etching process that utilizes wet etchant to selectively etch the sacrificial layer pre-grown between the active device layers and the substrate (Figure 2.3 (a)). For common solar cell materials like GaAs, lattice-matched Al-containing compounds such as AlAs or AlGaAs can be used as sacrificial materials, and selectively etched in hydrofluoric (HF) acid. HF can also act as selective etchant for thin-film Si solar cells with SiO_2 being the sacrificial layer in Si-On-Insulator (SOI) wafers. For infrared photodetectors and TPV applications that usually employ InP and InGaAs, dilute hydrochloric (HCl) acid is an ideal etchant for InP with high selectivity to InGaAs, while citric acid mixed with hydrogen-peroxide (H_2O_2) only etches InGaAs without damaging InP.

Although highly selective and capable of peeling off high quality epitaxial layers, the ELO process is usually very slow (several hours to days for a 4 inch wafer). To solve this problem and increase the lift-off speed, a modified ELO process called weight-induced ELO (WI-ELO) was developed. This method employs either a heavy-weight object[12] or a cylindrical roller[1] that is

attached to the flexible substrate to which the epilayers are bonded. The epilayers are thus bent away from the parent substrate during sacrificial layer etching. The weight or roller opens the etching front, improves the diffusion of etchant at the etching interface, and accelerates the lift-off process.

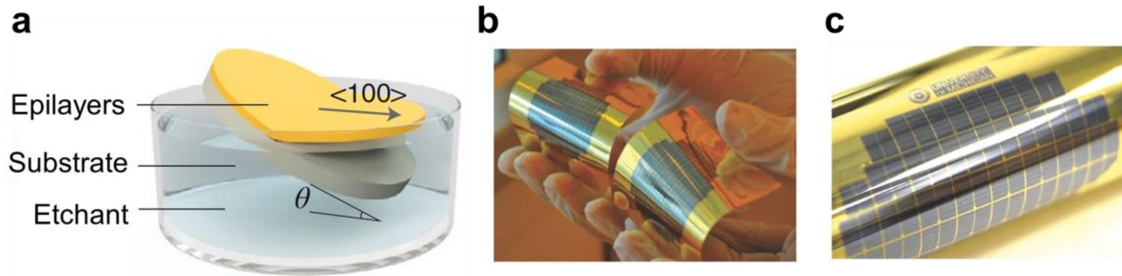

Figure 2.3: Illustration of epitaxial lift-off (ELO) process.
(a) Schematic of ELO process and (b) resulting single-crystalline epitaxial membrane. (c) Photograph of fabricated thin-film solar cells on plastic substrate. Reproduced from references 11 and 7.

Another attractive feature of the ELO process is the opportunity to reuse the parent growth substrate and reduce the overall cost of the production. The challenge, however, is to recover the original epi-ready quality of the crystalline surface on growth substrates. Chemical etching of sacrificial layers often causes roughness, damage, or etching residuals on the growth substrates[7]. Chemo-mechanical polishing (CMP) is a method that has been employed to prepare the epi-ready surface. For solar cell applications, no significant performance degradation has been observed on the thin-film GaAs and Ge solar cells grown on the recycled wafers prepared by this method[13,14]. The limitation remains, however, due to the substrate thinning during CMP that restricts the number of wafer reuses. In addition, the high cost of the CMP process cannot compensate for the cost saved on wafer recycling[15].

Another method that has huge potential to recover the epi-ready surface of the growth substrate with low cost is non-destructive ELO (ND-ELO). It inserts one or several epitaxially grown protection layers between the parent growth substrate and the sacrificial layers during the epitaxial growth stage. These protection layers comprise alternating lattice-matched arsenide-based and phosphide-based materials that enable recovery of the epi-ready wafer surface for regrowth on the original wafer without any observable degradation in surface quality or device performance[7]. For example, an InGaP and GaAs bilayer stack is grown on the GaAs parent substrate as protection layers. An AlAs sacrificial layer is then grown onto the protection layer stack, followed by the growth of the active device layers in the inverted order. After the AlAs layer is selectively etched using HF acid and the thin-film device layers are lifted-off from the substrate, the GaAs layer is first etched using a phosphoric acid-based etchant (H_3PO_4:H_2O_2:H_2O) until the etching stops at the InGaP layer, and the InGaP layer is then removed through etching in diluted HCl which provides complete etching selectivity with the GaAs substrate surface. The epi-ready substrate surface enabled by the ND-ELO process eliminates the additional CMP step for substrate preparation, and thus reduces the production cost of thin-film GaAs solar cells by at least three folds compared to the conventional ELO + CMP process[15]. Lee *et al.*[7] has demonstrated four times wafer recycling using ND-ELO process without apparent performance degradation on various lifted off thin-film optoelectronic and electronic devices including solar cells (Figure 2.3 (b) and (c)), LEDs, and transistors.

2.1.3. Laser Lift-Off

Laser lift-off (LLO) is a technique similar to ELO that separates thin-film epilayers from substrates by etch removal of the sacrificial layers between them. Instead of using chemical etchants, LLO decomposes the sacrificial layers by short-wavelength excimer laser radiation. The

sacrificial layers in LLO are usually composed of low-bandgap materials that have strong absorption to the laser energy, while the substrate materials are higher bandgap and hence transparent to the laser. Figure 2.4 (a) is a schematic of the LLO process. A GaN LED (Figure 2.4 (b)) lifted off from a sapphire substrate using GaN as the sacrificial layer[16] and InP thin film lifted-off from an InP substrate using InGaAs as the sacrificial layer[17] have been demonstrated. The LLO technique is relatively faster and enables high throughput production of thin-film optoelectronics compared to ELO. However, the roughness and surface damage on the substrate due to insufficient heat management and induced plasma at the lift-off interface during laser excitation remain an issue[18]. Additional polishing steps like CMP are often required to restore an epi-ready substrate, which increases the cost of production.

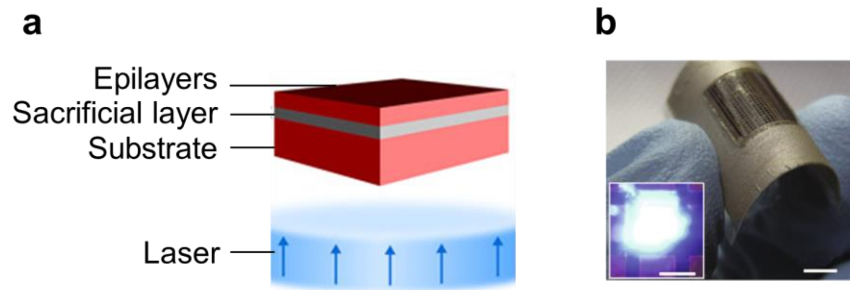

Figure 2.4: Illustration of laser lift-off (LLO) process.
(a) Schematic of LLO process and (b) resulting thin-film LED. Reproduced from references 17 and 16.

2.1.4. 2D Material-Assisted Lift-Off

Recently, 2D material-assisted lift-off and the remote epitaxy technique have been developed[19]. This technique employs monolayer 2D materials attached to the parent substrate through Van de Waals forces, and remotely grows epitaxial thin-film devices on their surface. The weak Van de Waals potential of 2D materials cannot screen the strong lattice potential of the underlying substrates, enabling epitaxial growth to occur despite its presence[19]. After the growth,

the epilayers are separated from the growth substrate similar to mechanical spalling through a stressor layer and an external handle, leaving a pristine substrate surface for regrowth. Figure 2.5 (a) illustrates a schematic of the 2D material-assisted lift-off process. Compared to mechanical spalling, this process has better control on the depth determined by the position of the 2D materials, requires less stress to separate the epilayers, and provides an atomically sharp interface without the need to polish the recycled substrate[11]. Using this 2D material-assisted lift-off method, GaAs, InP, and GaP thin films lifted off from their homo-epitaxial parent substrate have been demonstrate (Figure 2.5 (b)) together with a thin-film GaAs LED[19]. The wafer scale transferability of this method, however, has not been achieved due to imperfect control of defects on transferring large area monolayer materials.

Figure 2.5: Illustration of 2D assisted lift-off process.

(a) Schematic of 2D material-assisted lift-off process and (b) resulting GaAs thin film. Reproduced from references 11 and 19.

2.2. Non-Planar Architectures

In addition to lift-off from substrates, thin-film optoelectronic devices shaped onto three-3D surfaces can offer new functionalities inaccessible to conventional planar devices based on 2D geometries that are routinely fabricated by conventional photolithographic patterning processes.

A light sensing focal plane array (FPA) used in imagers is one example of a system that can benefit from fabrication on curved surfaces. By mimicking the hemispherical shape of the retina in the human eye, a hemispherical FPA provides a lightweight, compact imaging system with a low-aberration image, low *f*-number and a wide field of view[20–27]. Other examples include head-up and virtual reality displays that are often needed on curved or folded surfaces[28], wearable sensing devices[29–31], and conformal light absorption modules[32–35]. Due to the inherently high value of these applications, intensive efforts have been devoted to solving the problem of transforming a circuit fabricated on a flat wafer surface into an arbitrary shape without loss of performance or distorting the linear layouts that are the natural product of this fabrication paradigm. The transformation from 2D to 3D can be categorized into developable transformation, and non-developable transformation. The differences between these two and various methods on how to deform a plane into 3D shapes are discussed below.

2.2.1. Developable vs. Non-Developable Surfaces

A developable surface is a smooth surface with zero Gaussian curvature[36], meaning that the surface can be flattened onto a plane without distortion (stretching or compressing). Conversely, it is a surface which can be made by transforming a plane by folding, bending, or rolling[36]. Figure 2.6 (a) illustrates the deformation of a developable circuit from a flat to a cylindrical surface, representing a transformation between topologically equivalent surfaces. This transformation maintains a constant relative distance between two arbitrary fixed points on the surface (e.g. points **1** and **2**)[37]. Optoelectronic components fabricated on flexible substrates can be trivially bent to achieve functional devices on developable surfaces[23,38–41].

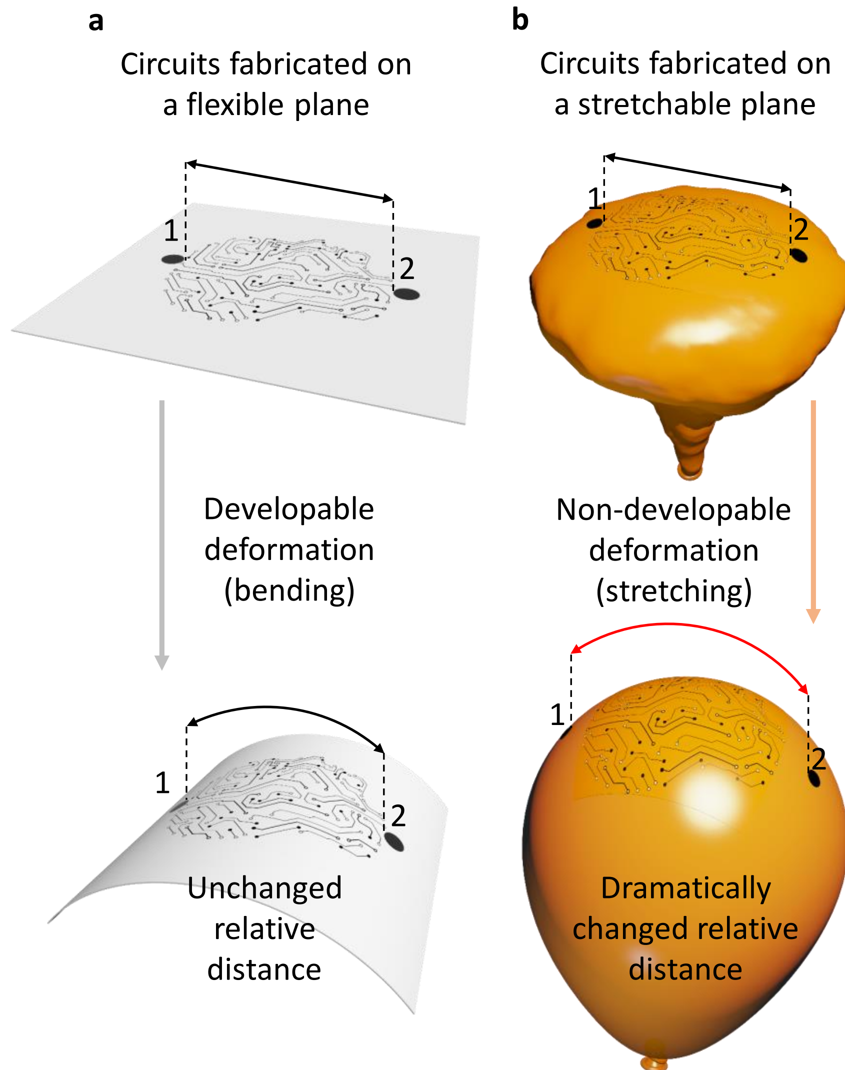

Figure 2.6: Schematic illustration of developable deformation vs. non-developable deformation process. (a) Circuits fabricated on a flexible plane and deformed into a developable semi-cylindrical shape that does not entail a topological transformation. The distance between points 1 and 2 along the surface remains the same after the deformation. (b) Circuits fabricated on a stretchable plane (a deflated balloon) and deformed into a non-developable, topologically distinct spherical shape (an inflated balloon). The distance between points 1 and 2 along the surface is dramatically increased after the deformation.

The topological transformation from a developable to a non-developable surface, however, is a more general type of distortion that can morph a plane into a random 3D shape. Figure 2.6 (b) illustrates circuits fabricated on a stretchable plane (e.g. a deflated balloon) transformed into a non-

developable spherical surface (an inflated balloon). This topological transformation results in a change in the relative distance between two arbitrary fixed points on the surface (points **1** and **2**)[37]. Electronic components fabricated on brittle semiconductors attached to the deformed surface suffer from strain that may eventually lead to structural damage[29,42]. Furthermore, the increased distances between points can lead to loss of resolution in pixel arrays located on the initially flat surface.

2.2.2. Methods for Deformation

2.2.2.1. Rolling

In general, there are four categories of methods to shape thin films into non-planar structures: rolling, folding, curving, and buckling[43]. The rolling process is mainly used to deform a plane into a cylindrical shape, which is basically a developable transformation. For III-V compound semiconductors, the rolling of epitaxially grown thin films are initiated by residual stress. Figure 2.7 (a) to (d) illustrates the rolling process based on a heteroepitaxial crystalline bilayer[44]. It begins with the epitaxial growth of two lattice-mismatched materials (GaAs and InAs) on a sacrificial layer (AlAs). The internal stress in the GaAs and InAs layers are opposing, i.e. the InAs layer experiences compressive stress, while the GaAs experience tensile stress. When the sacrificial layer is selectively etched, the two different stresses in this bilayer structure create a bending moment that rolls up the film. The rolling behavior can be precisely controlled by changing the lattice constants (governed by the composition of compounds) of the compressed and stretched materials to create controllable differential stress. An optically pumped micro-scale laser based on InGaAs/GaAs quantum dot roll-up tubes was demonstrated using stress induced rolling (Figure 2.7 (e))[45].

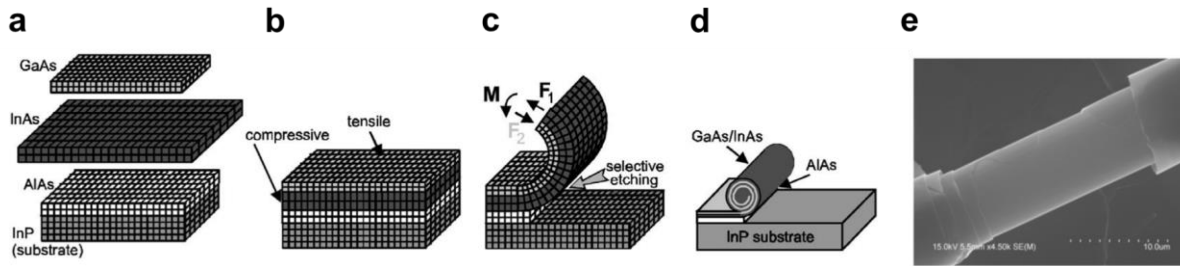

Figure 2.7: Illustration of the rolling process based on heteroepitaxial crystalline bilayer.
(a) InAs and GaAs layers with mismatched lattice constants. (b) Grow InAs/GaAs bilayer on an InP substrate. (c) GaAs/InAs bilayer slightly bent after the AlAs sacrificial layer is partial etched. (d) Self-rolling of the detached bilayers in a tube-scroll during further selective removal of the sacrificial layer. (e) Scanning electron microscopy image of lifted off rolled up microtube. Reproduced from references 44 and 45.

2.2.2.2. Folding

Folding is a deformation process that mechanically bends thin films locally through external or internal forces. The capillary force of water or other liquid droplets is one of the most commonly used external forces to achieve micro- or nano-scale folding[43]. Figure 2.8 (a) to (c) illustrates a schematic of capillary force assisted folding[46]. A Si membrane with a flower pattern is released from the SOI wafer by HF etching. A water droplet is applied to the center of the pattern. The volume of the water droplet needs to be large enough to cover the corners of the foil. As the water evaporates, the capillary force pulls the corners of the Si membrane up, causing it to wrap around the water droplet. Figure 2.8 (d) shows a spherical thin-film Si solar cell fabricated based on the folding process with an embedded glass bead to maintain a spherical shape. External forces can also be induced by residual stress (e.g. local ion-beam radiation[47], local deposition of stressed metals[48], etc.) to initiate folding.

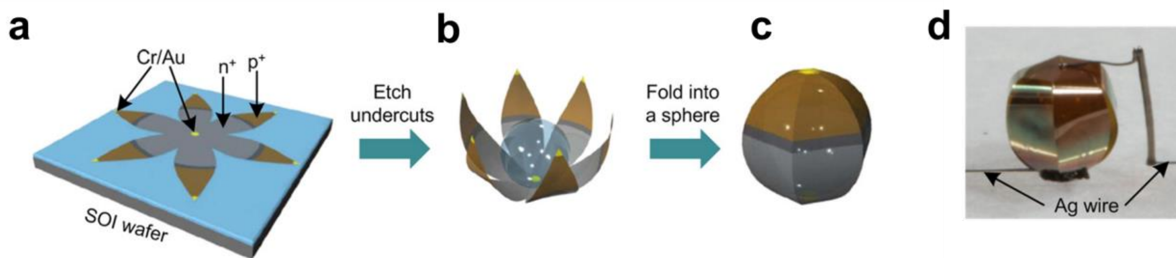

Figure 2.8: Illustration of folding process.

(a) - (c) Schematic representation of steps for fabricating a spherical-shaped Si solar cell. (d) Optical image of a complete device consisting of the folded spherical Si shell and printed silver electrodes. Reproduced from reference 46.

2.2.2.3. Curving

Curving is another method to achieve controllable transformation of thin-film optoelectronics from a plane to a curved 3D surface on a relatively large scale. The developable curving process can be achieved by simply bending thin films or wrapping them conformally to a cylinder. To deform thin films into non-developable shapes, however, more complex curving schemes that employ transfer printing based on an elastomer transfer stamp are often required. Figure 2.9 (a) to (c) shows a schematic of the curving process that transfers metal lines from a planar PDMS stamp to a plastic hemispherical substrate[42]. The hemispherical plastic substrate coated with a thin metal layer is placed in proximity to a membrane of patterned PDMS stamp of the same shape. The PDMS membrane is deformed by vacuum in a mold. After releasing vacuum, the stamp snaps into contact with the substrate surface. Metal patterns on the stamp and the metal layer on the plastic dome are bonded through cold-welding[49]. Reapplication of vacuum separates the PDMS stamp from the substrate, leaving the metal patterns on the hemisphere. An organic hemispherical FPA was demonstrated using this method as shown in Figure 2.9 (d). Inorganic

material based thin-film optoelectronics shaped into 3D shapes by similar curving processes have also been demonstrated, and are discussed in section 2.2.3 and Chapter 4.

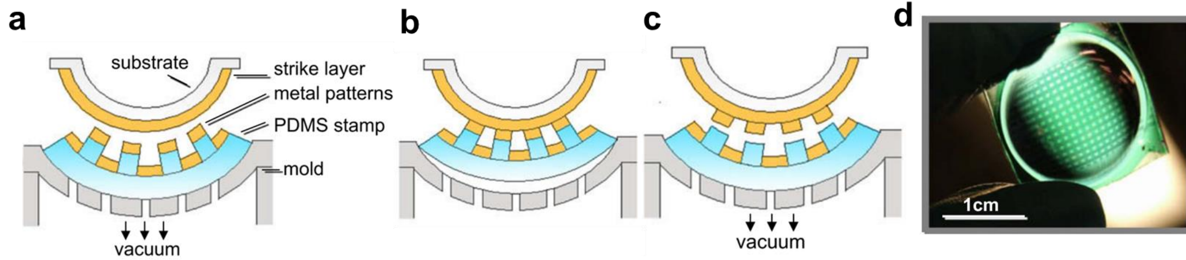

Figure 2.9: Illustration of the curving process based on transfer printing.
(a) - (c) Process sequence for fabricating a hemispherical FPA. (d) Photograph of an organic hemispherical focal plane array with metal interconnection patterned by the curving process. Reproduced from reference 42.

2.2.2.4. Buckling

Buckling pops materials and devices from 2D into 3D upon the relaxation of a pre-stretched elastomer base platform on which the 2D structure is bonded[50,51]. Here, Figure 2.10 (a) shows a schematic illustration of the buckling deformation process. A 2D precursor (Si thin films to be deformed) is patterned on its parent wafer (SOI). An external elastomer platform is used to stretch it uniaxially or biaxially. Next, lift off the 2D precursor from its parent wafer through chemical etching of the sacrificial layer and locally bond it to the bonding sites on the elastomer base by transfer printing. Then, release the pre-stretched elastomer substrate to generate compressive forces at the bonding sites and deform the 2D precursor into 3D mesostructure. The strategies of 2D precursor patterning, and the path of stretching and releasing of the base platform, can be precisely engineered to achieve very complex 3D structures[52] as shown in Figure 2.10 (b). The demonstrated optoelectronic devices include an outward facing hemispherical photoconductor system based on MoS_2[26] (Figure 2.10 (c)), and a pop-up 3D micro-electronic/optoelectronic system with integrated LEDs and photodiodes[53] (Figure 2.10 (d)).

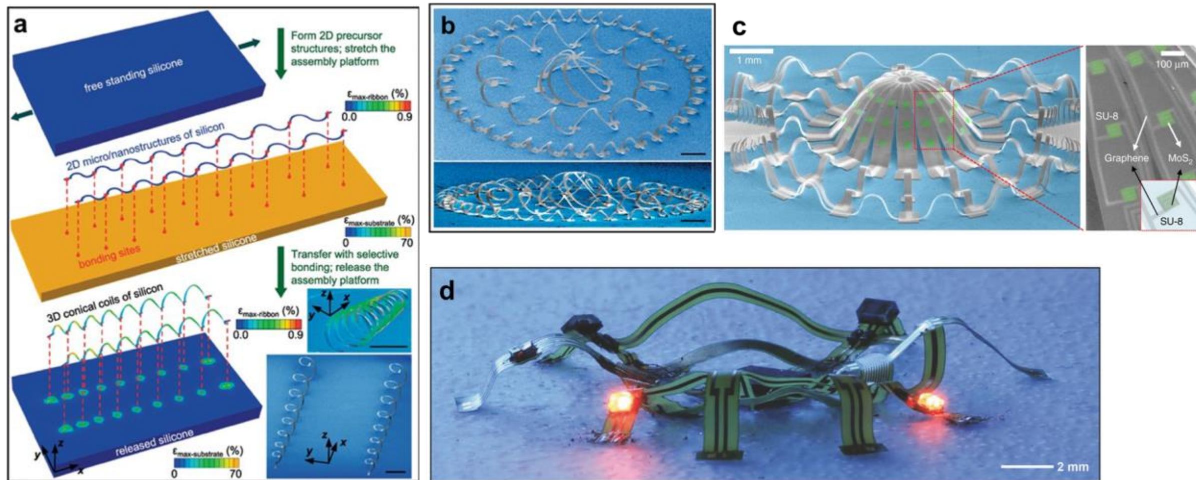

Figure 2.10: Illustration of the buckling process.

(a) Schematics for deterministic assembly of 3D mesostructures. (b) SEM images of a complex 3D mesostructure formed from a 2D precursor selectively bonded to a biaxially stretched elastomer substrate. (c) SEM image of MoS_2 photodetectors on the hemisphere with 3D interconnects. (d) Photographs of a 3D electronic/optoelectronic systems transformed from 2D using buckling process. Reproduced from references 26,50,53.

2.2.3. Bio-Inspired Artificial Imaging Systems

Natural imaging systems such as the compound eye or the human eye often employ conformal architectures that provide aberration-free images with wide field of view (FOV) or a very low *f*/number. However, the pace of imager development has been limited to planar geometries with their inherent disadvantages, including narrow FOV and off-axis optical aberrations[22,54]. The imperfect match between the focal and image planes of simple lenses necessitates additional optical elements[55] that increase the complexity, weight and cost of the imaging system. Inspired by the diversity of light sensing mechanisms in nature, intensive efforts have been made in the development of novel imaging systems that employ unconventional geometries and provide superior performance beyond existing technologies[56]. There are in general two types of vision systems in nature. One is the compound eye commonly found in arthropods, and the other is single-chambered eye in human and other mammals.

2.2.3.1. Compound Eye Type Imaging Systems

Figure 2.11 (a) is a schematic of the major components in a typical compound eye. It is composed of several ommatidia as visual units. Each ommatidium has an independent optical lens that focuses the incident light onto a light sensing rhabdom, which then converts light to neural signals[57]. The rhabdoms are surrounded by screening pigments that prevent light interference between adjacent ommatidia[57]. These ommatidia are often tightly packed on a convex hemisphere. The hemispherical geometry of the compound eye enables extremely wide FOV without the need of head movements[56], while the small dimension of each ommatidium provides nearly infinite depth of field and distortion- and aberration-free imaging capability[58].

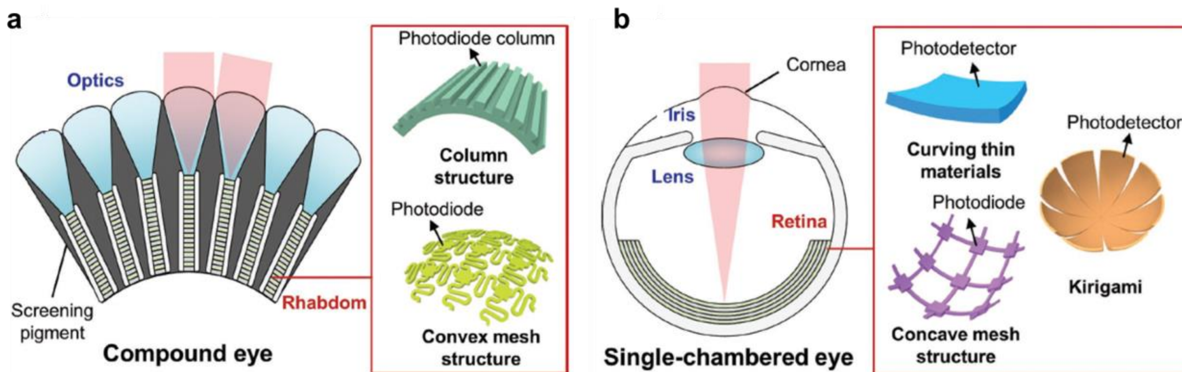

Figure 2.11: Schematic illustrations of the major components of bio-inspired imaging systems.
(a) Compound eye. (b) Single-chambered eye. Reproduced from reference 56.

Light sensing FPAs that consist of a large number of photodetectors are ideal optoelectronic devices to mimic the rhabdoms in compound eyes. The challenge, however, is to fabricate photodetector arrays with high pixel density on highly curved surfaces. As shown in the inset of Figure 2.11 (a), there are two general approaches to solve this issue. The first is a straightforward method that fabricates a photodetector array on a flexible surface and bends the array to a cylindrical shape, representing a 2D developable transformation solution. The other

method is to fabricate a photodetector array with a meshed interconnection structure. The mesh thus provides strain and elongation tolerance for an interconnecting circuit under non-developable transformation, enabling a functional photodetector array on a convex hemisphere.

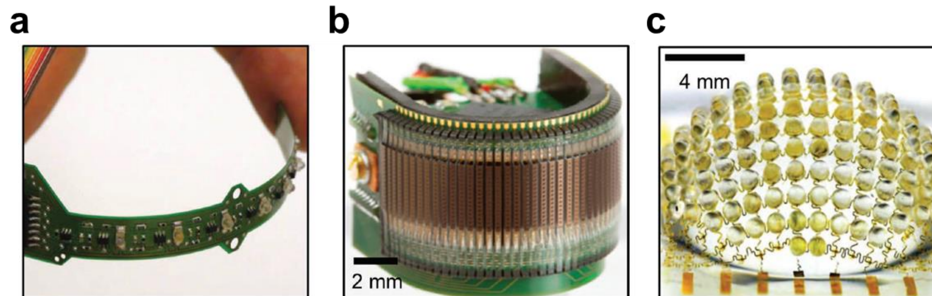

Figure 2.12: Demonstrations of artificial compound eye type imaging systems.
Photographs of (a) Vision Tape (b) Miniature artificial compound eye (c) hemispherical compound eye. Reproduced from references 25,38,59.

Dobrzynski *et al.*[59] demonstrated a Vision Tape with eight Si detectors fabricated on a flexible printed circuit board (FPCB) for motion extraction and proximity estimation (Figure 2.12 (a)). This device is wrapped around large objects such as human hands, heads, and the corner of a desk to demonstrate its wide FOV. However, the Vision Tape has no imaging capability due to its low pixel count. A similar scheme was employed in a miniature artificial compound eye demonstration[38] (Figure 2.12 (b)), in which the pixel count was increased to 630. The resolution of this system is significantly improved compared to the Vision Tape. However, the transformation remains developable, which only provides a wide FOV in one dimension. In addition, the device is bulky since the photodetector columns are not lifted off from the substrate and the column separation is achieved through wafer dicing. A hemispherical compound eye imager (Figure 2.12 (c)) was demonstrated by Song *et al.*[25] using the interconnecting mesh method as described above. This demonstration provides a 160° hemispherical FOV when integrated with a PDMS micro-lens

array (MLA). It also achieves nearly infinite depth of field, and low imaging aberrations, representing a successful imitation of the compound eyes in arthropods. The pixel density, however, is limited by the space reserved for the interconnecting mesh. Realizing a high resolution image using this method is difficult.

2.2.3.2. Single-Chambered Eye Type Imaging Systems

Figure 2.11 (b) illustrates the major components in a single-chambered eye. The incident light is focused through a single convex lens to the concave retina, which is a nearly hemispherical light-sensitive three-layer structure on the back of the human eye that converts light to neural signals through complex processes[56]. The hemispherical configuration of the retina enables a FOV of up to 95° with very low optical aberration when combined with an unusual graded refractive index lens[60]. In addition, the muscles around the iris can actively adjust the focal length to recognize objects at different distances, and opening size of iris can change to adapt for different light conditions.

Many efforts have been made to shape the light sensing FPA into a concave hemisphere, mimicking the geometry of retina in single-chambered eye. There are three types of methods as illustrated in the inset of Figure 2.11 (b). The first is to curve a conventional thin-film FPA using a truncated hemispherical vacuum mold. The photodetectors and interconnections on the FPA membrane, however, are strained after the deformation. The second method is to build meshed interconnection bridges between pixels as described in the fabrication of artificial compound eyes. Recently, a third method has been developed based on Origami assembly. The hemispherical shape can be achieved by cutting, folding, and mating pre-patterned sections to form an approximately hemispherical shape.

Figure 2.13 (a) presents a demonstration[20] of an artificial single-chambered eye type imager using the vacuum deformation curving method. A commercial CMOS imager was thinned through substrate polishing, and subsequently deformed into a truncated hemispherical shape by applying vacuum. No apparent performance degradation of individual pixels was observed, and the optical aberration of the field curvature was reduced after the deformation.

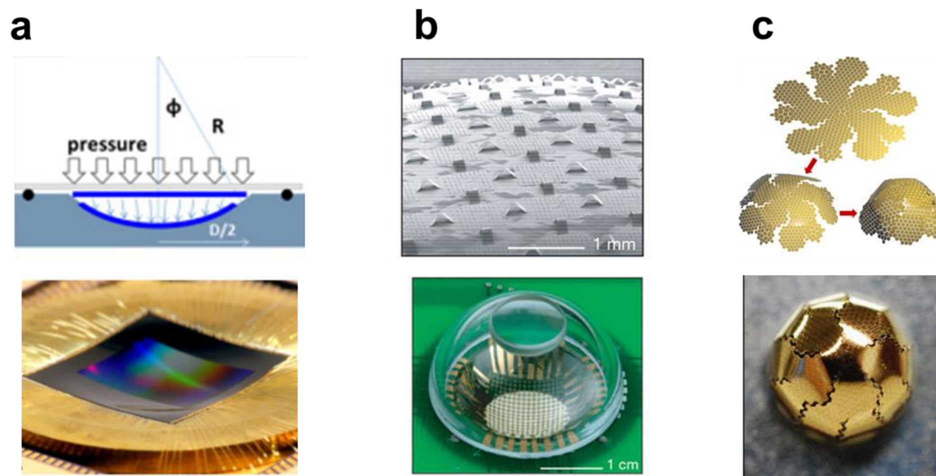

Figure 2.13: Demonstrations of artificial single-chambered eye type imaging systems.
(a) Schematic of vacuum deformation curving method and photograph of a resulting hemispherical imager. (b) SEM image and photograph of an artificial single-chambered eye employing meshed interconnection. (c) Schematic of Origami assembly method and photograph of a resulting hemispherical imager.
Reproduced from references 20,24,27.

However, the deformation is inevitably small and limited to a relatively larger radius of curvature (~19 mm) compared to that of a human retina (~12 mm) due to strain limitations of rigid crystalline materials, and the area coverage of the FPA is not a perfect hemisphere. A single-chambered eye imager with large deformation has been demonstrated[24] by the meshed interconnection method (Figure 2.13 (b)). The bendable and stretchable metal interconnection bridges between pixels relieve strain during non-developable deformation from a plane to a concave hemisphere to create a retina-like imager with full hemispherical coverage. However, the

gaps between pixels reserved for the bridges result in a loss of resolution, particularly near the central "fovea" at the point of maximum strain. Origami-inspired hemispherical FPAs were reported[27,61,62] with high deformability and pixel count (Figure 2.13 (c)). This process, however, does not result in a perfect conformation to a hemispherical surface, leading to undesirable optical aberrations and image stitching errors.

2.3. Summary

Thin-film optoelectronics is a fast-developing technology exhibiting numerous benefits over conventional optoelectronics based on rigid, bulk, and crystalline substrates including enhanced light absorption/reflection, reduced fabrication cost, mechanical flexibility, integration with dissimilar materials, etc. Lift-off and transfer techniques enable the separation of device epilayers from their parent growth substrates for advanced optoelectronic applications and provide a potential for substrate recycling leading to cost reduction. Thin-film devices deformed into non-planar architectures enable superior performance and novel applications inaccessible to conventional devices with 2D geometries. Employing various deformation and assembly methods, remarkable artificial imaging systems inspired by the optical superiority of compound and single-chambered eye architectures have been demonstrated. Optoelectronics on *unconventional surfaces* enabled by these thin film technologies have brought exciting innovations to the current electronics industry.

CHAPTER 2

Bibliography

1. Schermer, J. J. *et al.* Photon confinement in high-efficiency, thin-film III–V solar cells obtained by epitaxial lift-off. *Thin Solid Films* **511**–**512**, 645–653 (2006).

2. Schnitzer, I., Yablonovitch, E., Caneau, C., Gmitter, T. J. & Scherer, A. 30% external quantum efficiency from surface textured, thin-film light-emitting diodes. *Appl. Phys. Lett.* **63**, 2174–2176 (1993).

3. Yablonovitch, E. Statistical ray optics. *J. Opt. Soc. Am.* **72**, 899 (1982).

4. Bauhuis, G. J., Mulder, P., Haverkamp, E. J., Huijben, J. C. C. M. & Schermer, J. J. 26.1% thin-film GaAs solar cell using epitaxial lift-off. *Sol. Energy Mater. Sol. Cells* **93**, 1488–1491 (2009).

5. Miller, O. D., Yablonovitch, E. & Kurtz, S. R. Strong internal and external luminescence as solar cells approach the Shockley-Queisser limit. *IEEE J. Photovoltaics* **2**, 303–311 (2012).

6. Sheng, X. *et al.* Device Architectures for Enhanced Photon Recycling in Thin-Film Multijunction Solar Cells. *Adv. Energy Mater.* **5**, 1400919 (2015).

7. Lee, K., Zimmerman, J. D., Hughes, T. W. & Forrest, S. R. Non-Destructive Wafer Recycling for Low-Cost Thin-Film Flexible Optoelectronics. *Adv. Funct. Mater.* **24**, 4284–4291 (2014).

8. Lee, K., Shiu, K.-T., Zimmerman, J. D., Renshaw, C. K. & Forrest, S. R. Multiple growths of epitaxial lift-off solar cells from a single InP substrate. *Appl. Phys. Lett.* **97**, 101107 (2010).

9. Shahrjerdi, D. & Bedell, S. W. Extremely flexible nanoscale ultrathin body silicon integrated circuits on plastic. *Nano Lett.* **13**, 315–320 (2013).

10. Bedell, S. W. *et al.* Layer transfer by controlled spalling. *J. Phys. D. Appl. Phys.* **46**, (2013).

11. Kum, H. *et al.* Epitaxial growth and layer-transfer techniques for heterogeneous integration of materials for electronic and photonic devices. *Nat. Electron.* **2**, 439–450 (2019).

12. Voncken, M. M. A. . *et al.* Influence of radius of curvature on the lateral etch rate of the weight induced epitaxial lift-off process. *Mater. Sci. Eng. B* **95**, 242–248 (2002).

13. Bauhuis, G. J. *et al.* Wafer reuse for repeated growth of III-V solar cells. *Prog. Photovoltaics Res. Appl.* **18**, 155–159 (2010).

14. Adams, J. *et al.* Demonstration of multiple substrate reuses for inverted metamorphic solar cells. *IEEE J. Photovoltaics* **3**, 899–903 (2013).

15. Lee, K., Lee, J., Mazor, B. A. & Forrest, S. R. Transforming the cost of solar-to-electrical energy conversion: Integrating thin-film GaAs solar cells with non-tracking mini-concentrators. *Light Sci. Appl.* **4**, e288 (2015).

16. Chun, J. *et al.* Laser lift-off transfer printing of patterned GaN light-emitting diodes from sapphire to flexible substrates using a Cr/Au laser blocking layer. *Scr. Mater.* **77**, 13–16 (2014).

17. Jan, A., Reeves, B. A., van de Burgt, Y., Hayes, G. J. & Clemens, B. M. Threshold Fluence Measurement for Laser Liftoff of InP Thin Films by Selective Absorption. *Adv. Eng. Mater.* **20**, 1700624 (2018).

18. Gerhard, C. & Stappenbeck, M. Impact of the polishing suspension concentration on laser damage of classically manufactured and plasma post-processed zinc crown glass surfaces. *Appl. Sci.* **8**, 1556 (2018).

19. Kim, Y. *et al.* Remote epitaxy through graphene enables two-dimensional material-based layer transfer. *Nature* **544**, 340–343 (2017).

20. Guenter, B. *et al.* Highly curved image sensors: a practical approach for improved optical performance. *Opt. Express* **25**, 13010 (2017).

21. Dinyari, R., Rim, S.-B., Huang, K., Catrysse, P. B. & Peumans, P. Curving monolithic silicon for nonplanar focal plane array applications. *Appl. Phys. Lett.* **92**, (2008).

22. Rim, S.-B., Catrysse, P. B., Dinyari, R., Huang, K. & Peumans, P. The optical advantages of curved focal plane arrays. *Opt. Express* **16**, 4965 (2008).

23. Fan, D., Lee, K. & Forrest, S. R. Flexible Thin-Film InGaAs Photodiode Focal Plane Array. *ACS Photonics* **3**, (2016).

24. Ko, H. C. *et al.* A hemispherical electronic eye camera based on compressible silicon optoelectronics. *Nature* **454**, 748–753 (2008).

25. Song, Y. M. *et al.* Digital cameras with designs inspired by the arthropod eye. *Nature* **497**, 95–99 (2013).

26. Lee, W. *et al.* Two-dimensional materials in functional three-dimensional architectures with applications in photodetection and imaging. *Nat. Commun.* **9**, 1417 (2018).

27. Zhang, K. *et al.* Origami silicon optoelectronics for hemispherical electronic eye systems. *Nat. Commun.* **8**, 1782 (2017).

28. Richards, E. Curved electronic display element. (2017).

29. Miyamoto, A. *et al.* Inflammation-free, gas-permeable, lightweight, stretchable on-skin electronics with nanomeshes. *Nat. Nanotechnol.* **12**, 907–913 (2017).

30. Someya, T. *et al.* A large-area, flexible pressure sensor matrix with organic field-effect transistors for artificial skin applications. *Proc. Natl. Acad. Sci.* **101**, 9966–9970 (2004).

31. Someya, T. *et al.* Conformable, flexible, large-area networks of pressure and thermal sensors with organic transistor active matrixes. *Proc. Natl. Acad. Sci.* **102**, 12321–12325 (2005).

32. Xu, X. *et al.* Thermally stable, highly efficient, ultraflexible organic photovoltaics. *Proc. Natl. Acad. Sci. U. S. A.* **115**, 4589–4594 (2018).

33. Park, S. *et al.* Ultraflexible Near-Infrared Organic Photodetectors for Conformal Photoplethysmogram Sensors. *Adv. Mater.* **30**, 1802359 (2018).

34. Park, S. *et al.* Self-powered ultra-flexible electronics via nano-grating-patterned organic photovoltaics. *Nature* **561**, 516–521 (2018).

35. Wu, Y. L. *et al.* Low-Power Monolithically Stacked Organic Photodiode-Blocking Diode Imager by Turn-On Voltage Engineering. *Adv. Electron. Mater.* **4**, 1800311 (2018).

36. Kühnel, W. *Differential geometry : curves - surfaces - manifolds*. (American Mathematical Society, 2006).

37. Ventsel, E. & Krauthammer, T. Geometry of the Middle Surface. in *Thin Plates and Shells* 303–324 (2001).

38. Floreano, D. *et al.* Miniature curved artificial compound eyes. *Proc. Natl. Acad. Sci.* **110**, 9267–9272 (2013).

39. Shen, G. & Fan, Z. *Flexible Electronics*. (World Scientific Publishing Co, 2016).

40. Saito, H., Hoshino, K., Matsumoto, K. & Shimoyama, I. Compound eye shaped flexible organic image sensor with a tunable visual field. *18th IEEE International Conference on Micro Electro Mechanical Systems, 2005. MEMS 2005.* 96–99 (2005).

41. Yang, W. *et al.* Large-area InP-based crystalline nanomembrane flexible photodetectors. *Appl. Phys. Lett.* **96**, 121107 (2010).

42. Xu, X., Davanco, M., Qi, X. & Forrest, S. R. Direct transfer patterning on three dimensionally deformed surfaces at micrometer resolutions and its application to hemispherical focal plane detector arrays. *Org. Electron.* **9**, 1122–1127 (2008).

43. Cheng, X. & Zhang, Y. Micro/Nanoscale 3D Assembly by Rolling, Folding, Curving, and Buckling Approaches. *Advanced Materials* vol. 31 1901895 (2019).

44. Prinz, V. Y. A new concept in fabricating building blocks for nanoelectronic and nanomechanic devices. *Microelectron. Eng.* **69**, 466–475 (2003).

45. Mi, Z. & Bianucci, P. When self-organized In(Ga)As/GaAs quantum dot heterostructures roll up: Emerging devices and applications. *Curr. Opin. Solid State Mater. Sci.* **16**, 52–58 (2012).

46. Guo, X. *et al.* Two- and three-dimensional folding of thin film single-crystalline silicon for photovoltaic power applications. *Proc. Natl. Acad. Sci. U. S. A.* **106**, 20149–54 (2009).

47. Cui, A. *et al.* Directly patterned substrate-free plasmonic “nanograter” structures with

unusual Fano resonances. *Light Sci. Appl.* **4**, e308–e308 (2015).

48. Bassik, N., Stern, G. M. & Gracias, D. H. Microassembly based on hands free origami with bidirectional curvature. *Appl. Phys. Lett.* **95**, 091901 (2009).

49. Kim, C., Burrows, P. E. & Forrest, S. R. Micropatterning of Organic Electronic Devices by Cold-Welding. *Sci.* **288**, 831–833 (2000).

50. Xu, S. *et al.* Assembly of micro/nanomaterials into complex, three-dimensional architectures by compressive buckling. *Science* **347**, 154–159 (2015).

51. Yan, Z. *et al.* Controlled Mechanical Buckling for Origami-Inspired Construction of 3D Microstructures in Advanced Materials. *Adv. Funct. Mater.* **26**, 2629–2639 (2016).

52. Yan, Z. *et al.* Deterministic assembly of 3D mesostructures in advanced materials via compressive buckling: A short review of recent progress. *Extrem. Mech. Lett.* **11**, 96–104 (2017).

53. Kim, B. H. *et al.* Mechanically Guided Post-Assembly of 3D Electronic Systems. *Adv. Funct. Mater.* **28**, 1803149 (2018).

54. Swain, P. K., Channin, D. J., Taylor, G. C., Lipp, S. A. & Mark, D. S. Curved CCDs and their application with astronomical telescopes and stereo panoramic cameras. *Proc. SPIE* vol. 5301 109–129 (2004).

55. Brady, D. J. *et al.* Multiscale gigapixel photography. *Nature* **486**, 386–389 (2012).

56. Lee, G. J., Choi, C., Kim, D. H. & Song, Y. M. Bioinspired Artificial Eyes: Optic Components, Digital Cameras, and Visual Prostheses. *Advanced Functional Materials* vol. 28 1705202 (2018).

57. Land, M. F. & Nilsson, D.-E. *Animal Eyes*. (Oxford University Press, 2012).

58. Lakshminarayanan, V. & Kuppuswamy Parthasarathy, M. Biomimetic optics: visual systems. *J. Mod. Opt.* 1–26 (2016).

59. Dobrzynski, M. K., Pericet-Camara, R. & Floreano, D. Vision tape-a flexible compound vision sensor for motion detection and proximity estimation. *IEEE Sens. J.* **12**, 1131–1139 (2012).

60. Atchison, D. A. & Smith, G. *Optics of the human eye*. (Butterworth-Heinemann, 2000).

61. Wu, T. *et al.* Design and fabrication of silicon-tessellated structures for monocentric imagers. *Microsystems Nanoeng.* **2**, 16019 (2016).

62. Choi, C. *et al.* Human eye-inspired soft optoelectronic device using high-density MoS2-graphene curved image sensor array. *Nat. Commun.* **8**, 1664 (2017).

Chapter 3

A Flexible Thin-Film InGaAs Photodiode Focal Plane Array

Most artificial imagers such as conventional cameras are limited to a planar architecture demanded by the use of brittle semiconductor focal plane arrays (FPAs). High resolution image formation on this flat field requires multiple bulky optical elements. In this chapter, we demonstrate a general approach to fabricating complex circuits and, in particular, FPAs on flexible and/or conformable substrates that can be shaped to overcome these fundamental limitations. An 8×100, lightweight, thin-film $In_{0.53}Ga_{0.47}As$ *p-i-n* photodiode FPA with sensitivity to wavelengths as long as $\lambda = 1650$ nm is fabricated on a thin flexible plastic foil following transfer by adhesive-free bonding of the epitaxial layers that are subsequently lifted off from the parent InP substrate. The array is shaped into either a convex cylindrically curved imager to achieve a 2π FOV, or when formed into a concave shape, to provide high resolution and compact spectral decomposition over a wide wavelength range. The array exhibits ~99% fabrication yield with ~100% peak external quantum efficiency at $\lambda = 1300$ nm. The unique features of this flexible thin-film FPA provide a new paradigm for realizing advanced electronic and imaging applications.

3.1. Introduction

High performance photodetector focal plane arrays (FPAs) have been investigated to fulfill the increasing demands for advanced imaging systems. However, the pace of imager development

has been primarily limited to planar geometries with their inherent disadvantages, including narrow field of view (FOV) and off-axis optical aberrations[1,2]. The imperfect match between the focal and image planes of simple lenses necessitates additional optical elements[3] that increase the complexity, weight and cost of the imaging system. Considerable recent efforts[4,5] in the fabrication of flexible electronic devices[2,6,7,8] have led to demonstration of non-planar arrays that conform to the focal plane of a simple lens system. These demonstrations include deforming the focal plane using semi-cylindrical[9,10] and hemispherical[11,12] geometries to reduce aberrations and increase the FOV. For example, Song, *et al.*[11] demonstrated conformal photodiode arrays fabricated on stretchable substrates combined with an elastomeric microlens array to achieve approximately 180° FOV. One shortcoming of that and many similar approaches is that the spacing between adjacent detectors is large and often increased on deformation to form non-developable 3D curved array surfaces, leading to low resolution images.

Here, we demonstrate a flexible InGaAs FPA with high optical performance, high yield, and importantly, high pixel density on a 2D, developable array surface. By sacrificing one dimension of deformation, the pixel spacing remains unchanged upon transforming into the desired conformal shape. It is sensitive across the shortwave infrared (SWIR) spectral range with applications to spectroscopy, night vision, and surveillance. Specifically, we demonstrate the fabrication of a thin-film 8×100 InGaAs *p-i-n* photodiode FPA transferred to a thin plastic foil via cold-weld bonding[13], and then epitaxially lifted off (ELO)[14,15] from its parent (growth) substrate. The FPA is conveniently transformed into a conformal imager owing to the flexibility of the substrate, absence of brittle adhesives, and the very thin semiconductor devices mounted onto its surface. The conformal FPAs are used as a compact, *convex,* 1 cm diameter cylindrical imager that achieves a 360° in-plane FOV; i.e. it demonstrates “2π awareness”. Moreover, by imparting a

concave curvature, we demonstrate very high resolution, aberration-free spectral decomposition of multiple wavelengths extending across the SWIR, providing significantly improved performance compared with planar arrays used in conventional spectrophotometric applications. The methods employed can readily be extended to a wide range of devices, from active pixel sensors to light emitting diodes used in flexible displays[15]. The method is independent of the semiconductor materials choice, and can in principal achieve extremely high pixel densities due to the complete elimination of solder-bump technology typically used in bonding detectors to readout back planes[16,17,18].

Our FPA, weighing only 30 mg, shows nearly perfect fabrication yield (~99%) and an external quantum efficiency of *EQE* ~100% at a wavelength of $\lambda = 1300$ nm, with an almost equally high sensitivity from $\lambda = 980$ nm to 1650 nm. An integrated back side metal mirror reduces the active layer thickness by almost half that of a conventional InGaAs photodiode while maintaining high absorption[19,20]. These results confirm that thin-film arrays provide flexibility while maintaining high performance that can exceed analogous substrate-based devices. The unique features of this imaging system enable a broad range of applications, including high resolution spectroscopy[21], robotics[9], and telescopes[2,22].

3.2. Photodiode Focal Plane Array Fabrication

Fabrication of the FPA starts with the epitaxial growth (see Figure 3.1) of the InGaAs *p-i-n* photodiode active layer structure on a 2 inch (50.8 mm) diameter, Zn doped (100) InP wafer using gas source molecular beam epitaxy. An undoped, 200 nm thick InP buffer layer is grown, followed by a 4 nm thick lattice-mismatched AlAs sacrificial layer which is significantly greater than the critical thickness (~2 nm), above which a high density of defects is formed[23]. Nevertheless,

transmission electron microscope images indicate no apparent defects in the epitaxial layers. Next, a 200 nm thick Be doped (2×10^{18} cm^{-3}) p^+-InP window layer is grown, followed by a 2.1 μm thick unintentionally doped *i*-$In_{0.53}Ga_{0.47}As$ active absorption layer and a 100 nm thick Si-doped (5×10^{18} cm^{-3}) n^+-$In_{0.53}Ga_{0.47}As$ contact layer. The active device region is grown in inverted order such that top illumination *p*-*i*-*n* photodiode structures result from bonding to the host (Si/plastic) substrate and lift-off from the parent InP wafer.

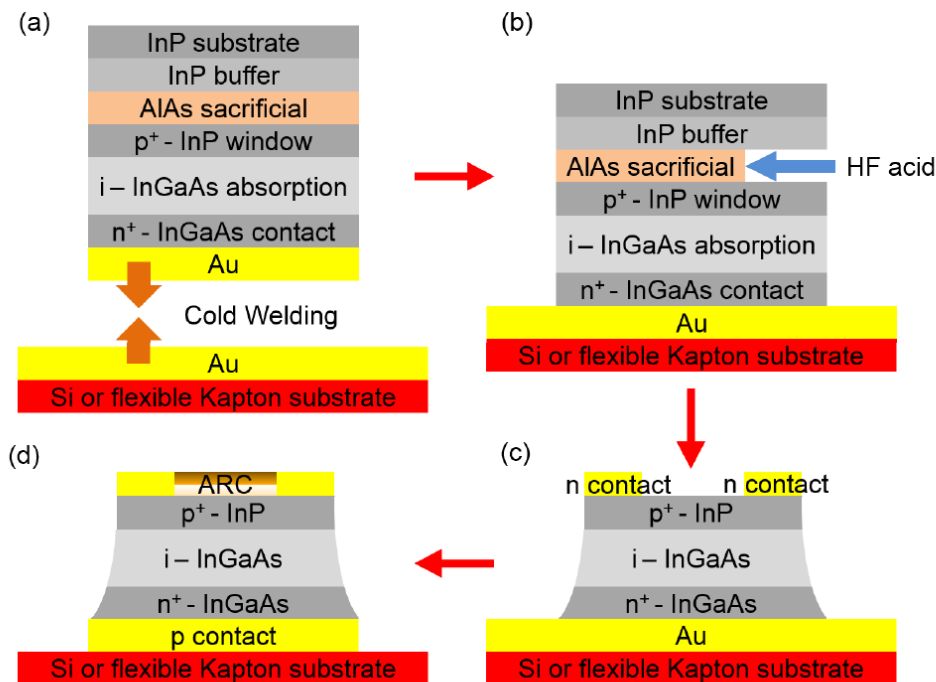

Figure 3.1: Schematic of fabrication flow of *p-i-n* thin-film photodiode.

(a) The device epi-growth structure and the cold-welding process to bond the epi-sample onto a host substrate; (b) the epitaxial lift-off process to separate the active device region from the parent InP substrate, transferring the thin-film photodiode epi-layers to the host substrate; (c) the front contact patterning and mesa defining process to make *p*-*i*-*n* InGaAs photodiode mesas on the host substrate; and (d) the back contact patterning and top bi-layer anti-reflection coating (ARC) deposition process to finish the fabrication.

The wafer is diced into 33×4 mm rectangles. Immediately after dicing, the epitaxial samples are rinsed with deionized water for 30 s to remove dicing residues. The samples are stored

in acetone to prevent possible surface contamination from the environment. The samples are rinsed for 5 min in isopropanol at 80°C, and the surface native oxide of the epitaxial layer is removed in buffered HF for 1 min, and rinsed in de-ionized (DI) water for 10 s. Next, 0.5 nm thick Ir followed by 200 nm thick Au layers are deposited by e-beam evaporation on both the epitaxial surface and a 25 μm thick, E-type Kapton® host foil substrate. During deposition, the sample is taped to a 4 inch (101.6 mm) rigid Si handle to keep it flat; a method applied during all subsequent metal evaporation steps.

The diced samples and host substrate are cold-weld bonded by applying heat (200°C) and pressure (20 MPa) for 5 min under vacuum (10^{-4} mTorr) using an EVG 510 wafer bonder. Cold-weld bonding is the bonding process that forms metallic junction by bringing two flat metal surfaces into intimate contact[13,24]. The metallic bond forms between two atomically flat metal surfaces when their spacing is below a critical thickness (a few angstroms)[25]. The intimate contact can be achieved with the application of pressure. Due to surface imperfections such as desorbed particles and native oxide films, bonding two hard surfaces often requires very high pressure (> 50 MPa). Low pressure bonding has been demonstrated by employing soft elastomer stamps during the bonding[13]. In this work, a soft graphite sheet is inserted between the sample and the bonder press head to ensure the application of uniform force across the array during bonding.

The epitaxial layers are then separated from the parent InP substrate by removing the AlAs layer through immersion in 17% HF in water at 45°C while agitating at 400 rpm using a magnetic stir bar. The epitaxial layers are fully transferred to the host substrate in 1.5 hr. After ELO, the samples are stored at 60°C in Remover PG (MicroChem) to prevent oxide formation on the epitaxial surface prior to further processing.

A process flow for fabrication of the thin-film InGaAs *p-i-n* photodiode array after the transfer of epilayers is presented in Figure 3.2. The Kapton® substrate is attached to a 4 inch (101.6 mm) diameter rigid Si handle using Kapton® tape to eliminate curling and wrinkling during device fabrication. All layers are photolithographically patterned using a LOR 3A (MicroChem) and S1827 (MicroChem) bi-layer photoresist. A Ti (20 nm)/Pt (30 nm)/Au (200 nm) top ring contact (150 μm/170 μm inner/outer diameter) is deposited using e-beam evaporation and lifted off in Remover PG (MicroChem) to define the light detection area. Photodiode mesas (190 μm diameter, 314 μm pixel separation) are patterned using inductively coupled plasma (ICP) reactive-ion etching (RIE; Cl_2:H_2 = 16:12 sccm, 12 mTorr base pressure, 600 W ICP power, 100 W forward power, 0℃ stage temperature for 5 min). The back contact (100 μm width) is patterned using wet-etching for 3 min in TFA Au etchant (Transene) to connect the photodiode rows. Ohmic contacts are formed by rapid thermal annealing for 1 min at 270°C. A 1 μm thick polyimide (PI2610, HD Microsystem) passivation layer is spin-cast and cured at 300°C for 30 min. The polyimide is patterned to expose the photodiode detection area and back contact pads using ICP RIE (O_2:CF_4 = 16:56 sccm, 5 mTorr base pressure, 500 W ICP power, 10 W forward power for 6 min). The e-beam evaporated, 50 μm wide Ti (10 nm)/Au (300 nm) top contact is patterned to connect columns of photodiodes. Finally, a MgF_2 (37 nm)/TiO_2 (127 nm) bilayer anti-reflection coating (ARC) is deposited by e-beam evaporation to achieve a maximum *EQE* at $\lambda = 1300$ nm.

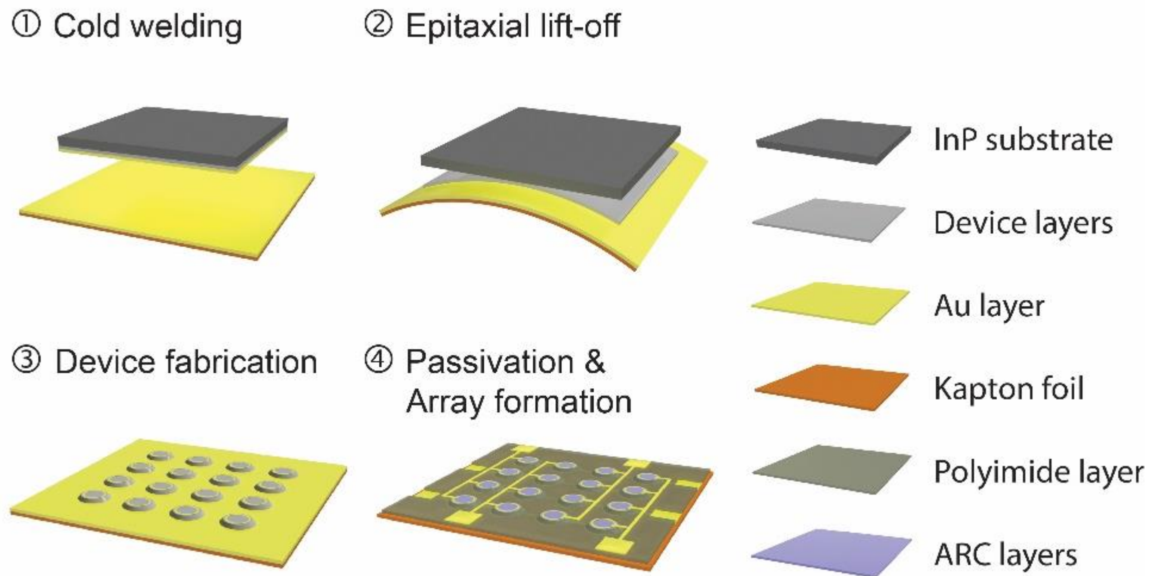

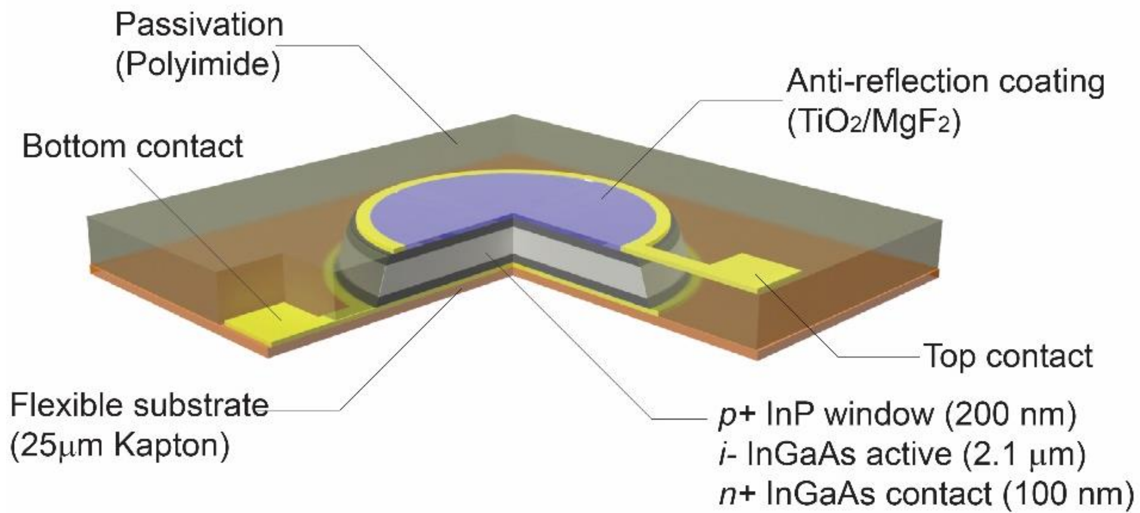

Figure 3.2: Process flow for fabrication of the thin-film InGaAs *p-i-n* photodiode array.
(top) Ir (0.5 nm)/Au (200 nm) is coated on both the epitaxial surface and the Kapton® host substrate. The metal films are brought into contact under pressure and slightly elevated temperatures to form a cold-weld bond. This is followed by epitaxial lift-off to remove the substrate from the foil. The top ring anode contact is patterned, and the photodiode mesas are etched. The back side row contacts are patterned; polyimide passivation is applied to the mesa edges and is opened to allow for deposition and pattering of the column contacts, followed by deposition of the anti-reflection coating in the device top contact rings. (bottom) Cross sectional view of a photodiode.

3.3. Photodiode Characterization

Figure 3.3 shows the thin-film 8×100 InGaAs *p-i-n* photodiode array bonded to the Kapton® foil. The array is ultra-lightweight (< 30 mg) and flexible (bend radius < 0.5 cm). The back side Au contact acts as a reflective mirror that enhances the optical absorption due to light interference in the photoactive layer. In principle, 100% peak absorption can be achieved in thin-film devices for any wavelength between 980 nm and 1650 nm by optimizing the ARC and active layer thicknesses. Here, the ARC is designed to maximize the response at $\lambda = 1300$ nm while maintaining > 85% light transmission between $\lambda = 980$ nm and 1650 nm.

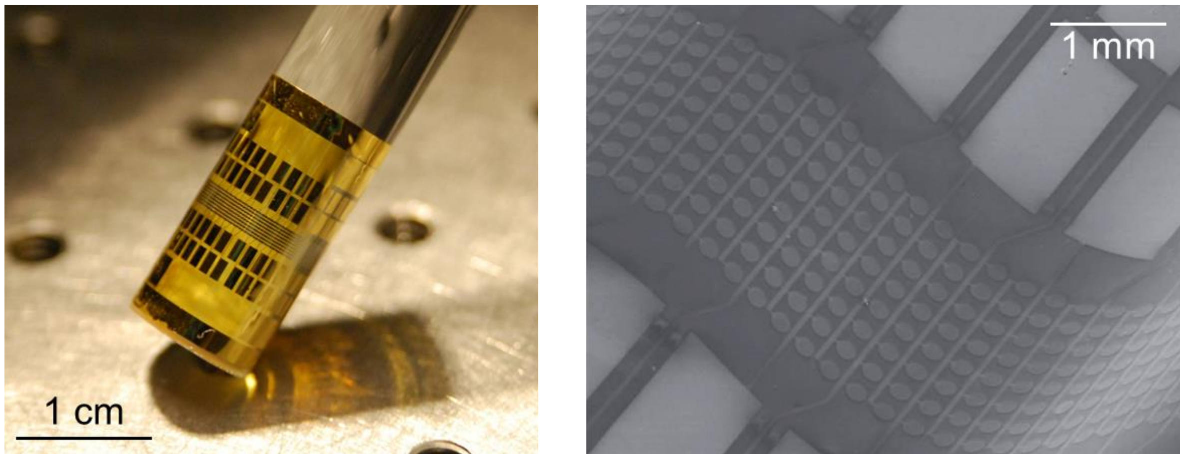

Figure 3.3: Images of an 8×100 thin-film InGaAs photodiode array fabricated on flexible Kapton® foil. (left) Photograph of an 8×100 thin-film InGaAs *p-i-n* photodiode array (right) Scanning electron microscopic image of the curved photodiode array.

Figure 3.4 shows the calculated optical intensity distribution[26] within the 2.1 μm thick InGaAs *i*-layer of the device compared with that of a substrate-based device with the same structure, clearly illustrating the improved light absorption in the thin-film device. A comparison of *EQE* at $\lambda = 1550$ nm at -1V for the thin-film devices *vs*. substrate-based devices with different InGaAs absorption layer thicknesses is shown in Figure 3.5 (left).

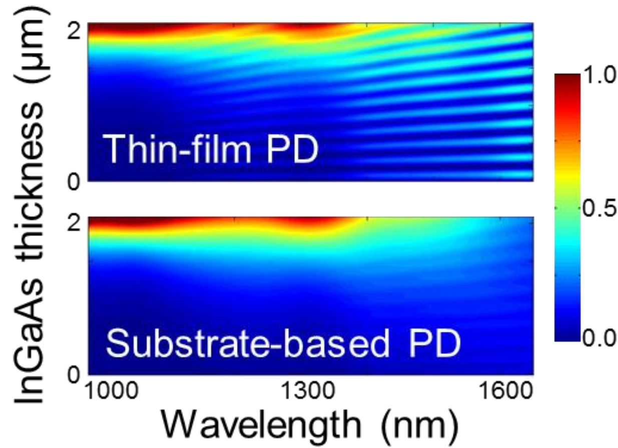

Figure 3.4: The normalized simulated optical intensity distribution.

A bi-layer antireflection coating (ARC) of MgF_2 (37 nm) and TiO_2 (127 nm) is employed for both simulated structures.

The simulated and measured *EQE* spectra of the thin-film photodiode are indicated by the line and data points in Figure 3.5 (right), respectively. The measured *EQE* are 82%, 99%, and 88% at $\lambda = 980$ nm, 1300 nm, and 1550 nm, respectively. The inset of Figure 3.5 (right) shows the current-voltage (*I-V*) characteristics of a 40 μm diameter photodiode under dark and 100 μW laser illumination at $\lambda = 1550$ nm. The dark current is 4.0 ± 0.8 nA. To our knowledge, *EQE* ~100% is the highest reported for InGaAs imagers[19,20,27,28,29].

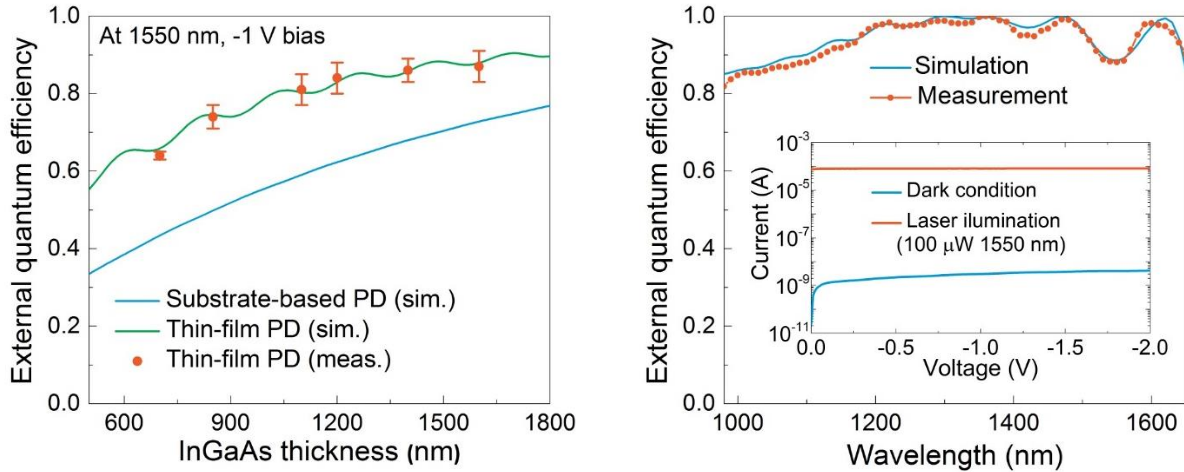

Figure 3.5: Simulated and measured external quantum efficiencies.

(left) Comparison of simulated and measured external quantum efficiencies (*EQE*) *vs*. *i*-region thickness at -1V bias and 1550 nm wavelength for thin-film (green line) and substrate-based devices (blue line). Measurements for photodiodes using a bi-layer ARC of MgF_2 (81 nm) and TiO_2 (113 nm) are shown (data points). (right) Simulated (blue line) and measured (orange dots) *EQE* spectra of the photodiode in the wavelength range from 980 nm to 1650 nm. *Inset*: Current-Voltage (*I-V*) characteristic of a 40 μm diameter photodiode in the dark (blue line) and under 100 μW, 1550 nm wavelength illumination (green line).

The current-voltage (*I-V*) characteristics under dark and 100 μW 1550 nm laser illumination are measured using an HP-4155B semiconductor parameter analyzer. Illumination, from a tunable laser source (Santec TSL-510), is guided through an SMF-28 optical fiber oriented normal to the photodiode active area using a Lightwave Probe (Cascade Microtech). External quantum efficiency from wavelengths of 980 to 1650 nm is measured under monochromatic illumination chopped at 200 Hz and coupled into an SMF-28 optical fiber. The photocurrent at -1 V is amplified by 10^5 V/A using a Keithley 428 amplifier. The output signal is collected by a lock-in amplifier (SR830). The light illumination power is calibrated using a reference InGaAs photodetector (Newport, 818-IG/DB).

3.4. Array Yield and Reliability

As shown by the histograms in Figure 3.6 (left), the yield of the 8×100 photodiode array is ~99% (790/800 photodiodes had a leakage current < 1 μA at -1 V). The high dark currents of > 1 μA in the 10 malfunctioning devices are possibly due to growth defects and/or damaged side-wall during mesa etching process. Similar yields were obtained on 10×10 photodiode arrays transferred to a Kapton® foil (Figure 3.7 (b)). In that case, the 40 μm diameter detectors on 50 μm center-to-center spacings had a 100% yield with leakage currents < 20 nA at -1V (Figure 3.6 (middle) and Figure 3.8 (b)), and an average *EQE* = 73 ± 2% (Figure 3.6 (right) and Figure 3.8 (b)). Similarly, a square array was transferred onto a *rigid* Si substrate (Figure 3.7 (a)), resulting in a 99% yield with this same range of low leakage currents (Figure 3.8 (a)). The single malfunctioning device on the Si substrate (indicated in white blank at (3,1) in Figure 3.8 (a)) is shorted.

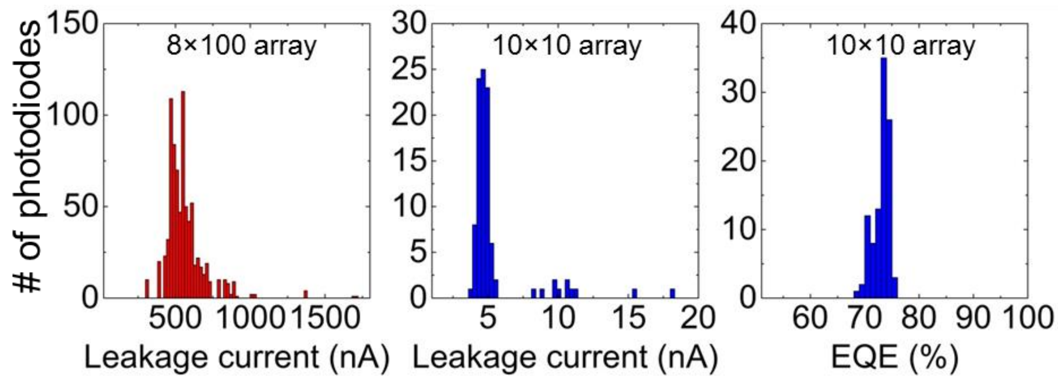

Figure 3.6: Histograms of dark current of detectors.

Histograms of dark current of detectors on the (left) 8×100 and (middle) 10×10 FPAs. Also shown (right) is a histogram of the external quantum efficiencies of diodes on the 10×10 thin-film FPA. These graphs indicate a ~99% device yield.

The 10×10 thin-film $In_{0.53}Ga_{0.47}As$ *p-i-n* photodiode arrays fabricated on both a 500 μm thick semi-insulating Si substrate and a 25 μm thick E-type Kapton® have similar fabrication processes to that of the 8×100 photodiode array, although the photodiode dimensions are different.

For the 10×10 arrays, the top ring contacts have 20 μm/30 μm inner/outer diameters that define the light detection area. Photodiode mesa diameters are 40 μm, with 100 μm pixel separations. The back side linear contacts are 5 μm wide to connect the photodiode rows, and the top linear contact columns are also 5 μm wide. A MgF_2 (81 nm)/TiO_2 (113 nm) bilayer anti-reflection coating (ARC) is employed to achieve a maximum *EQE* at $\lambda = 1550$ nm. Excluding the malfunctioning device, the average *EQE* at -1V bias and λ = 1550 nm is 88% (1.8 μm thick InGaAs active layer) and 73% (0.85 μm thick InGaAs active layer) for devices fabricated on Si and Kapton® substrates, respectively. The dark current, *EQE*, and yield of devices fabricated on these two substrates are almost identical over the entire array whether on Si or Kapton®.

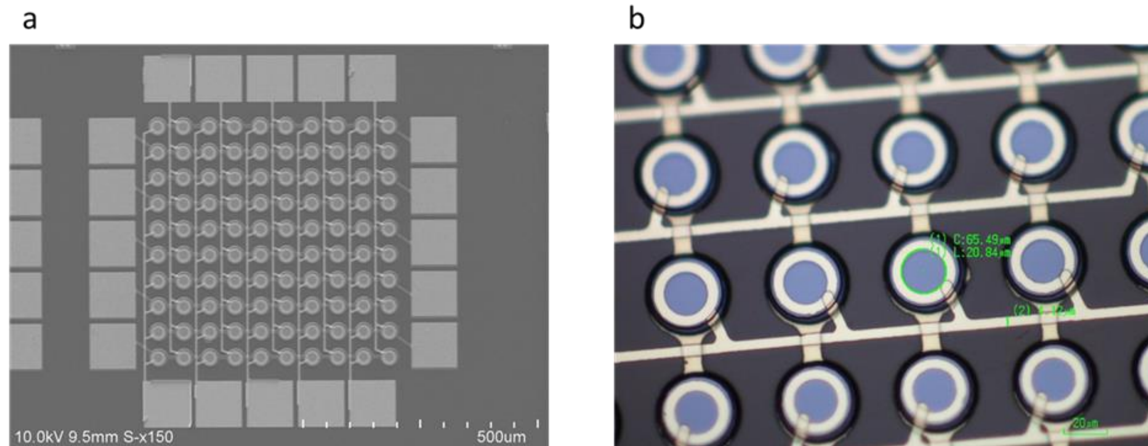

Figure 3.7: Image of the 10×10 InGaAs photodiode array fabricated on Si and Kapton substrates.
(a) Scanning electron microscopic image of the 10×10 InGaAs photodiode array fabricated on a Si substrate. (b) Microscope image of the array with the same dimensions fabricated on a flexible Kapton® substrate.

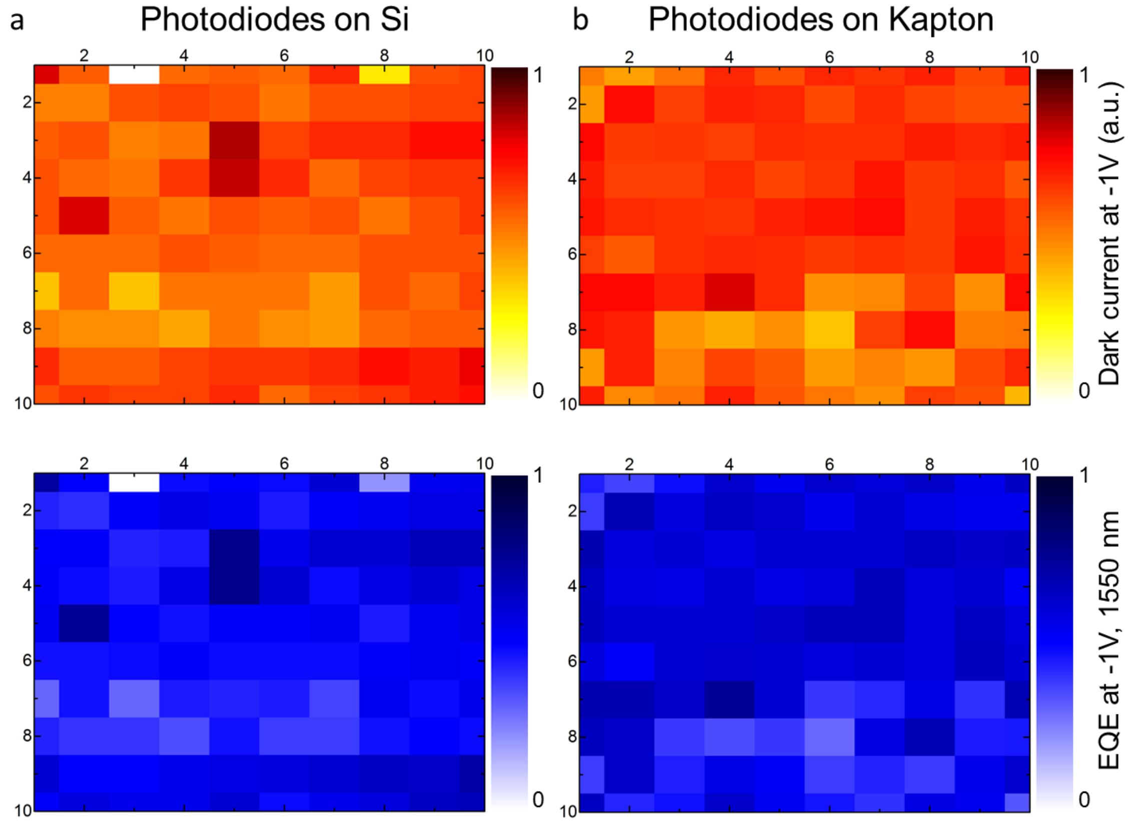

Figure 3.8: Dark current and *EQE* mapping of 10×10 InGaAs array.

Dark current (top) and external quantum efficiency (*EQE*, bottom) maps of 10×10 InGaAs array photodiodes on (a) a Si and (b) a Kapton® substrate.

The photodiode array was subjected to a burn-in test at 100ºC for 240 hr. Both dark current and *EQE* at $\lambda = 1550$ nm at -1V are measured at various intervals throughout the process. The normalized experimental results, showing the change of performance during burn-in, are almost constant within the 5% measurement error, as shown in Figure 3.9 (left). Also the performance of the array was tested before and after bending over radii ranging from 9.1 mm to 2.5 mm. Figure 3.9 (right) shows the normalized dark current and *EQE* at $\lambda = 1550$ nm at -1V following bending such that the upper half of the InGaAs active material was subjected to tensile stress and the lower half was subjected to compressive stress. No systematic performance changes are observed after bending.

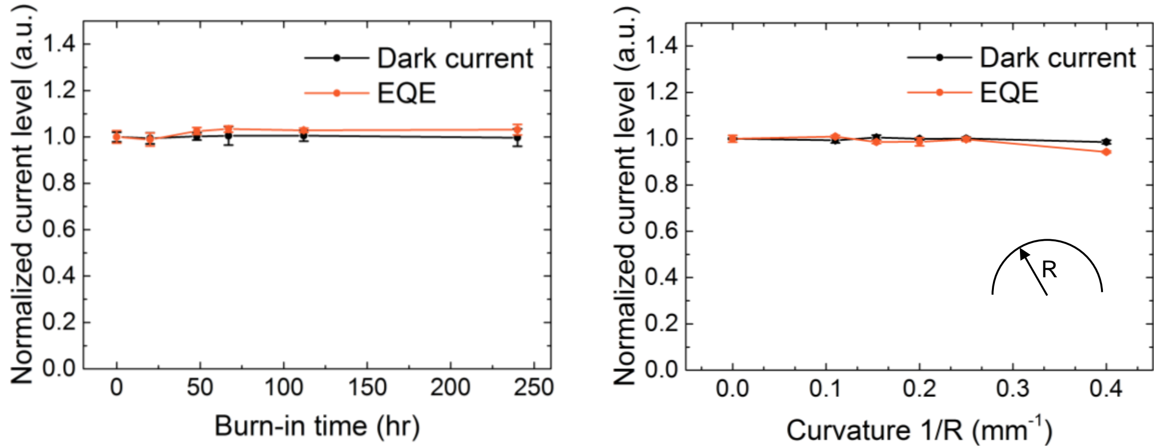

Figure 3.9: Reliability Tests.

(left) Change in normalized dark current and *EQE* under 100ºC burn-in test over 240 hr measured at 0 hr, 20 hr, 48 hr, 67 hr, 112 hr, and 240 hr. (right) Change in normalized dark current and *EQE* under different bending conditions (radius of curvature of infinity (flat), 9.1 mm, 6.5 mm, 5 mm, 4 mm, and 2.5 mm). No systematic performance change is observed in either test.

3.5. Application 1: 2π Imager

Two applications were explored that benefit from the flexibility and/or conformability of the 2D detector array that can be sharply curved into either a concave or convex format without damage. The first is in creating 2π object awareness. For the first application, the 8×100 photodiode array was wrapped into a convex, 1 cm diameter cylindrical shape to achieve a 360° (i.e. 2π) in-plane FOV.

To demonstrate this application, the 8×100 *p-i-n* thin-film InGaAs photodiode array is rolled into a 1cm diameter cylinder as shown in Figure 3.10. A 5 mW, 1550 nm wavelength laser beam is guided through an optical fiber with a numerical aperture of 0.14 to illuminate the photodiode array as it is rotated through 360°, pausing every 36° to collect an image.

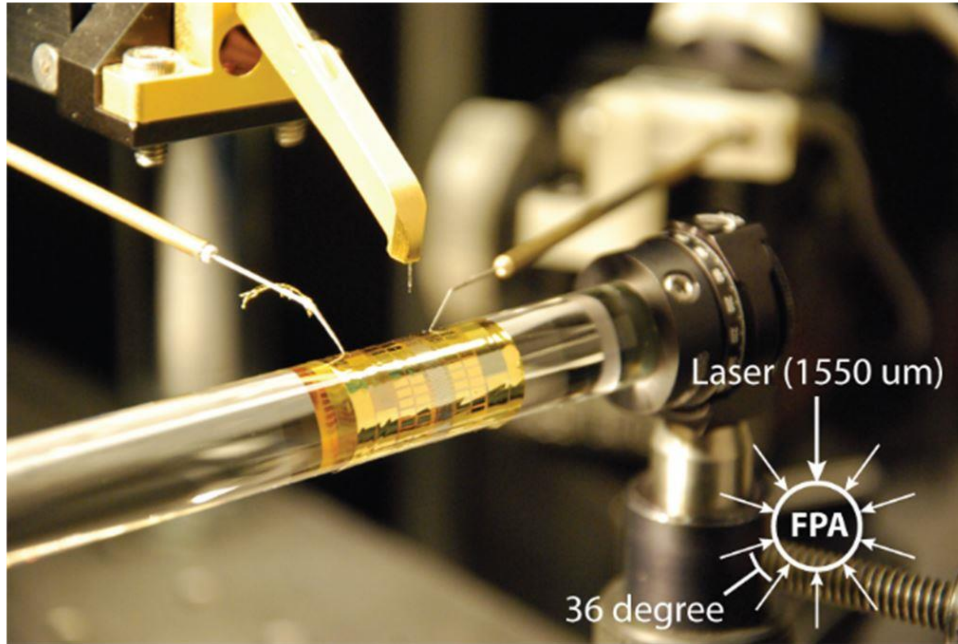

Figure 3.10: Field of view (FOV) measurement setup.

The 8×100 *p-i-n* InGaAs photodiode array is transformed to a 1 cm diameter cylindrical photodiode array. Laser light is guided through an optical fiber and normally illuminated on the array. *Inset:* Schematic illustration of the measurement.

Assuming a Gaussian beam profile at the fiber output, a beam waist diameter of 10.4 ± 0.8 µm, a 2.0 ± 0.1 cm distance from the fiber to the array, the calculated beam diameter at the array is 580 ± 25 µm. The measured beam diameter at the array surface at which the intensity drops to $1/e^2$ of its peak spans two pixels, which is consistent with the calculated result. As shown in Figure 3.11 (top), ten laser output profiles are mapped to demonstrate 2π awareness. The peak-to-peak photocurrent variations of the ten output profiles are possibly due to instabilities in laser output power and optical alignment. Figure 3.11 (bottom) shows the detected laser signal and the FOV covered by the array in both longitudinal and latitudinal directions.

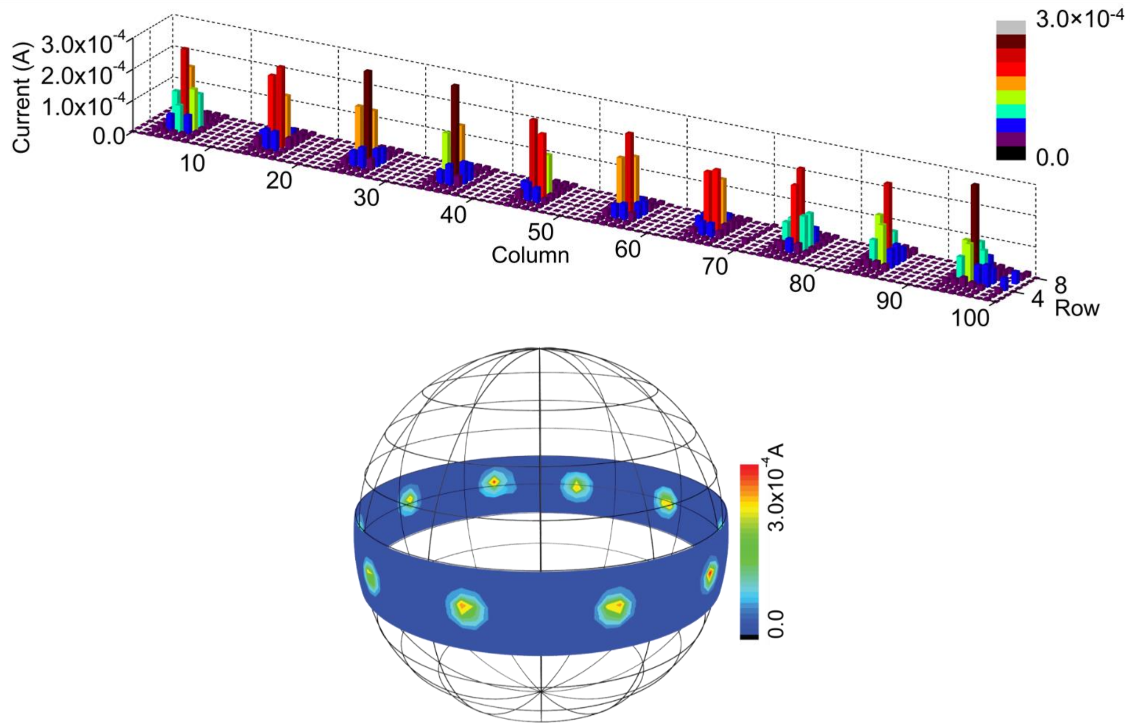

Figure 3.11: Photocurrent map of laser output profiles on a convex cylindrical 8×100 photodiode array. (top) Ten laser output profiles are shown, separated by 36º, verifying its 360º field of view (FOV). (bottom) The photocurrent response and the FOV covered by the cylindrical focal plane array in both the longitudinal and latitudinal directions.

Objects with arbitrary shapes can also be imaged as shown by Figure 3.12. A 10 mW, 1310 nm wavelength laser beam is shaped using an air-spaced achromatic doublet collimator to illuminate three shadow masks and create three stationary images on the photodiodes array as the laser beam is rotated through 360º. Each of the three 2.4 mm × 2.4 mm masks that cover 64 pixels are positioned ~1 mm from the array. The pixelated image of the letters "O", "C", and "M" are found in Figure 3.12 (a) with the setup in Figure 3.12 (b). As shown by Figure 3.12 (c), the three pixelated letters are imaged on the array by locally mapping the photocurrent of 8 by 8 photodiodes. The image is blurred possibly due to the sneak current between pixels. Figure 3.12 (d) shows the measured sneak current profile through a single mask slit. The images are then corrected by the

cancellation of sneak leakage current using the measured profile. The corrected images are shown in Figure 3.12 (e).

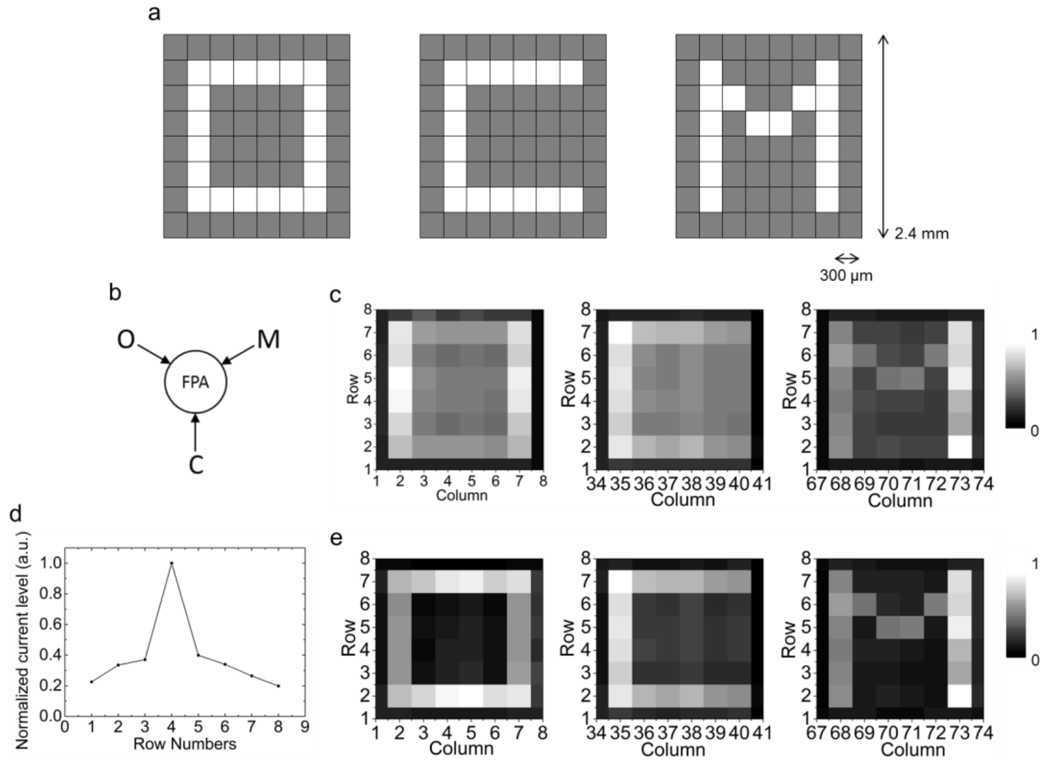

Figure 3.12: Imaging Test.

(a) Three shadow masks showing pixelated letters "O", "C", and "M". (b) Schematics of the imaging experiment setup. Laser beams illuminate on the array through three masks showing pixelated letters "O", "C", and "M" separated by 120º. (c) Photocurrent map on the array showing images of three stationary letters. (d) Sneak current profile through a single slit of the shadow mask. (e) Corrected images accounting for leakage measured in (c).

3.6. Application 2: High Resolution Spectroscopy

The second application is in high resolution spectroscopy. In a Monk-Gillieson type[30,31] spectrometer[32], the distance, *S*, from a flat diffraction grating to the focal plane is given by[30] $S = A \cdot \cos^2\theta$, where θ is the diffracted angle, $A = (f - D)/\cos^2\theta_i$, f is the focal length of the focusing component (a concave mirror or a lens), D is the distance from the focusing component to the grating, and θ_i is the light incident angle. Thus, *A*, depending on experimental arrangement,

defines the distance from the grating to the *in-focus spectral line* as shown in Figure 3.13 (left). As $\theta \to 0$, $S \to A$, whereas as $\theta \to 90^{\circ}$, $S \to 0$. This suggests that the spectral lines at large diffraction angles focus close to the grating rather than at the image plane. In contrast, a flexible FPA that is curved about an axis centered on the grating can be shaped to precisely match the focal region, maintaining focus independent of θ, as illustrated in Figure 3.13 (left). In this work, we shaped the FPA into a 2.54 cm diameter cylindrical curve (blue line) to improve its match with the focal plane compared with that of a planar array (orange line) to achieve higher spectral resolution at large diffracted angles.

The cylindrical 8×100 FPA was used to spatially resolve the outputs from three collimated laser beams at wavelengths of 980 nm, 1310 nm, and 1530 nm using the experimental arrangement in Figure 3.13 (right). The beams were shaped using air-spaced achromatic doublet collimators and a blaze reflective diffraction grating. Each laser beam was focused to a 300 ± 114 μm diameter spot, or approximately the pixel center-to-center spacing. Then, the response of the photodiodes was measured to locate the exact positions of each first-order diffraction maximum. The details of this measurement are as follows. The 8×100 FPA is conformally taped on the inner side a 2.54 cm diameter polyethylene terephthalate glycol-modified (PET-G) half tube. The array is positioned 3.4 cm from the grating to achieve a minimum *shape mismatch* with the focal plane of the grating system (see Figure 3.14). *Shape mismatch* is defined as $\sigma^2 = \int_{-30^{\circ}}^{30^{\circ}} (x_{array} - S)^2 d\theta$, where x_{array} (a function of θ) is the distance from the grating to the curved photodiode array.

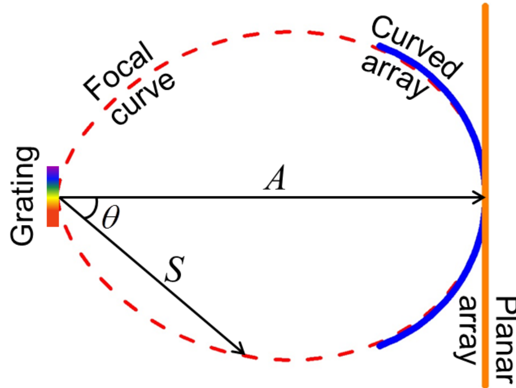

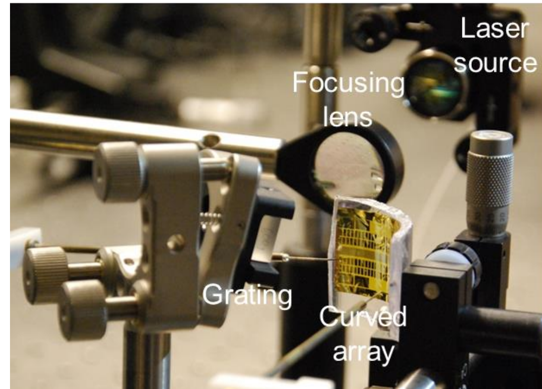

Figure 3.13: Spectroscopy Test.

(left) Spectral focal plane (dashed line) following diffraction by a blaze grating (rainbow rectangle); the detector plane of the curved focal plane array (FPA) is shown by the blue arc whose shape matches the curvature of the focal plane. A planar FPA (orange line) is shown for comparison. (right) Photograph of the spectral measurement setup. Collimated laser beams are focused and diffracted onto the curved FPA.

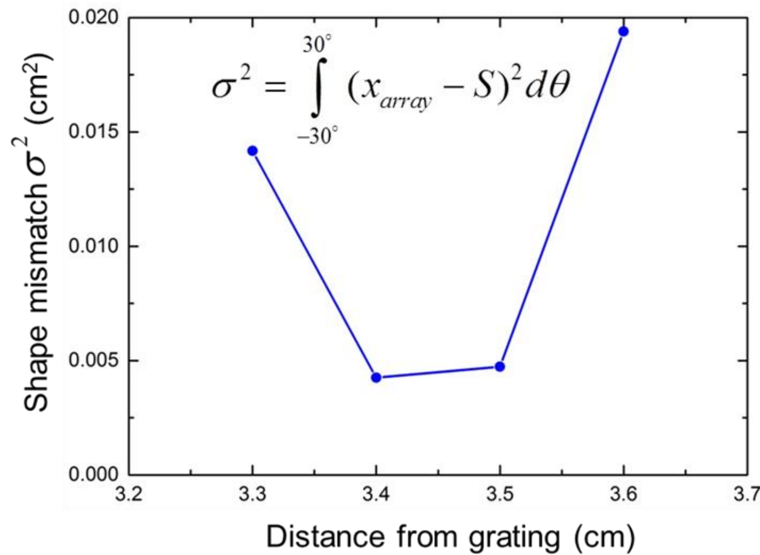

Figure 3.14: Shape mismatch vs. the position of the array.

When positioned 3.4 cm from the grating, the array achieves minimum shape mismatch with the focal plane taking into account the diffraction angles from -30° to 30°.

Three collimated diode laser beams (Thorlabs, SM-Pigtailed Butterfly Package Series) at wavelengths of 980 nm, 1310 nm, and 1530 nm are incident to the grating. Air-spaced doublet collimators (Thorlabs, F810FC-1064, F810FC-1310, and F810FC-1550 for 980 nm, 1310 nm, and 1530 nm, respectively) are used to shape the beams. An achromatic doublet (Thorlabs, AC254-

075-C) and blaze reflective diffraction grating (Thorlabs, GR13-0610, 1.59 nm/mrad dispersion) are used to focus and diffract the laser beams. The grating, located on a 360° rotational stage, is adjusted to achieve a 30° beam incident angle. The first order diffracted beams are illuminated on the 4th row of the array. The photocurrents at -1 V bias are collected using a Keithley 2400 SMU. The positions of the collimators and achromatic doublet were adjusted so that the 1530 nm beam is focused to approximately one-pixel width (confirmed by measuring the photocurrents of 5 adjacent photodiodes). After intensity peaks are mapped along the 4th row of the array, the laser source and achromatic doublet were changed to continue the measurement until all 100 photodiodes on the 4th row was measured.

Figure 3.15 shows the measured responses of the cylindrical FPA (data points), along with the simulated peak shapes (dashed lines, assuming Gaussian beam profiles) and positions (vertical, one-pixel wide bars) of the diffracted wavelength signals. The measured peaks match the simulated results within the measurement error with no evidence for systematic broadening of the full width at half maxima (FWHM). In Figure 3.15 (inset), we simulate the response near the imager edge (pixels #90 to #100) of both the cylindrical and planar FPA. Closely spaced wavelengths of 1624 nm, 1644 nm, and 1663 nm (corresponding to diffraction angles of 28.32^{o}, 29.10^{o}, and 29.85^{o} centered at pixels #94, #96, and #98, respectively) have 46.6%, 49.6%, and 53.3% mismatches between the focal distance, *S*, and the array-to-grating distances at their corresponding diffraction angles to the planar FPA, respectively. This corresponds to a greater than four pixel defocusing penalty, limiting the wavelength resolution to > 44 nm. In contrast, mismatch between *S* and the array-to-grating distance of these same wavelengths to the cylindrical FPA are only 4.8%, 0.1%, and 0.5%, respectively, corresponding to a wavelength resolution smaller than 11 nm.

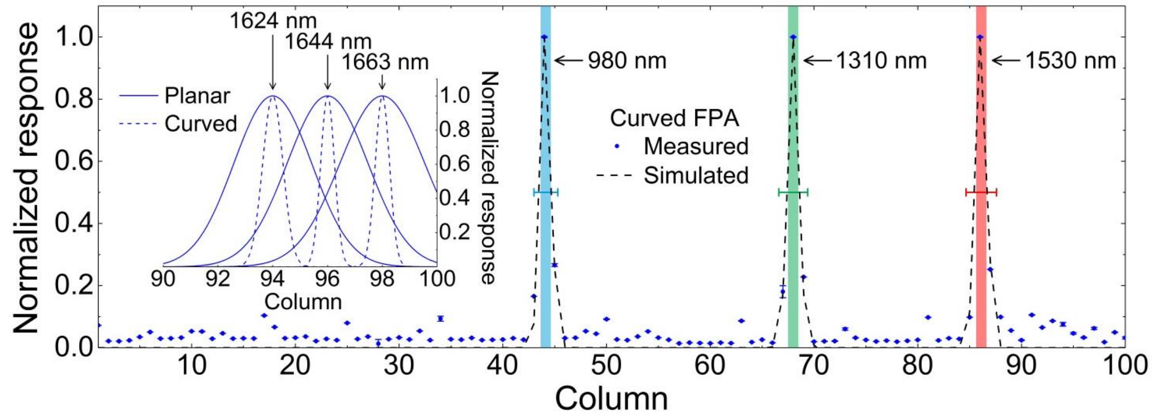

Figure 3.15: Resolution Improvement.

Simulated (dashed line, assuming Gaussian beam profiles) and measured (data points) photocurrent response (normalized) of the cylindrically curved FPA. Also shown are the simulated one-pixel width diffraction peaks (vertical bars) positions at three different wavelengths of 980 nm, 1310 nm and 1530 nm. *Inset:* Simulated response from pixels #90 to #100 on a cylindrical (dashed line) and a planar (solid line) FPA at three closely spaced wavelengths.

From Figure 3.13 (left), it is apparent that a curved FPA can provide a far wider spectral coverage than a planar FPA with the same number of pixels. That is, since each wavelength increment $\Delta\lambda$ subtends an angle $\Delta\theta$ about a central diffraction angle q, the subtended linear increment Δl on a planar FPA is then $\frac{\Delta l}{A} \approx \sec^2\theta \cdot \Delta\theta$. Hence, Δl increases dramatically with $\Delta\theta$ in the limit of large θ. In contrast, the curved FPA follows $\frac{\Delta l}{A} \approx \Delta\theta$, a function that is independent of diffraction angle θ.

Figure 3.16 (left) shows the wavelength coverage of both planar and curved FPAs using a 1200 grooves/mm diffraction grating. The array length required of an FPA curved to match the focal surface of the grating increases very slowly and approximately linearly with wavelength. Hence an 8.8 cm long array achieves coverage from 800 nm to 1600 nm, whereas the planar FPA length is dramatically increased 23.3 cm with a correspondingly larger number of pixels. The calculation details are as follows. We assume a diffraction grating with blazed at $g = 1200$

grooves/mm. Both the planar and the curved array have a pixel spacing of 300 μm, and are placed at a distance, $L = 3.4$ cm, from the diffraction grating.

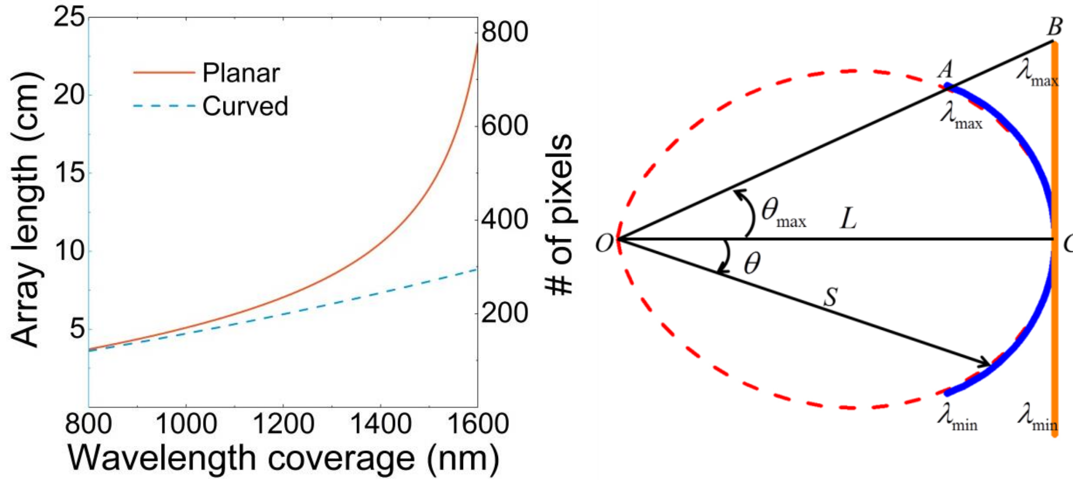

Figure 3.16: Wavelength coverage comparison.

(left) Comparison of the array length *vs.* wavelength coverage required for a curved (dashed line) and a planar (solid line) FPA. The corresponding number of pixels required (right vertical axis) is also shown, assuming a pixel spacing of 300 μm. Note the dramatic divergence in array size as the wavelength span is increased. (right) Schematic of the geometry used in the wavelength coverage comparison. For a curved (blue) and a planar (orange) array, the required array lengths to cover a wavelength range are 2*BC* and 2*AC*, respectively.

The grating equation gives:

$$(\sin\theta_i + \sin\theta) = \lambda \cdot g \tag{3.1}$$

where θ_i is the light incident angle, θ is the light diffraction angle, and λ is the diffracted wavelength such that:

$$\lambda = \frac{\sin\theta_i}{g} + \frac{\sin\theta}{g} \tag{3.2}$$

Since the first term is a constant depending on the experiment setup, then we have simply:

$$\lambda = \frac{\sin\theta}{g} \tag{3.3}$$

although θ_i has restrictions to make the equation physically meaningful, i.e. $\lambda > 0$.

For a planar array, as illustrated in Figure 3.16 (right), the wavelength coverage, λ_c, is,

$$\lambda_c = \lambda_{\max} - \lambda_{\min} \tag{3.4}$$

where $\lambda_{\max}$ and $\lambda_{\min}$ are the maximum and minimum wavelengths covered by the arrays.

Thus, from Eq. (3.3):

$$\lambda_c = \frac{\sin\theta_{\max} - \sin\theta_{\min}}{g} \tag{3.5}$$

where $\theta_{\max}$ and $\theta_{\min}$ are the corresponding diffraction angles of $\lambda_{\max}$ and $\lambda_{\min}$, respectively.

Assuming that the grating normal, *OC*, is at the center of the array, it is apparent that:

$$\theta_{\min} = -\theta_{\max} \tag{3.6}$$

Thus, Eq. (3.5) is simplified to:

$$\lambda_c = \frac{2\sin\theta_{\max}}{g} \tag{3.7}$$

Also illustrated in Figure 3.16 (right) is that:

$$\tan\theta_{\max} = \frac{BC}{OC} = \frac{BC}{L} \tag{3.8}$$

Therefore, combining Eqs. (3.7) and (3.8), the required array length, $2BC$, to provide enough coverage for λ_c is:

$$2BC = L \cdot \tan(\sin^{-1}(\frac{\lambda_c \cdot g}{2})) \tag{3.9}$$

For a curved array matching the focal surface of the grating system, the shape of the array in polar coordinates is:

$$S = L \cdot \cos^2 \theta \tag{3.10}$$

The required array length, $2AC$, is therefore:

$$2AC = \int_{-\theta_{\max}}^{\theta_{\max}} \sqrt{S^2 + (\frac{dS}{d\theta})^2} d\theta \tag{3.11}$$

A simultaneous solution of Eqs. (3.11), (3.10) and (3.7) yields the required array length, $2AC$ as a function of required wavelength coverage, λ_c.

3.7. Conclusion

In summary, we demonstrated a thin-film InGaAs *p-i-n* photodiode array fabricated on a thin, flexible Kapton® foil substrate. The array is transformed into a cylindrical shape to achieve a 360° FOV to achieve the ultimate 2π in-plane image awareness. The curved array was also used to improve focusing with enhanced wavelength coverage in a spectrophotometer application in comparison to a conventional planar array. Thin-film InGaAs photodiodes, employing a back side mirror dramatically enhanced the detector responsivity achieving *EQE* ~100% over a wide SWIR spectral range. A pixel spacing of 50 μm with a 40 μm mesa diameter was achieved using a manually aligned lithography tool with ~10 μm alignment tolerance. Smaller pixel spacings of < 5 μm, which is orders of magnitude smaller than state-of-art conformal photodetector arrays[6,9,7], are achievable using lithographic tools with higher resolution owing to the simplified ELO + precise cold-welding transfer methods that eliminate the brittle and significant bonding resolutions inherent in indium solder-bump technology. Additionally, transistor readout pixels can also be

integrated with each photodiode in the array on the parent wafer, and then transferred in a single step using the same fabrication methods as described here[15]. The unique features of this flexible and lightweight FPA enable advanced and simplified optical designs with exceptional FOV and significantly reduced aberrations, making it suitable for a wide variety of applications that cannot be accessed using planar arrays that are the foundation of current imaging systems.

CHAPTER 3

Bibliography

1. Rim, S.-B., Catrysse, P. B., Dinyari, R., Huang, K. & Peumans, P. The optical advantages of curved focal plane arrays. *Opt. Express* **16**, 4965 (2008).

2. Swain, P. K., Channin, D. J., Taylor, G. C., Lipp, S. A. & Mark, D. S. Curved CCDs and their application with astronomical telescopes and stereo panoramic cameras. *Proc. SPIE* vol. 5301 109–129 (2004).

3. Brady, D. J. *et al.* Multiscale gigapixel photography. *Nature* **486**, 386–389 (2012).

4. Wong, W. & Salleo, A. *Flexible electronics: materials and applications*. (Springer US, 2009).

5. Yoon, J. *et al.* Heterogeneously Integrated Optoelectronic Devices Enabled by Micro-Transfer Printing. *Adv. Opt. Mater.* **3**, 1313–1335 (2015).

6. Xu, X., Davanco, M., Qi, X. & Forrest, S. R. Direct transfer patterning on three dimensionally deformed surfaces at micrometer resolutions and its application to hemispherical focal plane detector arrays. *Org. Electron.* **9**, 1122–1127 (2008).

7. Ko, H. C. *et al.* A hemispherical electronic eye camera based on compressible silicon optoelectronics. *Nature* **454**, 748–753 (2008).

8. Saito, H., Hoshino, K., Matsumoto, K. & Shimoyama, I. Compound eye shaped flexible organic image sensor with a tunable visual field. *18th IEEE International Conference on Micro Electro Mechanical Systems, 2005. MEMS 2005.* 96–99 (2005).

9. Floreano, D. *et al.* Miniature curved artificial compound eyes. *Proc. Natl. Acad. Sci.* **110**, 9267–9272 (2013).

10. Dinyari, R., Rim, S.-B., Huang, K., Catrysse, P. B. & Peumans, P. Curving monolithic silicon for nonplanar focal plane array applications. *Appl. Phys. Lett.* **92**, (2008).

11. Song, Y. M. *et al.* Digital cameras with designs inspired by the arthropod eye. *Nature* **497**, 95–99 (2013).

12. Jin, H. C., Abelson, J. R., Erhardt, M. K. & Nuzzo, R. G. Soft lithographic fabrication of an image sensor array on a curved substrate. *J. Vac. Sci. Technol. B* **22**, (2004).

13. Kim, C., Burrows, P. E. & Forrest, S. R. Micropatterning of Organic Electronic Devices by Cold-Welding. *Sci.* **288**, 831–833 (2000).

14. Konagai, M., Sugimoto, M. & Takahashi, K. High efficiency GaAs thin film solar cells by peeled film technology. *J. Cryst. Growth* **45**, 277–280 (1978).

15. Lee, K., Zimmerman, J. D., Hughes, T. W. & Forrest, S. R. Non-Destructive Wafer Recycling for Low-Cost Thin-Film Flexible Optoelectronics. *Adv. Funct. Mater.* **24**, 4284–4291 (2014).

16. Rogalski, A. Progress in focal plane array technologies. *Prog. Quantum Electron.* **36**, 342–473 (2012).

17. Rogalski, A., Antoszewski, J. & Faraone, L. Third-generation infrared photodetector arrays. *J. Appl. Phys.* **105**, (2009).

18. Coussement, J. *et al.* New developments on InGaAs focal plane array. *Proc. SPIE* vol. 9070 907005–907009 (2014).

19. Wang, Y.-S., Chang, S.-J., Chiou, Y.-Z. & Lin, W. Noise Characteristics of High-Performance InGaAs PIN Photodiodes Prepared by MOCVD. *J. Electrochem. Soc.* **155**, J307 (2008).

20. Onat, B. M. *et al.* Ultra-low dark current InGaAs technology for focal plane arrays for low-light level visible-shortwave infrared imaging. *Proc. SPIE* vol. 6542 65420L-65420L–9 (2007).

21. Dowrey, A. E., Story, G. M. & Marcott, C. Industrial Applications of Near-IR Imaging. in *Spectrochemical Analysis Using Infrared Multichannel Detectors* 175–188 (Blackwell Publishing Ltd, 2005).

22. Blake, T. *et al.* Utilization of a Curved Focal Surface Array in a 3.5m Wide Field of View Telescope. *Proc. Adv. Maui Opt. Sp. Surveill. Technol. Conf.* (2013).

23. Matthews, J. W. & Blakeslee, A. E. Defects in epitaxial multilayers: I. Misfit dislocations.

J. Cryst. Growth **27**, 118–125 (1974).

24. Haisma, J. & Spierings, G. A. C. M. Contact bonding, including direct-bonding in a historical and recent context of materials science and technology, physics and chemistry. *Mater. Sci. Eng. R Reports* (2002).

25. Smith, J. R., Bozzolo, G., Banerjea, A. & Ferrante, J. Avalanche in adhesion. *Phys. Rev. Lett.* (1989).

26. Peumans, P., Yakimov, A. & Forrest, S. R. Small molecular weight organic thin-film photodetectors and solar cells. *J. Appl. Phys.* **93**, (2003).

27. Martin, T., Dixon, P., Gagliardi, M.-A. & Masaun, N. 320x240 pixel InGaAs/InP focal plane array for short-wave infrared and visible light imaging. *Proc. SPIE* vol. 5726 85–91 (2005).

28. Martin, T., Brubaker, R., Dixon, P., Gagliardi, M.-A. & Sudol, T. 640x512 InGaAs focal plane array camera for visible and SWIR imaging. *Proc. SPIE* vol. 5783 12–20 (2005).

29. Seshadri, S. *et al.* Characterization of NIR InGaAs imager arrays for the JDEM SNAP mission concept. *Proc. SPIE* vol. 6276 62760S-62760S–8 (2006).

30. Monk, G. S. A mounting for the plane grating. *J. Opt. Soc. Am.* **17**, 358–362 (1928).

31. Gillieson, A. H. C. P. A New Spectrographic Diffraction Grating Mounting. *J. Sci. Instrum.* **26**, 335 (1949).

32. Kaneko, T., Namioka, T. & Seya, M. Monk-Gillieson Monochromator. *Appl. Opt.* **10**, 367–381 (1971).

Chapter 4

A Retina-Like Hemispherical Focal Plane Array

Optoelectronic circuits in three-dimensional (3D) shapes with large deformations can offer new functionalities inaccessible to conventional planar electronics based on two-dimensional (2D) geometries constrained by conventional photolithographic patterning processes. A light sensing focal plane array (FPA) used in imagers is one example of a system that can benefit from fabrication on curved surfaces. By mimicking the hemispherical shape of the retina in the human eye, a hemispherical FPA provides a low-aberration image with wide field of view. Here we report a general approach for fabricating electronic circuits and optoelectronic devices on non-developable surfaces by introducing shear-slip of thin-film circuits components relative to the distorting substrate. In particular, we demonstrate retina-like imagers that allow for a topological transformation from a plane to a hemisphere without changing the relative positions of the pixels from that initially laid out on a planar surface. As a result, the resolution of the imager, particularly in the foveal region, is not compromised by stretching or creasing that inevitably results in transforming a 2D plane into a 3D geometry. The demonstration provides a general strategy for realizing high density integrated circuits on randomly shaped, non-developable surfaces.

4.1. Introduction

One extensively studied system that benefits from being shaped into a non-developable hemispherical architecture is the image sensing focal plane array (FPA). It offers significant benefits if a retinal shape can be achieved without changing the interpixel spacing that results in loss of image resolution or image distortion. The retina is the nearly hemispherical light sensitive three-layer structure on the back of human eye on which an image is focused by the lens[1]. In contrast to the shape and size of the retina, high performance photodetector FPAs employed in modern cameras are flat due to limitations of conventional photolithographic fabrication. The imperfect match between planar FPAs and image planes using only a single element convex lens such as that in the human eye results in a degraded image with a limited range of focus, a narrow field of view (FOV), and off-axis optical aberrations[2–5]. Consequently, additional optical elements are required to correct these aberrations that increase the complexity, weight and cost, while often decreasing the functionality of the imaging system.

Many efforts, therefore, have been made to shape the FPA into a hemisphere[6–15]. Fabricating arrays on retina-like hemispherical surfaces[10,11,16,17], however, introduces significant challenges. For example, thinning and deforming commercial CMOS imagers[9,17] (with integrated addressing circuits) provides a high pixel count, although the curvature must remain small to avoid the significant mechanical strain, or distortions such as creasing or folding. Changes in pixel separation that must be corrected to avoid image artifacts, and resolution loss associated with strain are also unavoidable. Larger deformations from a plane to a hemisphere have been achieved by placing bendable and stretchable metal interconnection "bridges" between pixels that relieve strain to create both concave[11] and convex[18] imagers. However, the gaps between pixels reserved for the bridges result in a loss of resolution, particularly near the central "fovea" at the point of maximum

strain. Recently, Origami-inspired hemispherical FPAs were reported[12,13,19] with high deformability and pixel counts that were achieved by cutting, folding and mating sections to form an approximately hemispherical shape. This process does not result in a perfect conformation to a hemisphere, leading to undesirable optical aberrations and image stitching errors.

In this work, we overcome these deficiencies by employing well-established optoelectronics processing techniques to form a thin-film, GaAs FPA on planar, flexible plastic foils. The hemispherical FPA (HFPA) is then achieved by transferring to an elastomeric handle, and then allowing the circuits to shear and slip along the elastomeric surface during distortion; a method first introduced in making organic thin-films detector arrays[10]. Specifically, a 15×15 thin-film GaAs photodiode FPA was fabricated on a flexible Kapton® foil via cold-weld bonding[20], and subsequently non-destructively epitaxially lifted off (ND-ELO)[21,22] from its parent (growth) substrate. The flexible FPA, attached to an elastomeric transfer handle with rows of detectors separated by plasma etching, is then deformed into a hemispherical shape that allows for shear slippage between the elastomer and the array surface and then is transferred to a mating concave hemispherical substrate to achieve the HFPA. The HFPA shows nearly perfect fabrication yield (~99%) and an external quantum efficiency $EQE > 80\%$ between wavelengths of 650 and 900 nm. Moreover, the noise performance and detectivity are both comparable to commercially available charge coupled detector (CCD) imagers[23]. Note that the fabrication strategy is independent of the semiconductor materials choice and can achieve the same high pixel density on almost any arbitrarily shaped surface as on a planar surface with a continuous first and second derivative.

4.2. Hemispherical Focal Plane Array (HFPA) Fabrication

A GaAs *p-n* junction photodiode array is first fabricated on a flexible, 25 µm thick E-type Kapton® substrate. Details of the array fabrication process are as follows. The photodiode array employs a 200 nm undoped GaAs buffer layer, 25 nm undoped AlAs sacrificial layer, 25 nm Si-doped (5×10^{18} cm^{-3}) GaAs contact layer, 25 nm Si-doped (1×10^{18} cm^{-3}) $In_{0.49}Ga_{0.51}P$ window layer, 150 nm Si-doped (1×10^{18} cm^{-3}) GaAs emitter layer, 2.5 µm Zn-doped (2×10^{17} cm^{-3}) GaAs base layer, 100 nm Zn-doped (6×10^{17} cm^{-3}) $Al_{0.26}Ga_{0.74}As$ back surface field layer, and 200 nm C-doped (5×10^{18} cm^{-3}) GaAs contact layer that are consecutively grown on an undoped (100) GaAs substrate using molecular beam epitaxy.

Following growth, the surface native oxide is removed in buffered HF for 90 s and rinsed in de-ionized (DI) water for 10 s. A 200 nm Au layer is deposited using e-beam evaporation on the epitaxial surface, and 5 nm Ir and 200 nm Au layers are sputtered onto a 25 µm E-type Kapton® foil. The GaAs sample with epitaxial layer is bonded to Kapton® foil by applying heat (200°C) and pressure (2 MPa) for 5 min under vacuum (10^{-4} mTorr) using an EVG 510 wafer bonder (EV Group Inc., NY, 12203). The bonded sample is then immersed in 17% HF solution maintained at 60°C with 400 rpm agitation for 3 hrs to remove the AlAs sacrificial layer, thereby separating the epitaxial layers from the parent GaAs wafer using non-destructive epitaxial lift-off (ND-ELO)[22].

The Kapton® substrate is fixed to a rigid Si handle to eliminate curling. All layers are photolithographically patterned using LOR 3A (MicroChem Corp., MA, 01581) and SPR 220 3.0 ((MicroChem Corp., MA, 01581) bilayer photoresist. Photodiode mesas (150 µm diameter, 300 µm pixel pitch) are patterned using inductively coupled plasma (ICP) reactive-ion etching (RIE; Cl_2:Ar_2:BCl_3 = 2:5:10 sccm, 5 mTorr pressure, 500 W ICP power, 100 W forward power, 0°C

stage temperature for 7 min). The back contact lines (50 μm wide) are wet etched using TFA Au etchant (Transene Company Inc., MA, 01923) to pattern photodiode rows. A 1.2 μm thick polyimide (PI2610, HD Microsystem, NJ, 08859) insulation layer is spin-cast and cured at 250°C for 5 hrs. The polyimide layer is patterned to expose the light detection area and back contact pads using O_2 plasma (O_2 = 80 sccm, 800 W ICP power, 300 mTorr pressure, 150°C stage temperature for 10 min). Next, the Ti (10 nm) / Au (500 nm) top contact ring is deposited onto the photodiode mesas. A TiO_2 (49 nm) / MgF_2 (81 nm) anti-reflection coating is then patterned on the light detection area. A Ti (10 nm)/ Al (200 nm) etch mask is deposited onto the reverse side of the Kapton® substrate with a pattern that matches the photodiode rows and contact lines on the front substrate surface. Photodiode mesas on the array are connected only in rows, whereas the column connections are not patterned at this point (see Figure 4.1).

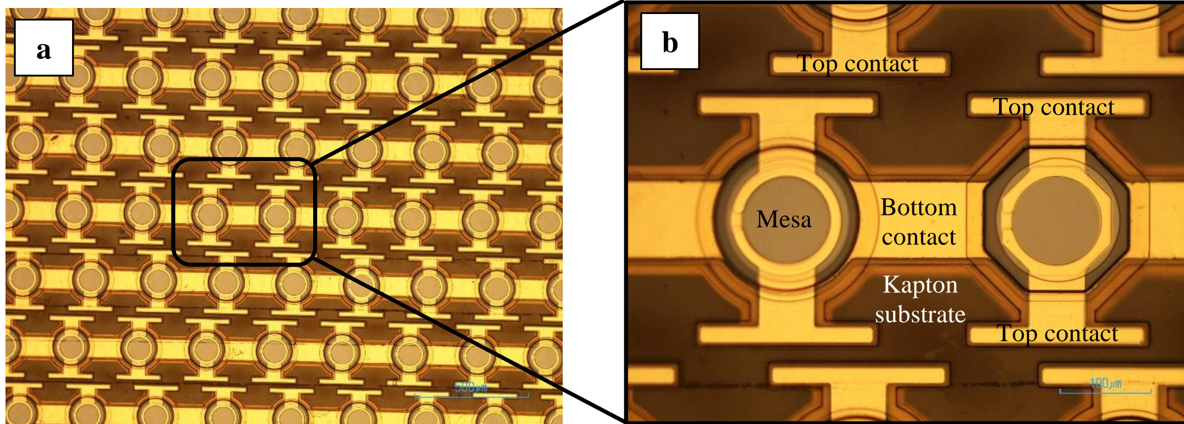

Figure 4.1: Microscopic image of photodiodes array connected in rows.
(a) Microscopic image of photodiodes array connected in rows patterned on 25 μm Kapton substrate. (b) Exploded view of individual photodiode layout. Electrical connections have not been patterned to connect rows of photodiodes.

Separately, a 100 μm PDMS (Sylgard 184, base to curing agent weight ratio = 10 : 1) membrane is spun (800 rpm) on a Si handle pre-treated with a release agent (tridecafluoro-1,1,2,2-

tetrahydrooctyl trichlorosilane), and cured at 100°C for 3 hrs. The Kapton® substrate with the detectors facing the membrane is then attached to the PDMS[24,25] as shown by Figure 4.2 (a). The Kapton® area not covered by the Al mask is removed to separate photodiode rows using O_2 plasma (O_2 = 20 sccm, 6 mTorr pressure, 500 W ICP power, 100 W forward power, 0°C stage temperature for 25 min). The Al mask is then removed using Cl_2 plasma (H_2:Cl_2:Ar = 12:9:5 sccm, 10 mTorr pressure, 500 W ICP power, 100 W forward power, 0°C stage temperature for 2 min) as shown by Figure 4.2 (b). This step removes the Kapton® substrate between the rows of detectors, i.e. separates a two-dimensional array plane into individual one-dimensional lines of detectors.

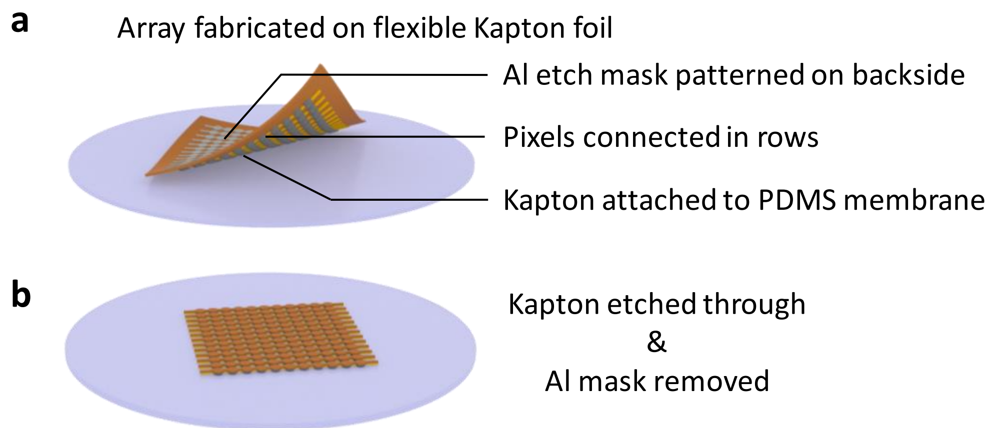

Figure 4.2: Schematic illustration of the key steps of fabricating a hemispherical photodiode array. (a) GaAs *p-n* junction photodiodes array connected in rows fabricated on flexible Kapton® substrate (brown) with Al etch mask (light gray) patterned on the backside is laid flat onto a poly(dimethylsiloxane) (PDMS) membrane (purple). (b) The Kapton® substrate is etched through to the PDMS surface using O_2 plasma. Al etch mask is removed using Cl_2 plasma.

Then, a thin layer of NOA 84 optical adhesive (4000 rpm, Norland Products) is spin-coated, and pre-cured using UV light (0.15 W/cm^2, 1 cm from the sample surface, 2 min) to partially harden the adhesive. The PDMS membrane is peeled from the Si handle, and attached to the bottom of a 3D printed holder (0.5 mm thick, 4 cm × 4 cm square shape with a 2 cm diameter clear aperture

in the center for device transfer). The same uncured PDMS is also poured into a plano-concave lens (Thorlabs, LC4942, 12.7 mm diameter, 9.2 mm surface curvature, 4.4 mm edge thickness, 2.0 mm center thickness), and cured at 100°C for 3 hr to form a hemispherical transfer punch. The membrane is then deformed by the centered PDMS punch as shown in Figure 4.4 (a). The PDMS membrane thus undergoes a topological stretching into a non-developable surface[26] in spite of significant strain (~7% in the center, and ~20% towards the edge, see Figure 4.3).

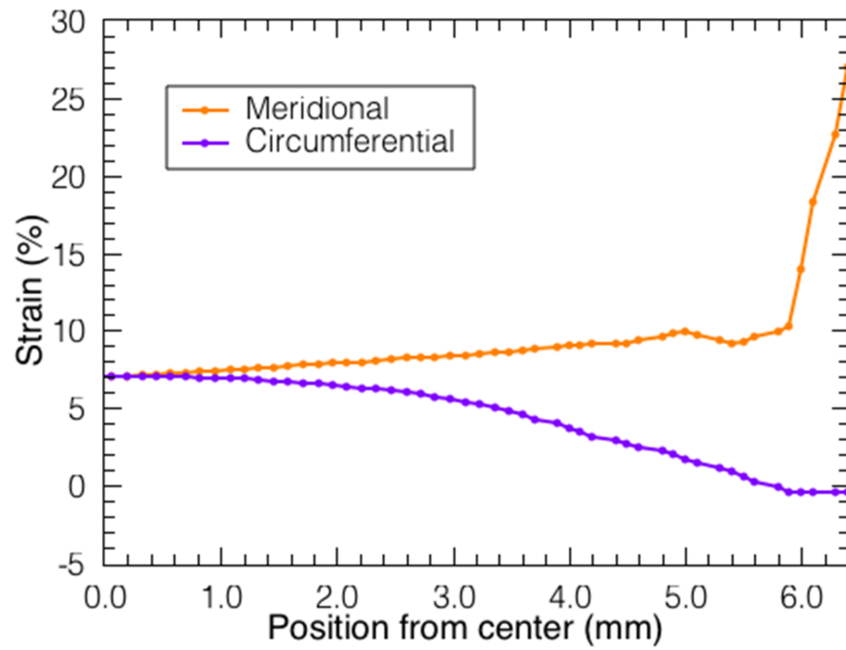

Figure 4.3: Simulated meridional and circumferential strain.

Simulated meridional and circumferential strain in the poly(dimethylsiloxane) (PDMS) membrane upon deformation to the final hemispherical shape using Ansys. The meridional strain in the center is ~7% and it increases dramatically to over 20% towards the edge of the hemisphere.

The pixels, however, do not change their spacing during stretching. The inset of Figure 4.4 (a) shows cross-sectional views of the array and PDMS membrane in XZ and YZ-planes. In the XZ-plane, detectors (gray) together with in-row connections (yellow) and the etched Kapton® (brown) move freely along the X-direction without longitudinal strain when the PDMS membrane

(blue) is stretched. In the YZ-direction, however, the detectors and connections are constrained by the Kapton® film, and hence they shear along the PDMS stretched in the Y-direction. The shear along the membrane surface is allowed without strain due to the weak adhesion at the detector/PDMS interface (see Figure 4.5)[10].

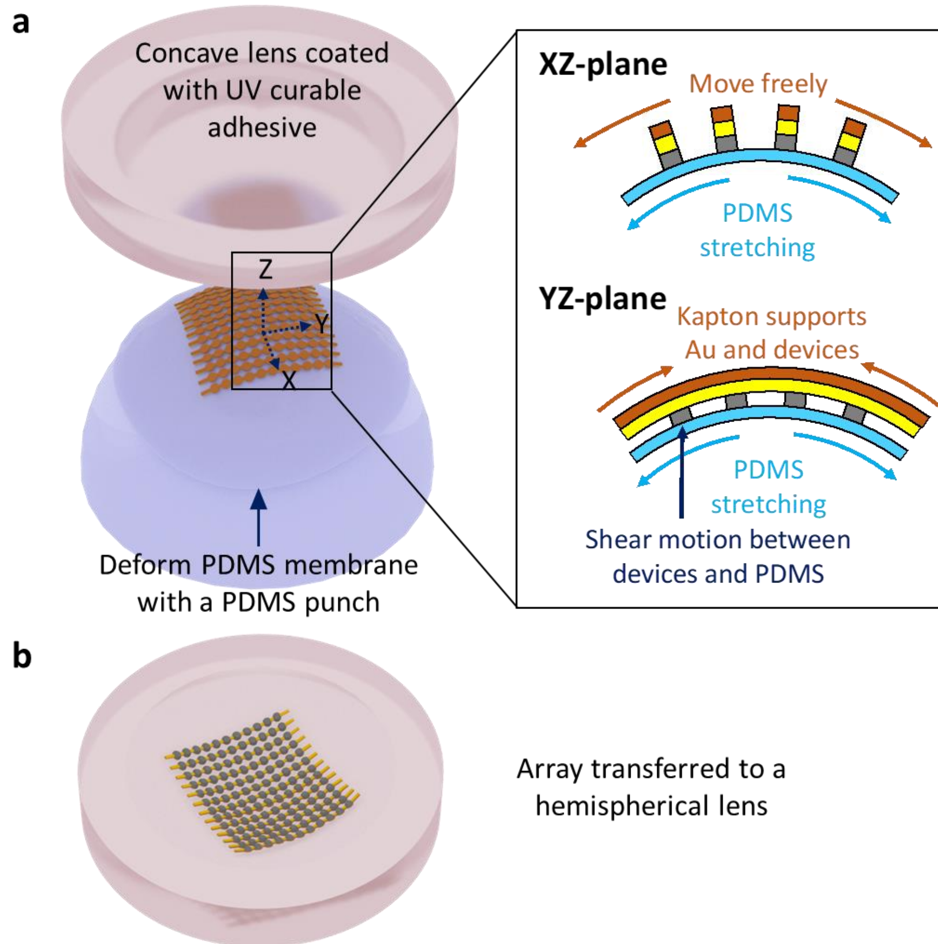

Figure 4.4: Schematic illustration of the key steps of deformation.

(a) The PDMS membrane that supports the array is fixed on its edges and deformed by a centered PDMS hemispherical punch. The array is transferred to a matching hemispherical concave glass lens coated with UV curable adhesive. Inset: Cross-section views from XZ-plane and XY-plane during the deformation process. Kapton® substrate (brown) supports Au connection lines (yellow) and photodiodes mesas (gray) when PDMS membrane (blue) is stretched. Rows of pixels are free to move in X-direction and have shear motion with PDMS membrane in Y-direction. (b) Array (connected in rows) transferred to the concave glass lens.

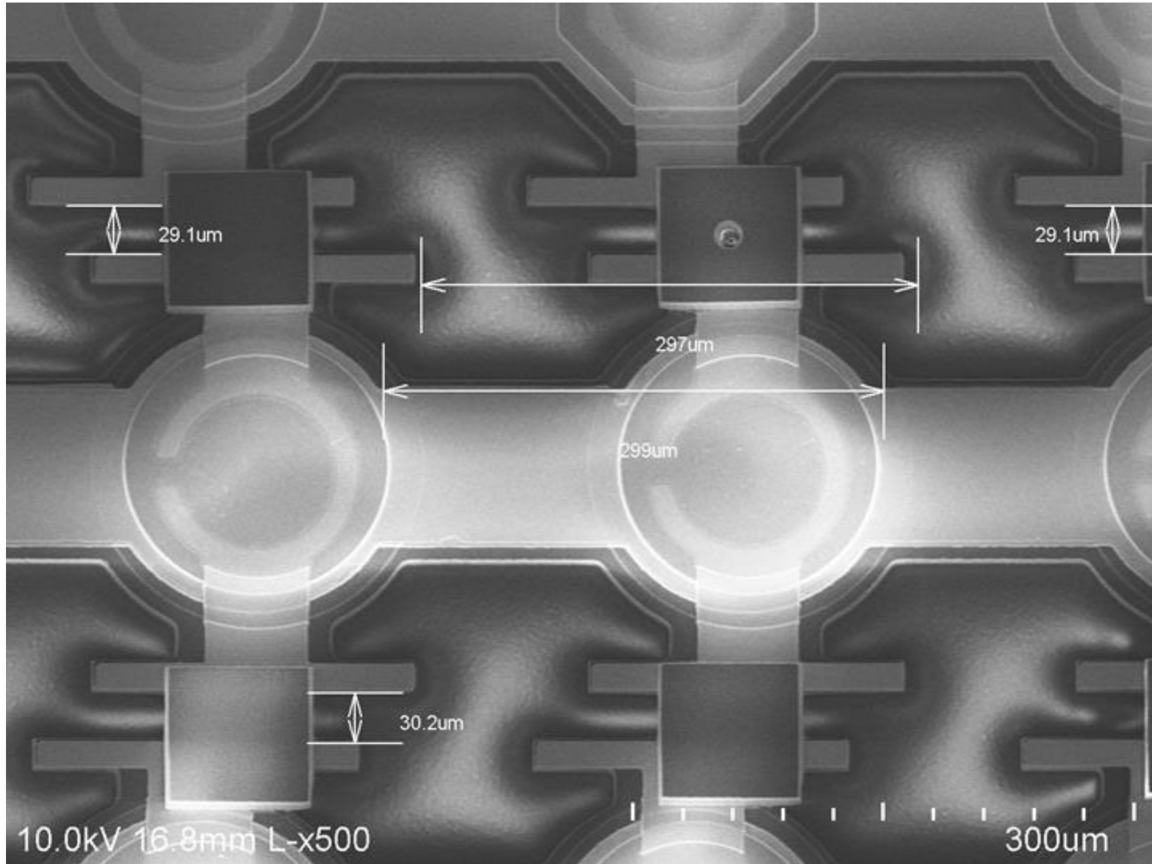

Figure 4.5: SEM image of individual pixels around the center of a fully fabricated (dummy) hemispherical focal plane array.

The designed distance between pixels is 300 µm. The measured distance between pixels in the horizontal direction in this figure (Y-direction in the inset of Figure 4.4 (a)) is approximately 300 µm. This result demonstrates that the photodiodes rows supported by Kapton substrate have no elongation in the horizontal direction during the stretching of PDMS membrane and transferring of the array. The designed gap between rows is 10 µm. The measured distance between pixels in the vertical direction in this figure (X-direction in in the inset of Figure 4.4 (a)) is approximately 30 µm. This result demonstrates that the photodiodes rows supported by Kapton® substrate have ~6.7% additional separation (30 µm = 10 µm gap + 300 µm pitch size × 6.7%) in the vertical direction during the stretching of PDMS membrane and transferring of the array. This result agrees with our simulated value (7%) in Figure 4.3 within measurement variation.

Shear-slip motion on PDMS has previously been observed and characterized in both organic[10] and inorganic[27] semiconductor systems. The governing factor that enables the slip is that the strain energy release rate must exceed the interface bonding energy between the surfaces. For

typical inorganic semiconductor/PDMS interfaces, the slip can occur for shear strains is > 7%[27]. In addition, due to the high Young's modulus of the 25 μm thick Kapton® film (~10^3 times higher than PDMS), the stress along the detector rows induced by PDMS stretching is well below the yield strength, and the strain in the thin film can thus be ignored. Generally, shear-slip motion and non-developable deformation is applicable to any circuit structure as long as the shear-induced energy release rate exceeds the interface binding between the circuit and the substrate transfer stamp, and the stress induced by PDMS stretching does not exceed the material yield strength of the circuit materials. It is worth mentioning that the relative positions of the top (light absorbing) surfaces of detectors on a row do suffer minor shrinkage due to the bending of the Kapton® film. More controllable geometries can be achieved by employing pre-distortion offsets of the pixel spacings during fabrication on the planar surface to achieve the target pixel spacings after transfer.

Next, the deformed array is brought into intimate contact with a hemispherical concave lens (Thorlabs, LC4942) coated with the same NOA 84 optical adhesive. The adhesive is fully cured (0.15 W/cm^2, 1 cm from the sample surface, 5 min), after which the lens and PDMS membrane are separated to complete the transfer (see Figure 4.4 and Figure 4.2 (b)). The residual adhesive is removed from the concave lens surface using O_2 plasma (O_2 = 80 sccm, 800 W ICP power, 300 mTorr pressure, 150°C stage temperature for 40 min).

The approach described in Figure 4.2 and Figure 4.4 transforms the two-dimensional tensile strain introduced during deformation to a simple separation and one-dimensional bending process. It maintains the pixel spacing before and after deformation in the Y-direction. In the X-direction, a second layer of detector rows can be applied in the same manner to fill in the gaps that arise during application of the first layer during stretching as shown by Figure 4.6.

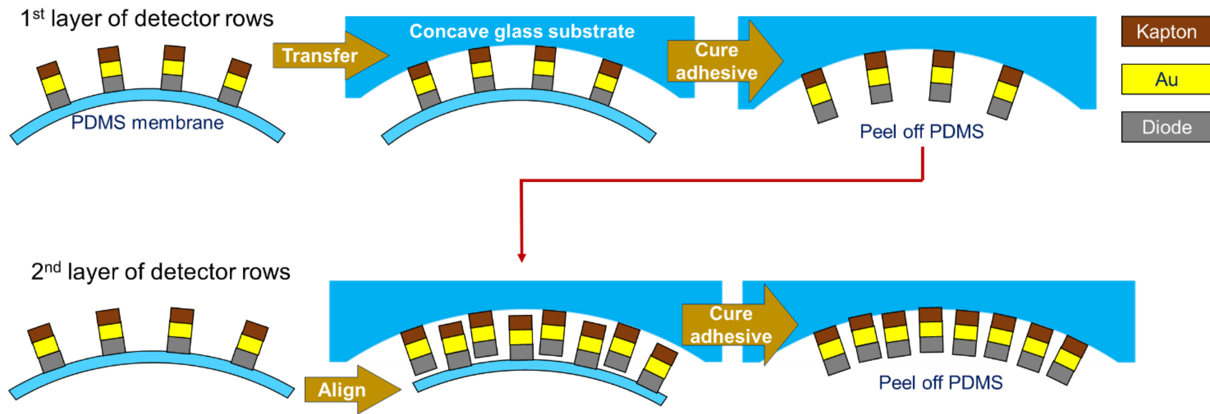

Figure 4.6: Schematic illustration of transferring a second layer of detector rows.
A second layer of detector rows can be applied in the same way as the first layer to fill the gaps that arise during application of the first layer during stretching. During the application, the second layer of detector rows is attached to the PDMS membrane and deformed by a PDMS punch. It is fixed on a 6-axis manual transfer stage that has X,Y, and Z axes translation and X,Y, and Z axes tilt. The top concave substrate with the first layer of detector rows transferred is fixed above the transfer stage. A stereo-microscope is used to observe from the top to align the concave substrate and the 2nd layer of detector rows. This step can be executed the same way as the application of metalized pads that connect rows of detectors. The result of such aligned transfer process on two hemispherical surfaces is demonstrated in both Figure 4.5 and Figure 4.7.

Finally, an array of metalized Kapton® pads is patterned and transferred to the concave substrate to connect rows of detectors and form the column connections (see Figure 4.7). The approach described here is compatible with batch fabrication of imagers (see Figure 4.8) with many high performance materials including, but not limited to Si, GaAs, InGaAs, and etc.

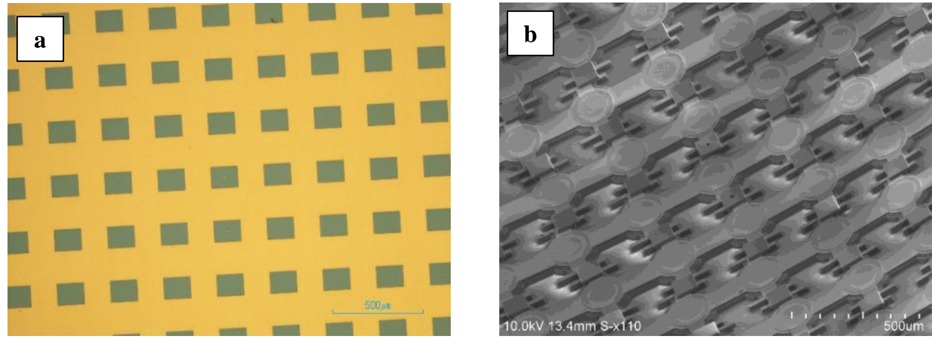

Figure 4.7: Metalized Kapton® pads for column connections.

(a) Microscopic image of photolithography mask of column connection pads. (b) SEM image of column connection pads transferred to the hemispherical concave substrate on top of the transferred rows of photodiodes. They are aligned between rows of photodiodes and enable column electrical connections.

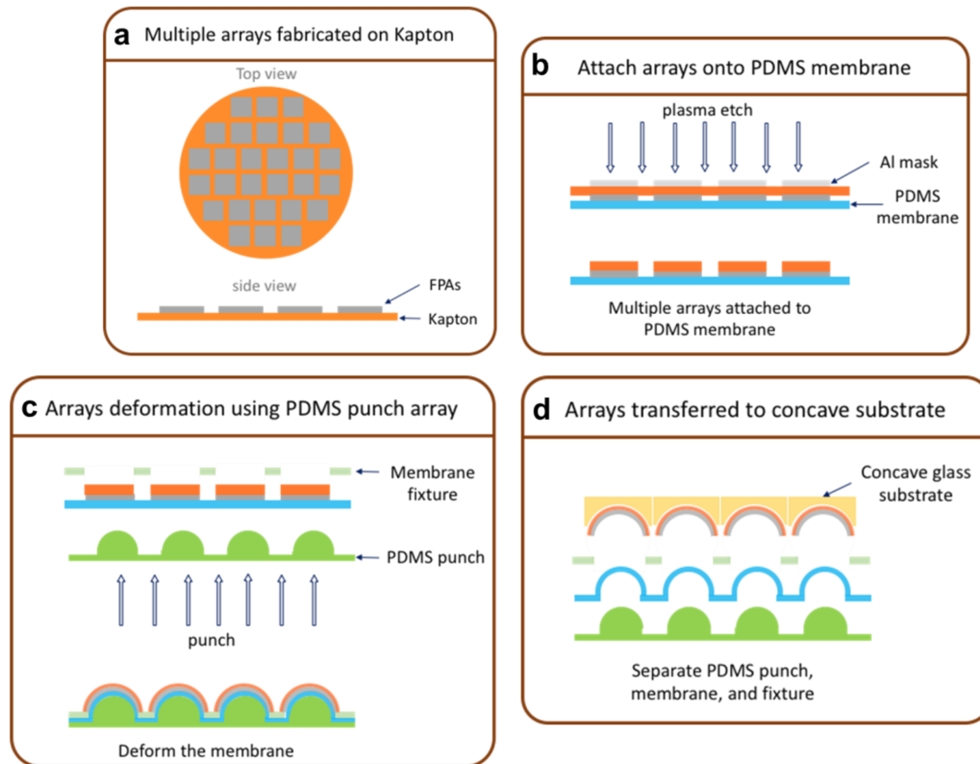

Figure 4.8: Schematics of the batch fabrication of multiple hemispherical focal plane arrays (FPAs).

(a) Multiple FPAs (gray) fabricated on Kapton® film (red). (b) Attach the Kapton® film onto PDMS membrane and etch Kapton® to separate FPAs using plasma. (c) Attach the membrane using a fixture with apertures centered to FPAs and deform the membrane with a PDMS punch array centered to FPAs. (d) Transfer multiple FPAs simultaneously to concave glass substrates, separate PDMS punch, membrane, and fixture. Batch fabrication of multiple hemispherical FPAs can be achieved.

4.3. Device characterization

Figure 4.9 (a) shows a GaAs *p-n* photodiode HFPA fabricated on a truncated concave hemispherical glass substrate with a radius of curvature = 9.2 mm, depth = 2.5 mm, and opening diameter = 12.7 mm. The 15×15 pixel array is centered within the substrate depression, providing high resolution foveal imaging capability. A secondary, 4×2 pixel array is located along the lip of the depression that is transferred at the same time as the central array. It provides peripheral, but low-resolution vision similar to that sensed by the human eye. Furthermore, its application demonstrates the ability to transfer devices at angles > 43° to provide a very large FOV[28].

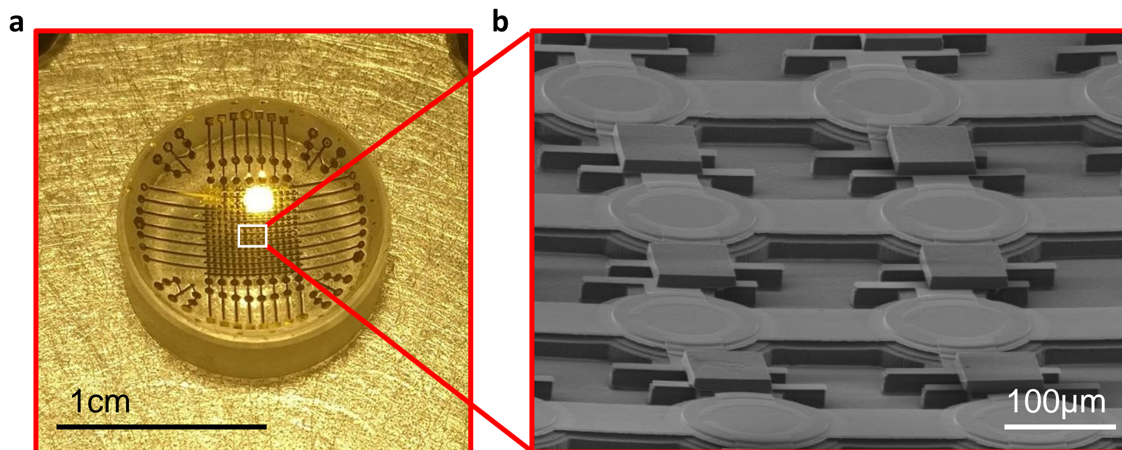

Figure 4.9: Images of a 15×15 pixel GaAs *p-n* junction FPA fabricated on a concave hemispherical surface.

(a) Photograph. Additional 4×2 peripheral pixels that allow for motion detection at wide angles of view are also

The scanning electron microscopic image in Figure 4.9 (b) provides a detailed view of the pixels shown in Figure 4.9 (a). No metal or semiconductor cracks are observed as typically encountered for free-standing metal films subjected to similarly substantial strain[10,29,30]. Metalized Kapton® pads between the pixels form top electrical connections that enable the column readout of the HFPA. Lateral misalignment between rows is due to the asymmetric shear slippage during

deformation and transfer. This issue can be solved by designing the array with a compensating offset between rows during fabrication prior to deformation.

Figure 4.10 is a schematic illustration of the photodiode pixel in the array. Each 150 μm diameter photodiode is connected in rows with adjacent pixels (300 μm center-to-center spacing) through the 50 μm wide bottom contact lines supported by the 60 μm wide Kapton® foil strips. Top contact rings are extended out of the photodetection area with 150 μm × 20 μm contact pads, and connected to adjacent units through a separately transferred layer of 80 μm × 60 μm column connection pads. An anti-reflection coating (ARC) is deposited on the top to enhance the optical absorption in visible spectrum.

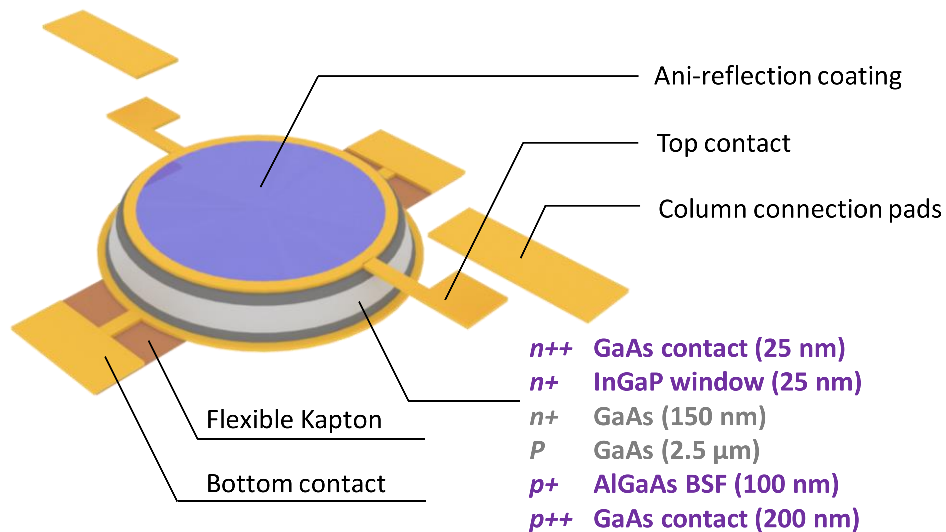

Figure 4.10: Schematic of a single pixel in the array.

The current-voltage (*I*-*V*) characteristics of a photodiode under dark and 64 nW illumination at a wavelength of $\lambda = 530$ nm are shown in Figure 4.11 inset. The *I*-*V* characteristics are measured using a Keithley 2400 Source Measuring Unit (SMU). The dark current is 1.3 ± 0.4

nA (corresponding to 7.4 ± 2.1 μA/cm^2) at -1 V for individual detector. The current under illumination is 18.5 nA at 0 V and 23.3 nA at -1 V.

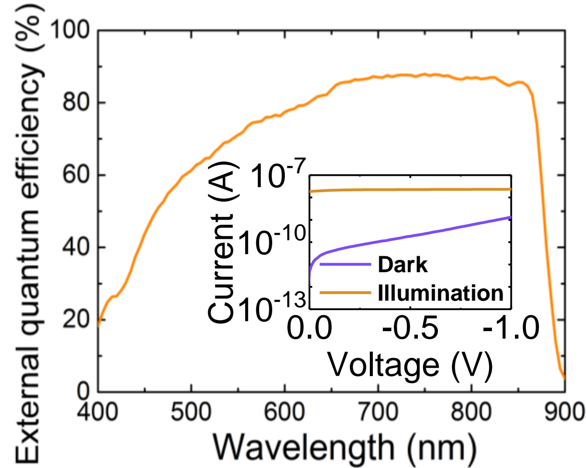

Figure 4.11: *EQE* and *I-V* characteristics.

External quantum efficiency (*EQE*) spectra of the photodiode in the wavelength range from 400 to 900 nm. Inset: Current-Voltage (*I-V*) characteristics of the photodiode in the dark (blue line) and under 64 nW, 530 nm light emitting diode (LED) illumination (orange line).

Figure 4.11 presents the external quantum efficiency, *EQE*, spectrum of a photodiode. *EQE* is measured using monochromatic illumination chopped at 200 Hz and coupled into a FG050LGA optical fiber oriented normal to the photodiode using a Lightwave Probe (Cascade Microtech, CA, 94551). The output signal is collected by a SR830 lock-in amplifier. The light illumination power is calibrated using a reference 818-UV/DB Si detector (Newport, CA, 92606). We observe *EQE* > 80% at $\lambda > 650$ nm, which to our knowledge is the highest reported for other hemispherical imagers[10–13,19]. The photodetector noise equivalent power is $NEP = \sqrt{2qI_D}/R(\lambda)$ under shot-noise-limited detection at -1 V, where q is the electron charge, I_D is the dark current, and $R(\lambda)$ is the responsivity at a given wavelength λ. With $EQE = 67.7\%$ at $\lambda = 530$ nm, then $R(\lambda) = 0.29\ A/W$, and $NEP = 7.03 \times 10^{-14}\ W/Hz^{1/2}$. The specific detectivity of the detector is $D^* =$

$\sqrt{A\Delta f}/NEP$, where A is its area, and Δf is the bandwidth, giving $D^* = 1.89 \times 10^{11}\ cm \cdot Hz^{1/2} \cdot W^{-1}$ in a 1 Hz bandwidth. The NEP and D^* are at the same order of magnitude as that of commercially available CCD imagers[23].

The normalized dark current map in Figure 4.12 (inset) and the histogram in Figure 4.12, indicate the yield of the 15×15 photodiode array is > 99% (223/225 photodiodes have a leakage current < 40 nA at -1 V. The dark current of the detectors on the array is 9.1 ± 7.9 nA at -1 V, which is approximately 7 times greater than for individual detectors due to sneak reverse currents from adjacent detectors. This can be eliminated by using a passive pixel sensor address transistor[31] at each pixel that can be transferred simultaneously with the detectors without change or complication to the existing process.

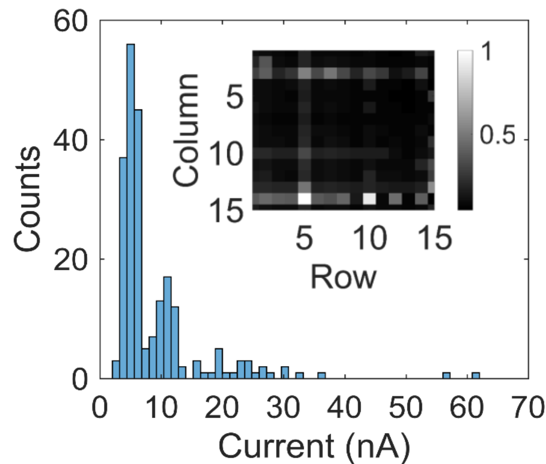

Figure 4.12: Dark current mapping.
Histogram of dark current of photodiodes on the 15×15 FPA. Inset: Normalized dark current maps of the 15×15 GaAs focal plane array (FPA) on hemispherical surface.

As shown in Figure 4.13, the detector dynamic range is determined from the detector photocurrent (black square) at $\lambda = 850$ nm vs. incident optical power. A photocurrent compression of 1 dB from linear response (red line) sets the maximum intensity, P_1, whereas P_0 is the lowest

detectable optical power (root-mean-square noise power). The dynamic range is $DR = 10\log(P_1/P_0)$. At 0 V, $P_0 = 10^{-4}$ W/cm^2, $P_1 = 10^{-1}$ W/cm^2, giving DR = 30 dB, corresponding to a 10-bit gray-scale resolution.

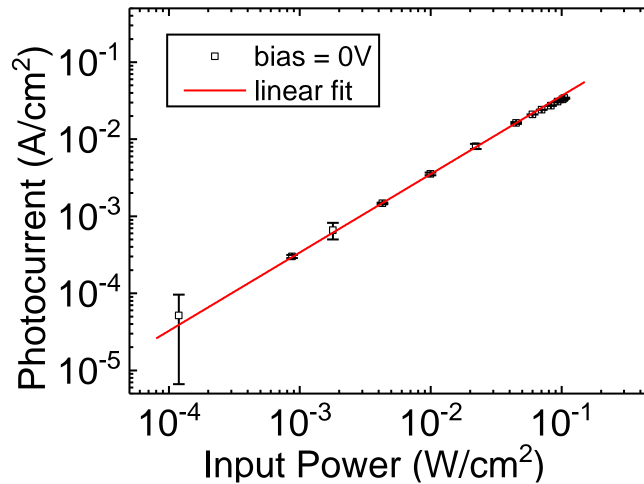

Figure 4.13: Photocurrent vs. input optical power of a single photodetector.
Red line shows a linear fit to the photocurrent at low input optical power. The minimum detectable power is about 10^{-4} W/cm^2, and the 1 dB compression point is at 0.1 W/cm^2, giving a 30 dB dynamic range and a 10-bit gray-scale resolution.

4.4. Imaging with HFPA

A conventional imaging system based on a planar FPA has a mismatch with the image plane of a single element lens. Producing a high resolution image thus necessitates additional optical elements that increase the complexity, weight and cost of the system, while restricting the FOV. Using an HFPA, however, provides the possibility of using a single plano-convex lens, whose optical field curvature is matched with that of the curvature of the FPA to produce high quality images[2,3,5].

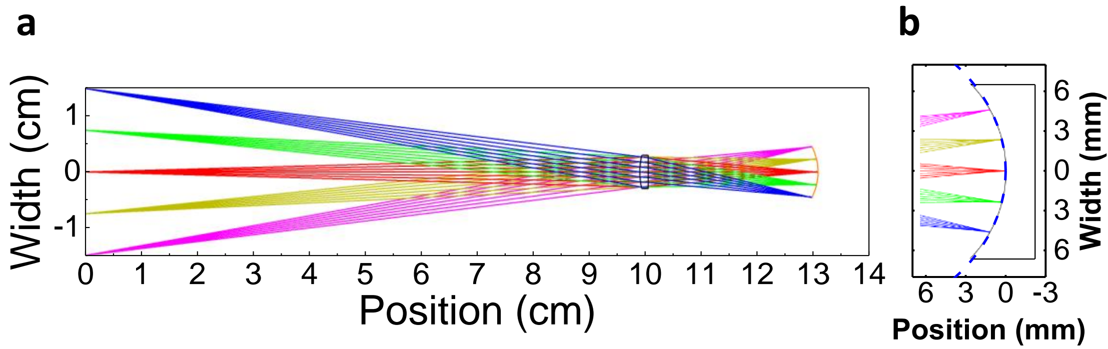

Figure 4.14: Ray tracing simulation.

(a) Ray tracing simulation result of an object (3 cm wide) located 10 cm from a plano-convex lens (black contour). Rays from the object are focused by the lens onto the FPA surface (orange curve, 3.0 cm from the lens). (b) Magnified view around the hemispherical imager (black contour). The simulated lens focal surface (blue dashed line) has good overlap with the concave FPA surface (front curve of the black contour).

As shown in Figure 4.14 (a), multiple rays illuminated from five point-sources (3 cm wide) positioned at the origin can be focused onto the curved plane of the HFPA centered at 3.0 cm from the lens at a distance of 10 cm. This image plane has a radius of curvature of R = 9.2 mm in the center, and gradually increases to 10.1 mm towards the edge as shown by the blue dashed line in Figure 4.14 (b). An HFPA (black contour in Figure 4.14 (b)) with R = 9.2 mm is positioned coaxially with the lens. The simulated results in Figure 4.15 show a spot size of 13.4 μm and 38.3 μm for the images of point sources in the center and on the edge, respectively, corresponding to a 1.8 times edge defocusing. In comparison, when a planar FPA is located at the same position as the HFPA, the simulated spot sizes are 13.4 μm and 73.9 μm, corresponding to a 4.5 times edge defocusing.

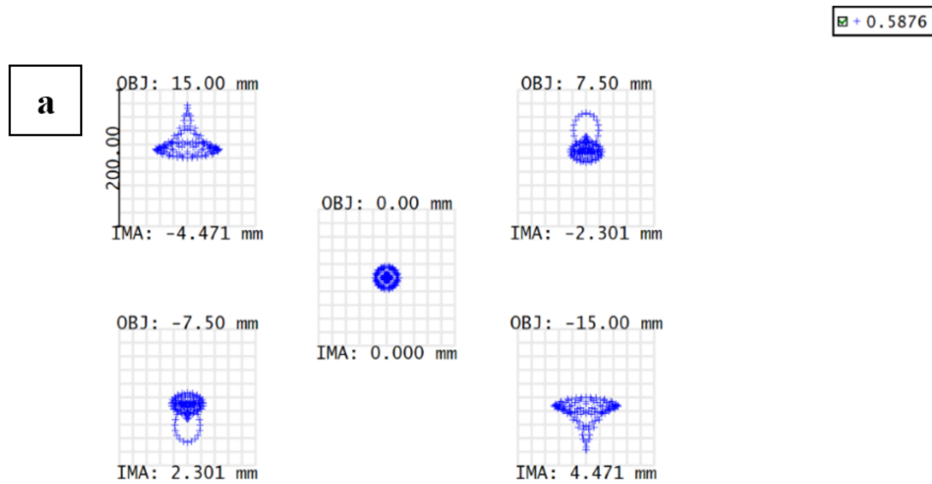

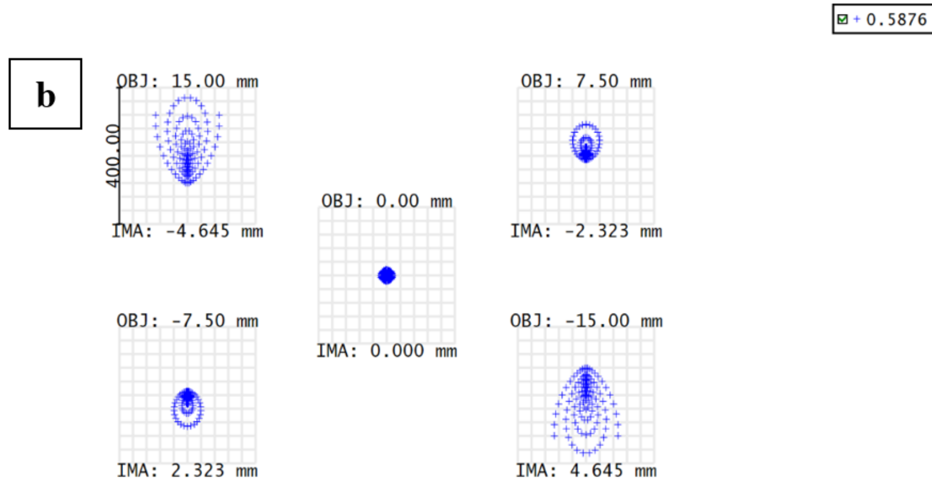

Figure 4.15: Ray tracing simulation spot diagram of a curved image surface using ZeMax. (a) Each group of spots correspond to the focusing rays on the curved image surface shown in Figure 4.14 (b). Center ray has a spot radius of 13.4 µm, while the ray on the edge has a spot radius of 38.3 µm, showing 1.8 times edge defocusing. (b) Spot diagram of the same light sources focused on a planar image surface. Center ray has a spot radius of 13.4 µm, while the ray on the edge has a spot radius of 73.9 µm, showing 4.5 times edge defocusing.

A single-lens imaging system using the fabricated HFPA is shown in Figure 4.16. Object imaging is measured using a 48-channel probe card (AccuProbe, MA, 01970) interfaced with a Keithley 2400 SMU and a Keithley 2700 + Keithley 7705 switching unit. A customized LabView graphic user interface is programmed to collect output signals. A schematic of the signal collection mechanism is shown in Figure 4.16 and Figure 4.17. The HFPA was mounted on a 3D printed substrate holder. Row and column electrical contacts are extended to the edge of the substrate holder and connected to a 48-channel probe card that is interfaced to the read-out electronics. The plano-convex lens (diameter = 6 mm, focal length = 24 mm) is mounted on a 3D printed lens holder and plugged into the substrate holder. The resulting system is mounted on a six-axis optical stage to capture images as shown in Figure 4.16 (b).

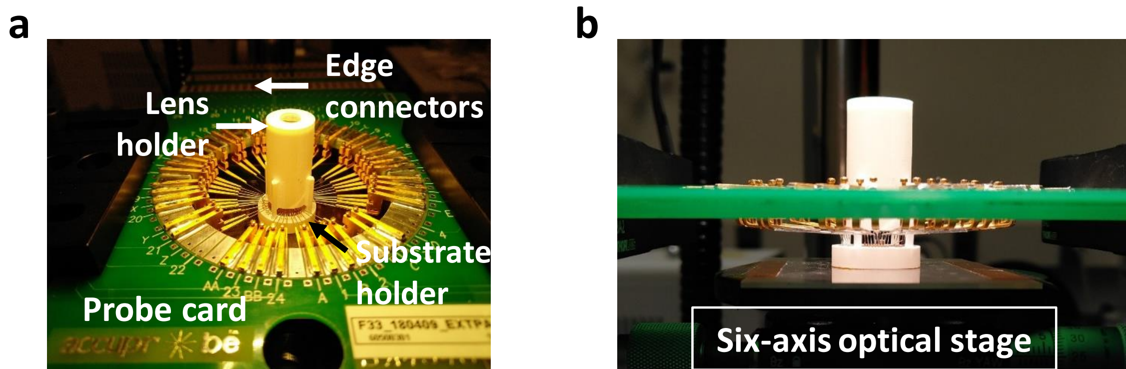

Figure 4.16: Photograph of the HFPA mounted on testing stage.

(a) HFPA mounted on a 3D printed substrate holder integrated with a 3D printed lens holder. Also presented is a 48-channel probe card used to read currents generated by all pixels on the hemispherical FPA simultaneously. (b) Side view of the experimental setup for imaging acquisition.

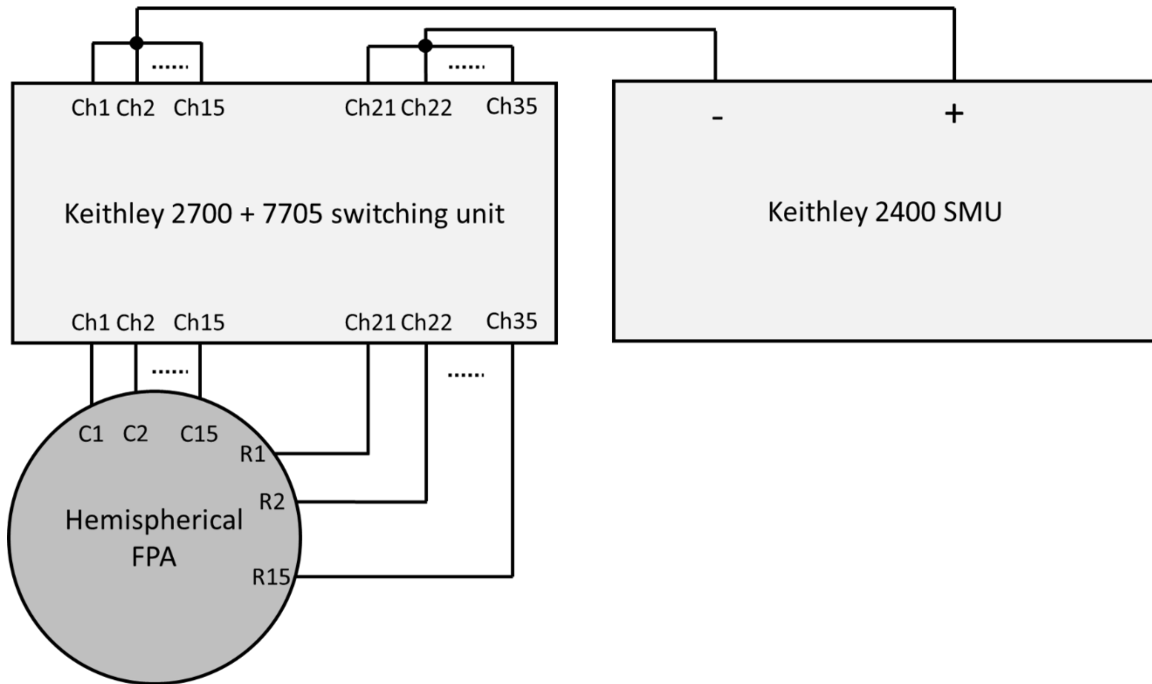

Figure 4.17: Schematics of the image acquisition mechanism.

15 rows and 15 columns of the hemispherical FPA are electrically contacted simultaneously using a probe card. Assign columns to the input channels 1 to 15 on a switching unit, and assign rows to the input channels 21 to 35. The output channels 1 to 15 are wired together and connected to the driving voltage port of an SMU. The output channels 21 to 35 are wired and connected to the SMU ground. The current generated by a specific pixel, for example row 1 and column 1, can be addressed by switching on channels 1 and 21 while leaving all other channels off, and running SMU to collect signal.

The diffuse emission from a $\lambda = 525$ nm LED illuminates an image formed by a glass slide patterned with 1 cm wide "O", "C", and "M" apertures. Applying a leakage (sneak) current threshold of 15.8 nA, the images of these letters are acquired as shown in Figure 4.18. The lens provides the HFPA with a calculated array angular coverage of ~15°, and a field of view of approximately 112°. This is demonstrated by focusing the LED source (3 mm diameter) to ~60° from the optical axis of the lens. The edge detectors on the HFPA generate a photocurrent two orders of magnitude larger than in the absence of the light source with a power of 23.2 nW. This demonstrates the object detection ability of the HFPA at a large viewing angle.

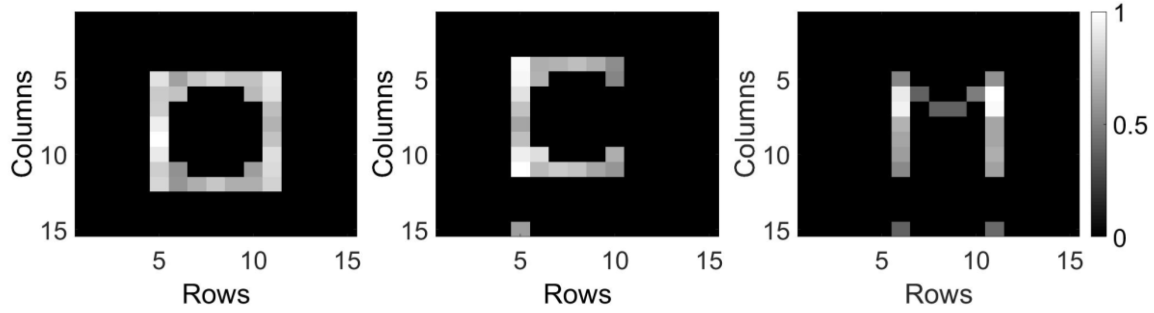

Figure 4.18: Normalized photocurrent map.

Normalized photocurrent map on the 15×15 FPA showing images of letter "O", "C", and "M". A leakage current threshold of 15.8 nA is applied to minimize obscuration of the images by the background sneak currents.

4.5. Conclusion

We demonstrate a general strategy to achieve topological transformations of optoelectronic devices from a 2D plane into a 3D surface by exploiting slippage of the circuits during deformation. We use this process to demonstrate retina-like hemispherical imagers by starting on a planar substrate, and then transferring the array onto a hemispherical surface without loss of array resolution. This process results in defect-free metal interconnections and a fixed pixel spacing. The HFPA has an individual detector performance comparable to that found in conventional planar CCD imagers. The hemispherical shape enables simplified optical designs with reduced aberrations along with a large FOV. The resolution of the imaging system is currently limited to tens of microns by the need to manually align the lens with only a 10 μm alignment tolerance. A smaller pixel spacing of < 5 μm is achievable by use of more precise optics. The array size is limited to 15 x 15 to minimize sneak currents. Arrays with pixel density and counts similar to those in commercial CMOS imagers are possible if the detectors are integrated with access transistors in each cell. Including more circuit elements does not change the process sequence, since our

process uses conventional planar semiconductor fabrication methods up until the transfer to the shaped surface occurs. The combination features and fabrication strategies demonstrated in this work introduce processing techniques and performance advantages that may lead to new capabilities of next generation conformable and foldable optoelectronic devices.

CHAPTER 4

Bibliography

1. Hecht, J. The Eye and How It Works. in *Optics* 33–44 (Addison-Wesley, 1987).

2. Rim, S.-B., Catrysse, P. B., Dinyari, R., Huang, K. & Peumans, P. The optical advantages of curved focal plane arrays. *Opt. Express* **16**, 4965 (2008).

3. Dinyari, R., Rim, S.-B., Huang, K., Catrysse, P. B. & Peumans, P. Curving monolithic silicon for nonplanar focal plane array applications. *Appl. Phys. Lett.* **92**, (2008).

4. Brady, D. J. *et al.* Multiscale gigapixel photography. *Nature* **486**, 386–389 (2012).

5. Lee, G. J., Nam, W. Il & Song, Y. M. Robustness of an artificially tailored fisheye imaging system with a curvilinear image surface. *Opt. Laser Technol.* **96**, 50–57 (2017).

6. Shen, G. & Fan, Z. *Flexible Electronics*. (World Scientific Publishing Co, 2016).

7. Fan, D., Lee, K. & Forrest, S. R. Flexible Thin-Film InGaAs Photodiode Focal Plane Array. *ACS Photonics* **3**, (2016).

8. Iwert, O. & Delabre, B. The challenge of highly curved monolithic imaging detectors. *Proc. SPIE* vol. 7742 774227–774229 (2010).

9. Guenter, B. *et al.* Highly curved image sensors: a practical approach for improved optical performance. *Opt. Express* **25**, 13010 (2017).

10. Xu, X., Davanco, M., Qi, X. & Forrest, S. R. Direct transfer patterning on three dimensionally deformed surfaces at micrometer resolutions and its application to hemispherical focal plane detector arrays. *Org. Electron.* **9**, 1122–1127 (2008).

11. Ko, H. C. *et al.* A hemispherical electronic eye camera based on compressible silicon optoelectronics. *Nature* **454**, 748–753 (2008).

12. Zhang, K. *et al.* Origami silicon optoelectronics for hemispherical electronic eye systems. *Nat. Commun.* **8**, 1782 (2017).

13. Wu, T. *et al.* Design and fabrication of silicon-tessellated structures for monocentric

imagers. *Microsystems Nanoeng.* **2**, 16019 (2016).

14. Yoon, J. *et al.* Heterogeneously Integrated Optoelectronic Devices Enabled by Micro-Transfer Printing. *Adv. Opt. Mater.* **3**, 1313–1335 (2015).

15. Wong, W. & Salleo, A. *Flexible electronics: materials and applications*. (Springer US, 2009).

16. Park, S. Il *et al.* Soft, stretchable, fully implantable miniaturized optoelectronic systems for wireless optogenetics. *Nat. Biotechnol.* **33**, 1280–1286 (2015).

17. Swain, P. K., Channin, D. J., Taylor, G. C., Lipp, S. A. & Mark, D. S. Curved CCDs and their application with astronomical telescopes and stereo panoramic cameras. *Proc. SPIE* vol. 5301 109–129 (2004).

18. Song, Y. M. *et al.* Digital cameras with designs inspired by the arthropod eye. *Nature* **497**, 95–99 (2013).

19. Choi, C. *et al.* Human eye-inspired soft optoelectronic device using high-density MoS2-graphene curved image sensor array. *Nat. Commun.* **8**, 1664 (2017).

20. Kim, C., Burrows, P. E. & Forrest, S. R. Micropatterning of Organic Electronic Devices by Cold-Welding. *Sci.* **288**, 831–833 (2000).

21. Konagai, M., Sugimoto, M. & Takahashi, K. High efficiency GaAs thin film solar cells by peeled film technology. *J. Cryst. Growth* **45**, 277–280 (1978).

22. Lee, K., Zimmerman, J. D., Hughes, T. W. & Forrest, S. R. Non-Destructive Wafer Recycling for Low-Cost Thin-Film Flexible Optoelectronics. *Adv. Funct. Mater.* **24**, 4284–4291 (2014).

23. Rogalski, A. Progress in focal plane array technologies. *Prog. Quantum Electron.* **36**, 342–473 (2012).

24. Huang, Y. Y. *et al.* Stamp collapse in soft lithography. *Langmuir* **21**, 8058–8068 (2005).

25. Meitl, M. A. *et al.* Transfer printing by kinetic control of adhesion to an elastomeric stamp. *Nat. Mater.* **5**, 33–38 (2006).

26. Ventsel, E. & Krauthammer, T. Geometry of the Middle Surface. in *Thin Plates and Shells* 303–324 (2001).

27. Carlson, A. *et al.* Shear-enhanced adhesiveless transfer printing for use in deterministic materials assembly. *Appl. Phys. Lett.* **98**, 264104 (2011).

28. Atchison, D. A. & Smith, G. *Optics of the human eye*. (Butterworth-Heinemann, 2000).

29. Lacour, S. P., Jones, J., Wagner, S., Teng Li & Zhigang Suo. Stretchable Interconnects for Elastic Electronic Surfaces. *Proc. IEEE* **93**, 1459–1467 (2005).

30. Lacour, S. P., Wagner, S., Huang, Z. & Suo, Z. Stretchable gold conductors on elastomeric substrates. *Appl. Phys. Lett.* **82**, 2404–2406 (2003).

31. Fossum, E. R. CMOS image sensors: electronic camera-on-a-chip. *IEEE Trans. Electron Devices* **44**, 1689–1698 (1997).

Chapter 5

Thin-Film Architectures with High Spectral Selectivity for Thermophotovoltaic Cells

Thermophotovoltaic (TPV) systems are a promising technology for distributed conversion of high-temperature heat to electricity. To achieve high conversion efficiency, the transport of sub-bandgap radiation between the thermal emitter and PV cell should be suppressed. This can be achieved by recycling sub-bandgap radiation back to the emitter using a spectrally selective cell. However, conventional TPV cells exhibit limited sub-bandgap reflectance. In this chapter, we demonstrate thin-film $In_{0.53}Ga_{0.47}As$ structures with high spectral selectivity, including record-high average sub-bandgap reflectance (96%). Selectivity is enabled by short optical paths through a high-quality material fabricated using epitaxial lift-off, highly reflective back surfaces, and optimized interference. In addition, we use a parallel-plate TPV model to evaluate the impact of specific structural features on performance and to optimize the cell architecture. We show that a dielectric spacer between the InGaAs and the Au back contact is an important feature that enables a predicted TPV efficiency above 50% (with a power output of 2.1 W/cm^2), significantly higher than current TPV devices. This work provides guidelines for the design of high-efficiency, low-cost TPV generators.

5.1. Introduction

Thermophotovoltaic (TPV) systems are a promising alternative to turbines for small-scale energy conversion (~1 kW) such as distributed co-generation of heat and power[1–4]. The technology also has the potential for integration with high-temperature thermal energy storage, a technique that could help regulate power supply[5–8]. A thermophotovoltaic cell generates electricity by converting photons radiated by a hot thermal emitter (Figure 5.1)[1]. Selective radiative transfer, specifically suppression of sub-bandgap radiative transfer, is essential for high efficiency[3,6,9–14]. However, conventional TPV cells, in which the growth substrate is used in the device, have limited spectral selectivity[10–12,15]. Here, we investigate thin-film TPV cells fabricated using epitaxial lift-off to enable selective radiative transfer and high efficiency. A significant enhancement in spectral selectivity, relative to conventional TPVs, was measured in thin-film $In_{0.53}Ga_{0.47}As$ (hereafter InGaAs) structures because of the reduced optical path and optimized interference. Beyond their optical advantages over conventional TPVs, thin-film devices fabricated using epitaxial lift-off have the potential to increase the external luminescent efficiency[14] and to reduce the cost of TPV generators by reusing expensive III-V substrates[1,3,12,16–18].

TPV cells exhibiting selective absorption have facilitated recycling of low-energy photons, and consequently, improved efficiency[9–11,15]. This approach makes use of a cell with a back surface reflector (BSR) or a front surface filter (FSF) to reflect radiation with energy lower than the semiconductor bandgap while absorbing radiation with higher energies[9–11,15]. Low-energy photons reflected by the cell are re-absorbed by the thermal emitter, decreasing net heat transfer between the emitter and cell (Q_h) without decreasing output power (P_{out}) (Figure 5.1). An early demonstration of selective absorption in a Si cell with a Ag BSR reached a thermal-to-electrical conversion efficiency of 26% for an emitter temperature of 2300 K[15]. Utilization of lower bandgap

cells has enabled similar efficiencies at moderate temperatures. Siergiej, *et al*. utilized a 0.6 eV InGaAs cell with a Si_3N_4/Au BSR to achieve an efficiency of 20.6% for a 1330 K emitter[10]. Deposition of a dielectric spacer layer on the BSR helps to mitigate sub-bandgap absorption by limiting the intensity of radiation at the absorbing metallic surface[19–21]. This device was later modified to include a FSF, increasing its efficiency to 23.6%[11]. The measured spectral selectivity of these approaches, however, has been limited by absorption of sub-bandgap radiation due to a variety of possible mechanisms including parasitic absorption in the growth substrate[10–12,15].

The structures we demonstrated in this chapter exhibit higher reflectance below the semiconductor bandgap than previous TPVs, coupled with high absorption of radiation above the bandgap. To evaluate the impact of specific thin-film structural features on performance and to optimize the cell architecture, we use a prediction of TPV performance in a parallel-plate geometry. This work provides design guidelines for selectively absorptive, high-efficiency thin-film TPVs.

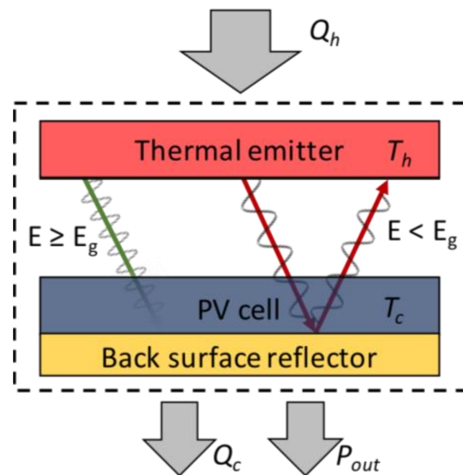

Figure 5.1: Energy flows in a parallel plate TPV system with sub-bandgap photon recycle. Spectrally selective absorption is achieved in a thin-film cell, decreasing waste heat (Q_c) and net heat transfer between the emitter and cell (Q_h), without decreasing output power (P_{out}).

5.2. Device Fabrication

As a baseline structure, we fabricated and characterized the optical properties of a 1.38 μm thick epitaxial layer of InGaAs on a Au BSR, hereafter called *BSR* (Figure 5.2 (a)). InGaAs structures were grown by gas-source molecular beam epitaxy. A 200 nm thick, unintentionally doped InP buffer layer was grown on a 2 inch diameter, Zn doped (100) InP wafer, followed by a 4 nm thick AlAs sacrificial layer, and an unintentionally doped *i*-InGaAs absorption layer. The wafer was then diced into 6 mm x 6 mm squares using an ADT7100 dicing saw. Samples were rinsed with DI water for 30 seconds to remove dicing residue and stored in acetone to prevent surface contamination. Immediately before further processing, samples were soaked in buffered HF for 1 minute and rinsed in DI water for 10 seconds to remove surface native oxides. Following InGaAs film growth, a 200 nm thick Au layer was deposited by electron beam evaporation on the epitaxial InGaAs surface. A 500 μm thick Si wafer was immersed in buffered HF for 1 minute and rinsed in DI water for 10 seconds to remove native oxides. A 5 nm thick Ir adhesion layer and a 200 nm thick Au layer were deposited on the Si wafer. The metalized surfaces of the sample and wafer were cold-weld bonded by applying heat (200°C) and pressure (5 MPa) for 5 minutes under vacuum (10^{-4} mTorr) using an EVG 520 wafer bonder. The epitaxial layers were lifted off from the parent InP wafer by removing the AlAs layer through immersion in 17% HF at 45°C with 400 rpm agitation by magnetic stir bar for 1.5 hours. Following lift-off, samples were stored at 60°C in Remover PG (MicroChem) to prevent oxide formation on the epitaxial surface prior to further processing.

To enhance the above-bandgap absorption of the structure, we deposited a double layer anti-reflection coating (ARC) (190 nm MgF_2, 110 nm ZnSe) on a 1.3 μm InGaAs layer with a Au *BSR*, hereafter called *ARC* (Figure 5.2 (b)).

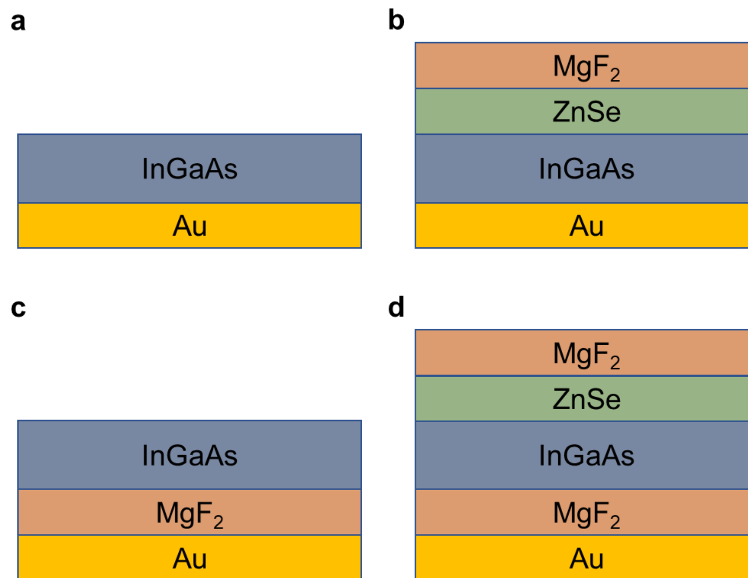

Figure 5.2: Schematics of the thin-film structures.

(a) Structure of back surface reflector (*BSR*), (b) anti-reflection coating (*ARC*), (c) InGaAs on dielectric spacer (*Spacer*), and (d) *ARC* and *Spacer*.

As a strategy for enhancing sub-bandgap reflectance, we fabricated a different structure, consisting of a 430 nm thick MgF_2 spacer between a 2.1 μm thick InGaAs layer and Au *BSR*. The InGaAs-MgF_2-Au structure, hereafter called *Spacer* (Figure 5.2 (c)). The Spacer structure was fabricated as follows. Following InGaAs film growth, a 200 nm thick Au layer was deposited by electron beam evaporation on the epitaxial InGaAs surface. Similarly, a 5 nm thick Ir adhesion layer and a 200 nm thick Au layer were deposited on a 25 μm thick E-type Kapton foil substrate. The metalized surfaces of the sample and foil were cold-weld bonded by applying heat (200°C) and pressure (5 MPa) for 5 minutes under vacuum (10^{-4} mTorr) using an EVG 520 wafer bonder. The epitaxial layers were lifted off from the parent InP wafer by removing the AlAs layer through immersion in 17% HF at 45°C with 400 rpm agitation by magnetic stir bar for 1.5 hours.

Following lift-off by HF etch, MgF_2 was deposited onto the epitaxial InGaAs surface by electron beam evaporation, followed by a 200 nm thick Au layer. A 500 μm thick (100) B doped Si wafer was immersed in buffered HF for 1 minute and rinsed in DI water for 10 seconds to remove native oxides. A 5 nm thick Ir adhesion layer and a 200 nm thick Au layer were deposited on the Si wafer. The metalized surfaces of the sample and Si wafer were cold-weld bonded by applying heat (200°C) and pressure (5 MPa) for 5 minutes under vacuum (10^{-4} mTorr) using an EVG 520 wafer bonder. The Kapton® host foil was removed by inductively coupled plasma (ICP) reactive-ion etching (RIE) (Oxford Plasmalab System 100) with 20 sccm of O_2 at a chamber pressure of 6 mTorr, stage temperature of 0°C, ICP power of 500 W, and forward power of 100 W for 25 minutes. The remaining Ir and Au layers were removed using ICP RIE with 12:9:5 sccm of H_2:Cl_2:Ar at a chamber pressure of 10 mTorr, stage temperature of 0°C, ICP power of 500 W, and forward power of 100 W for 2.5 minutes.

5.3. Optical Properties

In this section, we identify techniques for enhancing the spectral selectivity of fabricated thin films. We also compare the measured reflectance to optical modeling based on the transfer matrix method[22,23]. The absorptance (a) of the *BSR* structure, as a function of incident photon energy (E) and incidence angle (θ), is compared to the experimental response measured by a Fourier transform infrared (FT-IR) microscope (Figure 5.3 (a)). The response is characterized by selective absorptance above the material bandgap. Average, weighted optical properties were calculated with respect to the photon flux of a 1500 K emitter. The measured response exhibits an

average absorptance of 61% above the bandgap and 5.5% below the bandgap (94.5% average sub-bandgap reflectance).

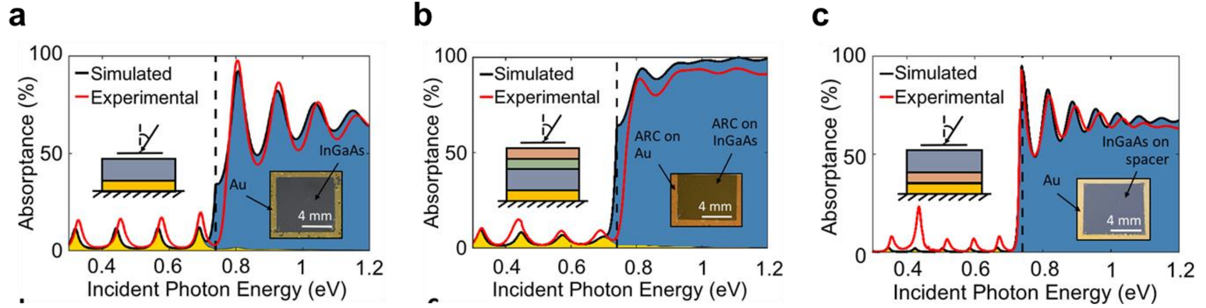

Figure 5.3: Simulated and measured absorption spectra.

Simulated (red) and measured (black) optical responses of the (a) *BSR* structure, (b) *ARC* structure, (c) *Spacer* structure. Blue (yellow) shading indicates predicted absorption by the InGaAs (Au) layer. Left inset: Angle of incidence (15°). Right inset: Photograph of structure.

The optical response of the *ARC* structure is characterized by a pronounced increase in absorptance above the bandgap compared to the *BSR* structure and a reduction of peak-to-peak absorptance variations (Figure 5.3 (b)). On average, the *ARC* structure exhibits absorptance of 81% above the bandgap and 5.3% absorptance below the bandgap (94.7% average sub-bandgap reflectance). A parasitic absorptance peak is observed at 0.44 eV, which is attributed to absorption in the double-layer ARC, as confirmed by measurement of the ARC directly on Au (see Figure 5.4).

The *Spacer* structure exhibits an average sub-bandgap reflectance of 95.7% (Figure 5.3 (c)), better than either of the previous structures. A parasitic absorptance peak at 0.44 eV, similar to the one observed in the *ARC* structure, limits the desired reflectance. The *Spacer* structure exhibits above-bandgap absorptance of 62.5%, comparable to that of *BSR* structure. Outside of the parasitic peak, the simulated optical response of each of the architectures agrees with its measured

response within 9% above the bandgap and 5% below the bandgap. The model also captures the oscillatory interference variations in absorptance. Material optical properties obtained from literature were used in the simulations[24–30]. All experimental layer thicknesses are estimated from their growth rate during fabrication.

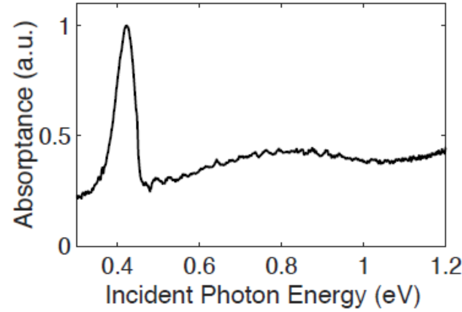

Figure 5.4: Measured optical response of MgF_2/ZnSe ARC on Au.

5.4. Energy Conversion Simulation

During TPV operation (Figure 5.1), input heat (Q_h) increases the temperature of the emitter (T_h) and drives thermal emission (Q_{emit}). The photon flux of an emitting blackbody, Φ, as a function of emitted photon energy, E, is calculated via Planck's Law:

$$\Phi(E) = \frac{2\pi E^2}{c^2 h^3 \left(\exp\left(\frac{E}{k_B T}\right) - 1\right)} \tag{5.1}$$

where c is the speed of light, h is Planck's constant, and k_B is the Boltzmann constant. Radiation emitted by the thermal emitter, $\Phi_h(E)$, is described by Planck's Law evaluated at T_h.

A portion of incident radiation is absorbed by the PV cell and the rest is reflected (Q_{ref}). Hemispherical-averaged absorptance (*a(E)*) is calculated by integration of the angle-dependent absorption spectrum (*a(E, θ)*) over angles (*θ,ϕ*):

$$a(E) = \frac{\int_0^{2\pi}\int_0^{\pi/2} a(E,\theta)\cos(\theta)\sin(\theta)d\theta d\phi}{\int_0^{2\pi}\int_0^{\pi/2}\cos(\theta)\sin(\theta)d\theta d\phi} \tag{5.2}$$

Upon absorption in the InGaAs layer, above-bandgap photons generate excited electron-hole pairs, enabling the generation of electrical power (P_{out}).

The maximum short circuit current, is calculated from the angle-averaged optical response, *a(E)*, and the emitted photon flux, $\Phi_h(E)$:

$$J_{SC} = q\int_{E_g}^{\infty} a(E)\Phi_h(E)dE \tag{5.3}$$

where q is the elementary charge of an electron and E_g is the bandgap.

The photocurrent, J, as a function of voltage across the cell, V, is the difference between the short circuit current and recombination loss, given by:

$$J(V) = J_{sc} - q\left(R_{rad} + R_{SRH} + R_{Aug}\right) \tag{5.4}$$

where $R_{rad,}$ R_{SRH}, and R_{Aug}, are the radiative, Shockley-Reed-Hall (SRH), and Auger recombination rates, respectively. The radiative recombination rate is:

$$R_{rad} = exp\left(\frac{qV}{k_B T_c}\right)\int_{E_g}^{\infty} a(E)\Phi_c(E)dE \tag{5.5}$$

In the case of low semiconductor doping concentration (N_D), such that the injected carrier concentration (n_o) is greater than N_D, the non-radiative recombination rates are independent of dopant concentration.[31] In this high-injection regime, the non-radiative SRH recombination rate is:

$$R_{SRH} = \frac{Ln_i^2}{\tau_{SRH}} exp\left(\frac{qV}{2k_BT_c}\right) \quad (5.6)$$

where L is the thickness of the active region, τ_{SRH} is the SRH recombination lifetime, and n_i is the intrinsic carrier concentration. Literature values of intrinsic carrier concentration and SRH lifetime for InGaAs at 300 K are 6.3×10^{11} cm^{-3} and 47.4 μs, respectively[32]. The non-radiative, Auger recombination rate, R_{Aug}, is:

$$R_{Aug} = L\left(C_n + C_p\right) n_i^3 exp\left(\frac{3qV}{2k_BT_c}\right) \quad (5.7)$$

where C_n and C_p are the Auger recombination coefficients for recombination involving two electrons and two holes, respectively. The Auger recombination coefficients are $C_n = C_p = 8.1\times10^{-29}$ cm^{-3} [32].

The output power of the cell is the product of the photocurrent and the voltage:

$$P_{out} = J(V) \cdot V \quad (5.8)$$

Efficiency is calculated from the maximum power point voltage, V_{MPP}, and current response, J_{MPP} via:

$$\eta_{TPV} = \frac{P_{out}}{Q_h} = \frac{P_{out}}{Q_{emit}-Q_{ref}} = \frac{J_{MPP}\cdot V_{MPP}}{\int_0^\infty E\cdot\Phi_h(E)dE - \int_0^\infty\left(1-a(E)\right)\cdot E\cdot\Phi_h(E)dE} \quad (5.9)$$

5.5. Evaluating Strategies for Enhanced Selectivity

To evaluate the spectral selectivity of the three cases (*BSR*, *ARC*, and *Spacer*), we use a prediction of TPV performance (see section 5.4) based on the optical response and geometry of the cell, operating at 20°C, in perfect view of a high-temperature black emitter. For a fair

comparison among cases, we varied the layer thicknesses within the constraints of the three cases to maximize the predicted conversion efficiency. The performance of the optimized structures (Table 5.1) is compared with an InGaAs cell without a *BSR* (hereafter called *Blackbody*), characterized by no spectral selectivity. We set the thickness of the InGaAs layer in the *Blackbody* case to twice that of the *BSR* case, such that the optical path lengths through InGaAs are approximately equal.

A significant enhancement in efficiency, relative to the blackbody case, is predicted for cells with a reflective back surface, suggesting it is an essential feature for achieving high efficiency. For example, the *BSR* case is predicted to achieve 43% efficiency when paired with a 1500 K emitter, whereas the *Blackbody* case achieves only 8% efficiency under these conditions. Use of a MgF_2 back spacer increases this efficiency gain further. The *Spacer* case is predicted to exhibit 8% greater (absolute) efficiency than the BSR case because of its higher sub-bandgap reflectance (98.9% vs. 96.8%).

An anti-reflection coating, on the other hand, is less important for improving efficiency. However, an *ARC* considerably improves the above bandgap absorptance and, consequently, the power density. For example, the *ARC* case exhibits ~0.8 W/cm^2 higher power density than either the *BSR* or the *Spacer* case.

Table 5.1: Optimized architecture and performance for InGaAs structures (Th = 1500 K).

	MgF_2 [μm]	**ZnSe [μm]**	**InGaAs [μm]**	**MgF_2 [μm]**	**Back surface**	**$\bar{a}(E \geq E_g)$ [%]**	**$\bar{a}(E<E_g)$ [%]**	**η [%]**	**P_{out} [W cm^{-2}]**
BSR	-	-	0.97	-	Au	60.8	3.2	42.9	1.52
ARC	0.20	0.10	2.78	-	Au	92.2	3.7	44.6	2.27
Spacer	-	-	1.1	0.44	Au	61.1	1.1	51.0	1.52
Combined	0.46	0.15	1.46	0.42	Au	82.3	1.4	51.7	2.07
Blackbody	*	*	1.93	-	Black	100	100	8.1	2.32

* The hypothetical *Blackbody* case is assumed to have perfect broadband absorptance.

5.6. Structure Optimization

To optimize the overall cell architecture, we modeled a TPV cell with *ARC* and *Spacer* (Figure 5.2 (d)), hereafter called the *Combined* case. The optimized *Combined* case exhibits high spectral selectivity (Figure 5.5 (a)), achieving higher above-bandgap absorptance than the Spacer case without significantly compromising sub-bandgap reflectance (Table 5.1). Because of its superior optical properties, the *Combined* case is predicted to operate with higher efficiency than either the *BSR* or *Spacer* case (Figure 5.5 (b)) and with a power output approaching that of the *ARC* case (Figure 5.5 (c)). Specifically, for an optimized *Combined* cell, we predict an efficiency of 52% and a power output of 2.1 W/cm^2 when paired with a 1500 K blackbody emitter.

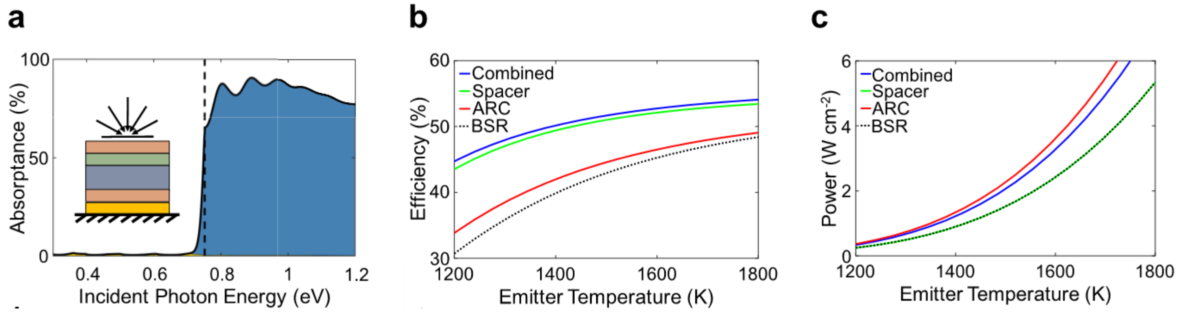

Figure 5.5: Combined structure.

(a) Calculated hemispherical averaged optical response of the *Combined* structure. Blue and yellow shading indicates specific absorption by the InGaAs and Au layer, respectively. Inset: Structure schematic. Comparison of predicted (b) efficiency, (c) power output for each case, optimized given its discrete set of layers.

These simulations suggest that spacers are an important feature of high-efficiency thin-film InGaAs cells. Spacers limit parasitic absorption by the metal contact by reducing the intensity that reaches the back interface. Provided that parasitic absorption is mitigated in the active layers, average sub-bandgap reflectance approaching 99% may be achieved with the use of a back spacer. Development of a TPV device with a back spacer will require the design of electrical contacts capable of collecting charge carriers laterally or across this dielectric region. Prior demonstration of a TPV device with dielectric claddings (ARC and spacer) utilized monolithic series interconnections to electrically contact the active region[21]. Similar design elements may be appropriate for developing TPV modules with the proposed MgF_2 spacer.

5.7. Conclusion

In summary, we demonstrated high spectral selectivity in thin-film structures by using back surface reflectors and by optimizing interference. Specifically, we fabricated thin-film structures with record high average sub-bandgap reflectance (~96%). We identified that reflective back

surfaces are the most important feature for high efficiency cells. The enhanced reflectance due to a dielectric spacer layer, between the InGaAs and the Au back contact, results in predicted TPV efficiencies above 50% for a 1500 K black emitter. When combined with a double-layer anti-reflection coating, high power densities (~2 W/cm^2) are also achievable. The potential for a dramatic increase of conversion efficiency through improved spectral selectivity, combined with the potential for reduced module costs through wafer reuse, supports the prospect of thin-film TPVs for applications in distributed power generation. Beyond the high spectral selectivity demonstrated here, development of high-performance thin-film TPV systems will require precise doping of active materials and design of selective electrical contacts with low parasitic absorption.

CHAPTER 5

Bibliography

1. Coutts, T. J. Overview of thermophotovoltaic generation of electricity. *Sol. Energy Mater. Sol. Cells* **66**, 443–452 (2001).

2. Bianchi, M., Ferrari, C., Melino, F. & Peretto, A. Feasibility study of a Thermo-Photo-Voltaic system for CHP application in residential buildings. *Appl. Energy* **97**, 704–713 (2012).

3. Durisch, W. & Bitnar, B. Novel thin film thermophotovoltaic system. *Sol. Energy Mater. Sol. Cells* **94**, 960–965 (2010).

4. Fraas, L. M., Avery, J. E. & Huang, H. X. Thermophotovoltaic furnace – generator for the home using low bandgap GaSb cells. *Semicond. Sci. Technol.* **18**, 247–253 (2003).

5. Amy, C. *et al.* Pumping liquid metal at high temperatures up to 1,673 kelvin. *Nature* **550**, 199–203 (2017).

6. Seyf, H. R. & Henry, A. Thermophotovoltaics: a potential pathway to high efficiency concentrated solar power. *Energy Environ. Sci.* **9**, 2654–2665 (2016).

7. Datas, A., Chubb, D. L. & Veeraragavan, A. Steady state analysis of a storage integrated solar thermophotovoltaic (SISTPV) system. *Sol. Energy* **96**, 33–45 (2013).

8. Datas, A., Ramos, A., Martí, A., del Cañizo, C. & Luque, A. Ultra high temperature latent heat energy storage and thermophotovoltaic energy conversion. *Energy* **107**, 542–549 (2016).

9. Bitnar, B. Silicon, germanium and silicon/germanium photocells for thermophotovoltaics applications. *Semicond. Sci. Technol.* **18**, S221 (2003).

10. Siergiej, R. R. *et al.* 20% efficient InGaAs/InPAs TPV cells. in *Thermophotovoltaic Generation of Electricity 5th Conference* 414–423 (2003).

11. Wernsman, B. *et al.* Greater than 20% radiant heat conversion efficiency of a thermophotovoltaic radiator/module system using reflective spectral control. *IEEE Trans.*

Electron Devices **51**, 512–515 (2004).

12. Ganapati, V., Xiao, T. P. & Yablonovitch, E. Ultra-Efficient Thermophotovoltaics Exploiting Spectral Filtering by the Photovoltaic Band-Edge arXiv : 1611 . 03544v2 [physics . optics] 7 Feb 2018. 1–14 (2018).

13. Lenert, A., Nam, Y., Bierman, D. M. & Wang, E. N. Role of spectral non-idealities in the design of solar thermophotovoltaics. *Opt. Express* **22**, A1604 (2014).

14. Miller, O. D., Yablonovitch, E. & Kurtz, S. R. Strong internal and external luminescence as solar cells approach the Shockley-Queisser limit. *IEEE J. Photovoltaics* **2**, 303–311 (2012).

15. Swanson, R. M. Silicon photovoltaic cells in thermophotovoltaic energy conversion. in *1978 International Electron Devices Meeting* 70–73 (IRE, 1978).

16. Jurczak, P., Onno, A., Sablon, K. & Liu, H. Efficiency of GaInAs thermophotovoltaic cells: the effects of incident radiation, light trapping and recombinations. *Opt. Express* **23**, A1208 (2015).

17. Lee, K., Zimmerman, J. D., Hughes, T. W. & Forrest, S. R. Non-Destructive Wafer Recycling for Low-Cost Thin-Film Flexible Optoelectronics. *Adv. Funct. Mater.* **24**, 4284–4291 (2014).

18. Lee, K., Lee, J., Mazor, B. A. & Forrest, S. R. Transforming the cost of solar-to-electrical energy conversion: Integrating thin-film GaAs solar cells with non-tracking mini-concentrators. *Light Sci. Appl.* **4**, e288 (2015).

19. Wu, X. *et al.* A Study of Contacts and Back-Surface Reflectors Interconnected Modules. **517**, (1999).

20. Clevenger, M. B. *et al.* Optical properties of thin semiconductor device structures with reflective back-surface layers. in *Fourth NREL conference on thermophotovoltaic generation of electricity* 327–334 (2011).

21. Wang, C. *et al.* Wafer Bonding and Epitaxial Transfer of GaSb-Based Epitaxy to GaAs for Monolithic Interconnection of Thermophotovoltaic Devices. *J. Electron. Mater.* **33**,

213–217 (2004).

22. Born, M. & Wolf, E. *Principles of Optics*. (Perfamon Press Ltd., 1970).

23. Deng, X.-H., Liu, J.-T., Yuan, J.-R., Liao, Q.-H. & Liu, N.-H. A new transfer matrix method to calculate the optical absorption of graphene at any position in stratified media. *Europhys. Lett.* **109**, 27002 (2015).

24. Li, H. H. Refracfive Index of Alkali Halides and Its Wavelength end Temperature Derivatives. *J. Phys. Chem. Ref. Data* **5**, 329–528 (1976).

25. Tatian, B. Fitting refractive-index data with the Sellmeier dispersion formula. *Appl. Opt.* **23**, 4477 (1984).

26. Connolly, J., DiBenedetto, B. & Donadio, R. Specifications Of Raytran Material. in *Proc. SPIE* (ed. Fischer, R. E.) 141–144 (1979).

27. Palik, E. D. *Handbook of optical constants of solids*. (Academic Press, 1998).

28. Dixon, J. R. & Ellis, J. M. Optical properties of N-type indium arsenide in the fundamental absorption edge region. *Phys. Rev.* **123**, 1560–1566 (1961).

29. Sturge, M. D. Optical absorption of gallium arsenide between 0.6 and 2.75 eV. *Phys. Rev.* **127**, 768–773 (1962).

30. Olmon, R. L. *et al.* Optical dielectric function of gold. *Phys. Rev. B* **86**, 235147 (2012).

31. Krier, A. *Mid-infrared Semiconductor Optoelectronics*. (Springer, 2006).

32. Ahrenkiel, R. K., Ellingson, R., Johnston, S. & Wanlass, M. Recombination lifetime of In0.53Ga0.47As as a function of doping density. *Appl. Phys. Lett.* **72**, 3470–3472 (1998).

Chapter 6

Nearly Perfect Photon Utilization in an Air-Bridge Thermophotovoltaic Cell

Thermophotovoltaic (TPV) cells are similar to solar cells, but instead of converting solar radiation to electricity, they are designed to utilize locally radiated heat. Development of high efficiency TPV cells has the potential to enable widespread applications in grid-scale thermal energy storage[1,2], direct solar energy conversion[3–8], distributed co-generation[9–11], and waste heat scavenging[12]. To reach high efficiencies, TPV cells must utilize the broad spectrum of a radiative thermal source. The challenge arises because most of the thermal radiation is in a low-energy wavelength range that cannot be used to excite electronic transitions and generate electricity. One promising approach to overcome this challenge is to have low-energy photons reflected and re-absorbed by the thermal emitter, where their energy can have another chance at contributing toward photogeneration in the cell. However, current methods for photon recuperation are limited by insufficient bandwidth or parasitic absorption, resulting in large efficiency losses relative to theoretical limits. In this work, we demonstrate an unconventional TPV-suspended-over-air architecture that enables nearly perfect reflection of low-energy photons. By embedding an air layer within a thin-film $In_{0.53}Ga_{0.47}As$ TPV cell, a four-fold reduction in parasitic absorption relative to existing TPV cells is achieved. This level of photon utilization enables an 8% absolute gain in efficiency compared to a state-of-the-art architecture and a record-high power conversion

efficiency exceeding 31%, as measured with a 1500 K blackbody emitter. As out-of-band reflectance approaches unity, TPV efficiency becomes nearly insensitive to cell bandgap and emitter temperature. Accessing this regime unlocks a range of possible materials and heat sources that were previously inaccessible to TPV energy conversion.

6.1. Introduction

Thermophotovoltaics utilize locally emitted thermal radiation to generate electricity. Similar to solar PVs, sufficiently high energy photons (so-called in-band, IB photons) radiated from a thermal emitter excite electronic transitions in the cell. Photogenerated charge carriers are subsequently separated and extracted as electricity. The challenge in TPV cells is that most thermal emitters operate at temperatures between 1000 and 2500 K[13–16]. In this temperature range, a large fraction of out-of-band (OOB) photons carry energy below the semiconductor bandgap and are thus unavailable for exciting electronic transitions[17].

Unlike solar PV cells, however, OOB thermal radiation in a TPV can be recycled back to the closely positioned emitter using spectral control, enabling recovery of the unconverted energy[18]. High OOB cell reflectance can be engineered through use of a back-surface reflector (BSR), front-surface filter (FSF), or both. Swanson reported[19] the development of a Si TPV cell with 95% OOB reflectance, enabling a power conversion efficiency of 29% using a 2300 K broadband emitter. Omair *et al.* recently reported[20] a thin-film $In_{0.53}Ga_{0.47}As$ (InGaAs) cell exhibiting 29.1% efficiency and 94.6% OOB reflectance, paired with a 1480 K graphite emitter. This demonstration represents the highest reported efficiency for any TPV to date. Nevertheless, selective reflectors, including metallic back-surface reflectors[19–21], Bragg/plasma filters[22], and photonic crystals[23],

have yet to exceed 95% OOB reflectance. At this level, the largest losses relative to theoretical limits are due to spectral inefficiencies. 5% OOB reflectance loss, although seemingly small, lowers TPV efficiency by ~10% absolute[24] due to the importance of low-energy photons. We recently developed an InGaAs-on-dielectric thin-film structure that exhibited a record-high OOB reflectance of 96%[24]. The reflectance of this structure, however, fell short of the prediction by ~3% due to absorption losses from residual H_2O in the dielectric spacer adjacent to the Au BSR.

Here we demonstrate an alternative approach where the dielectric spacer within the thin-film cell is replaced with air. The air-bridge InGaAs TPV cell absorbs most of the IB radiation to generate electricity while serving as a nearly perfect mirror with ~99% OOB reflectance. This high reflectance enables a TPV power conversion efficiency exceeding 31% using a 1500 K emitter. This approach eliminates parasitic absorption in the dielectric and maximizes the refractive index mismatch at each interface. Furthermore, TPVs enter a fundamentally different regime when OOB reflectance approaches unity. While the trade-off between bandgap and photocurrent must be made in conventional devices with < 95% OOB reflectance[17], the spectral efficiency becomes nearly insensitive to the bandgap or to the temperature of the thermal emitter at 99% OOB reflectance, potentially allowing for the exploitation of low-cost semiconductors such as Si that have heretofore been impractical.

The benefits of an air-bridge architecture are apparent from a theoretical comparison of energy flows and losses in a TPV utilizing a conventional thin-film and an air-bridge cell (Figure 6.1). In Figure 6.1 (a), a hot thermal source radiates photons with a broad, blackbody spectrum. Photons with energy (E) greater than the TPV semiconductor bandgap (E_g) are absorbed and generate current, while photons with $E < E_g$ travel through the TPV, are reflected by the BSR, and re-absorbed by the emitter.

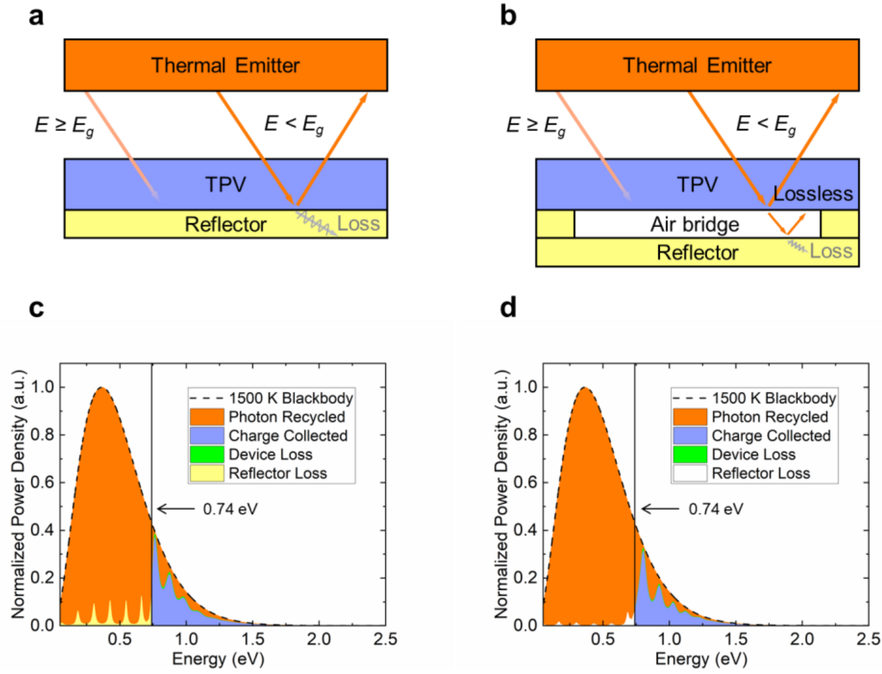

Figure 6.1: Photon utilization in air-bridge thermophotovoltaics (TPVs).
Conceptual schematics of energy flow in (a) a conventional thin-film TPV with Au versus (b) a thin-film TPV with air-bridge reflector. (c) Power distribution of a conventional thin-film InGaAs cell (E_g = 0.74 eV) with a Au BSR operated with a 1500 K blackbody source (structure given in Extended Data Fig. 1). The dashed line shows the normalized power density of the blackbody, and the cell absorption spectrum is calculated using transfer matrix methods[29]. (d) Power distribution of the air-bridge TPV shown in (b) operated using a 1500 K blackbody emitter.

Conventional reflectors such as Au introduce a loss of ~5% at the semiconductor/Au interface for every reflection/re-absorption cycle. In contrast, when an air cavity is integrated within the cell (Figure 6.1 (b)), photons with $E < E_g$ experience lossless Fresnel reflection at the TPV/air interface. Photons that transmit through this interface are then reflected by the Au with < 2% reflectance loss at the air/Au interface. When integrated over the emitter spectrum, OOB absorption by the conventional thin-film cell is 4.7%, representing the primary source of loss (see Figure 6.1 (c)). Other loss pathways include carrier collection (~2.5%). The absorption oscillations are Fabry-Perot modes formed in the cavity between the reflector and the TPV. In comparison, the air-bridge cell loses only 1.1% of power to OOB absorption (Figure 6.1 (d)). From these

calculations, both cells have a similar energy transfer efficiency in the in-band region (61.1% for conventional vs. 61.8% for air-bridge), whereas the air-bridge structure effectively reduces the OOB losses by more than 4 times compared to the conventional cell.

6.2. Device Fabrication

A lattice-matched, inverted *P-n-N* heterostructure thermophotovoltaic (TPV) cell is epitaxially grown on a 350 μm thick (100) InP substrate using GENxplore Molecular Beam Epitaxy (Veeco Corp., MN, 55127). The heterostructure comprises a 200 nm undoped InP buffer layer, 200 nm Be-doped (1×10^{18} cm^{-3}) $In_{0.53}Ga_{0.47}As$ (InGaAs) contact layer, 200 nm Be-doped (1×10^{18} cm^{-3}) InP front window layer, 1 μm nm Si-doped (1×10^{17} cm-3) InGaAs absorption layer, 100 nm Si-doped (1×10^{18} cm^{-3}) InP back window layer, and 100 nm Si-doped (1×10^{18} cm^{-3}) InGaAs contact layer.

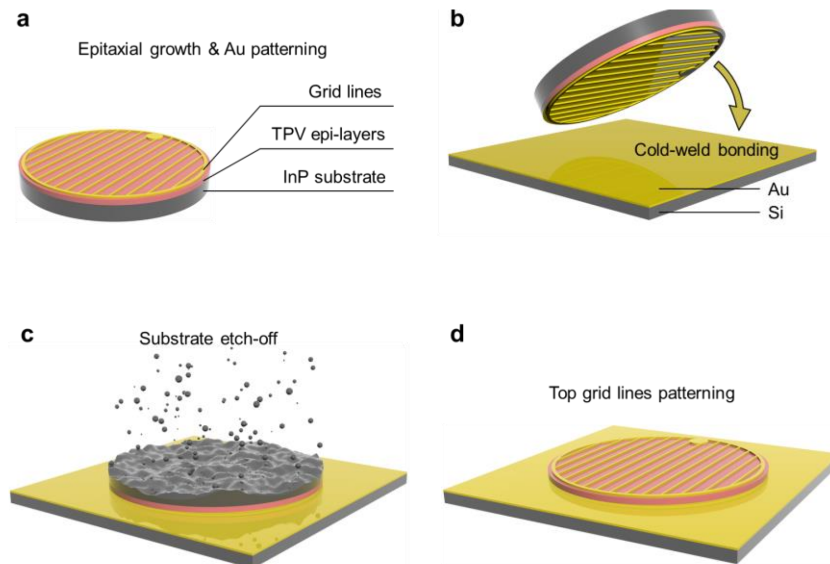

Figure 6.2: Air-bridge TPV cell fabrication.
(a) TPV active layers growth and cathode grid line patterning. (b) Cold-weld bonding to a Si substrate coated with Au, (c) substrate removal via etching in HCl, and (d) top anode grid line patterning.

Figure 6.2 illustrates key steps in fabricating the air-bridge cell. The native oxide on the epitaxial surface is removed in buffered HF for 90 s and rinsed in de-ionized (DI) water for 10 s. All layers are photolithographically patterned using LOR 3A (MicroChem Corp., MA, 01581) and SPR 220 3.0 (MicroChem Corp., MA, 01581) bilayer photoresist. Cathode contacts (10 nm Ti/ 590 nm Au, E-beam evaporated) are patterned first with 2.95/2.85 mm outer/inner diameter ring contact filled with 8 µm wide metal grids. The grid-to-grid spacing is 80 µm, giving an ~10 % grid coverage (i.e., a 90 % geometric fill factor). The sample is then soaked in H_3PO_4: H_2O_2:H_2O = 1:1:8 solution for 20 s to remove the 100 nm n-type InGaAs contact layer, while the contact layer underneath the cathode contact metal is protected to minimize the contact resistance. The sample is bonded to a Si substrate coated with 5 nm Ti/ 300 nm Au (E-beam evaporated) by applying heat (150°C) and pressure (10 MPa) for 5 min using an EVG 510 wafer bonder (EV Group Inc., NY, 12203). Next, the InP substrate is removed by immersion in dilute HCl (HCl:H_2O = 1:1) for 16 hr, leaving only the active TPV epitaxial layers suspended over air bridges, and supported by the buried grid lines. This destructive substrate removal step can be substituted by non-destructive epitaxial lift-off (ND-ELO)[25,26] to recycle the costly InP growth substrate. The TPV mesa (3 mm diameter) is subsequently patterned by alternatively soaking the sample in InGaAs etchant (citric acid: H_2O_2 = 4:1) and InP etchant (HCl:H_2O = 1:1). Finally, the top anode contact (10 nm Ti/ 30 nm Pt/ 500 nm Au, E-beam evaporated) that is coincident with the buried cathode contact is patterned, and the 200 nm p-type InGaAs contact layer is removed using citric acid: H_2O_2 = 4:1 for 2 min.

The fabrication procedure provides two significant advantages. First, the air cavity thickness can be accurately controlled within nanometers by the thickness of buried Au grid lines. Second, all the air cavities are encapsulated through Au-Au cold-weld bonding. This protects the

TPV bottom surface from damage by the HCl substrate etchant. Figure 6.3 (a) is an image of the air-bridge TPV cell. The 3 mm diameter device is covered with multiple 8-μm grid lines. As the bottom and top grid lines are aligned, normally incident photons encounter only the TPV/air interface when they penetrate the device active layers. The device has been cleaved perpendicular to the grid lines to reveal its cross-section (Figure 6.3 (b) and (c)). The 0.6 μm high × 72 μm wide air cavity in Figure 6.3 (b) is uniform along the entire span between two supporting grid lines with no apparent bowing (< 0.1%, see Figure 6.4).

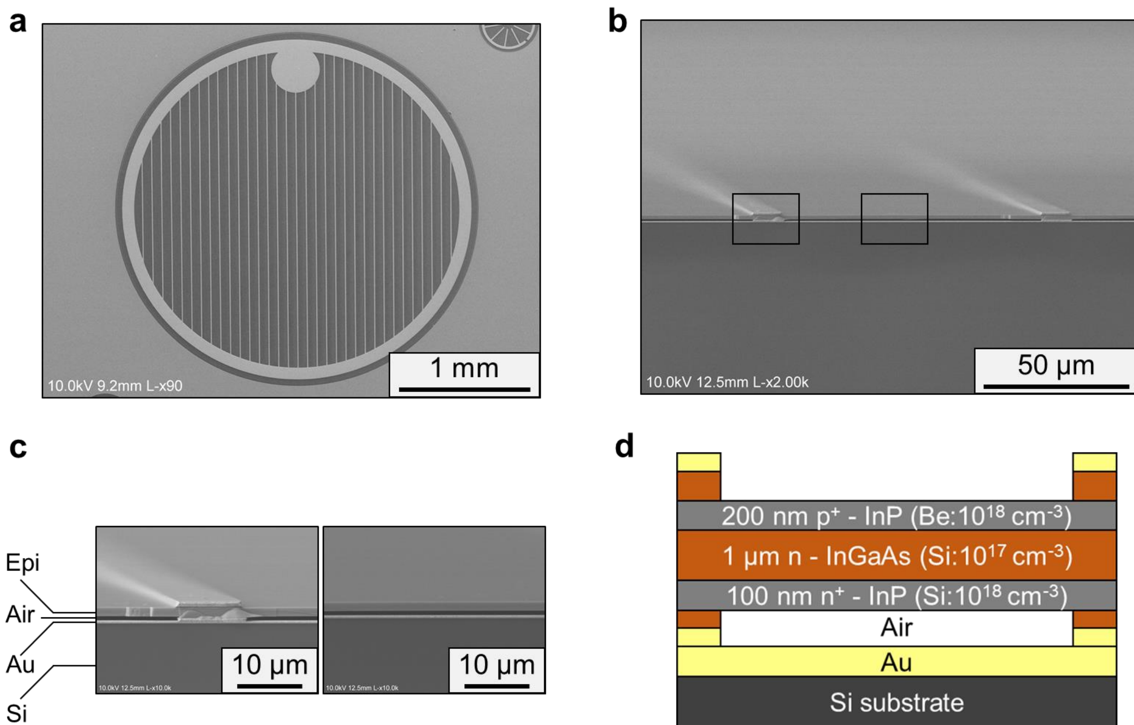

Figure 6.3: Structure of the air-bridge cell.

(a) Top view scanning electron microscope (SEM) image of the air-bridge TPV. (b) Cross-section SEM images of the air-bridge, and (c) high magnification images of black boxes in (b). (d) Schematic of the TPV active layers.

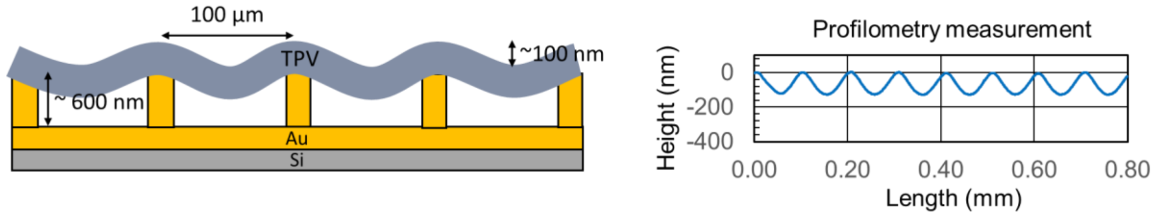

Figure 6.4: Air-bridge bowing.

(left) Schematic of an air-bridge TPV cell without top contact grid lines, and (right) the top surface profilometry measurement of the same cell with 100 μm grid spacing. The designed air cavity thickness is 700 nm. TPV epitaxial layers slightly bow downward by about 100 nm (~0.1% of the lateral span of each air cavity).

6.3. Spectral Properties

The spectral properties of the Au reflector and air-bridge cells were characterized using Fourier transform infrared (FT-IR) spectroscopy (Spectrum GX FT-IR microscope, Perkin-Elmer, MA, 02451). The measurements were done in the near-IR spectral region (12000 cm^{-1} to 1800 cm^{-1}) with a 0.3 mm × 0.3 mm aperture using a CaF_2 beam splitter and a liquid nitrogen cooled InSb detector. As weighted by the 1500 K blackbody emission spectrum, the average OOB power reflectance is 95.3% for the Au reflector cell, and 98.5% for the air-bridge cell (Figure 6.5 (a)). The average IB power absorption is 63.6% and 61.2% for the Au reflector and the air-bridge cells, respectively (Figure 6.5 (b)). This is consistent with the simulated absorption in Figure 6.6.

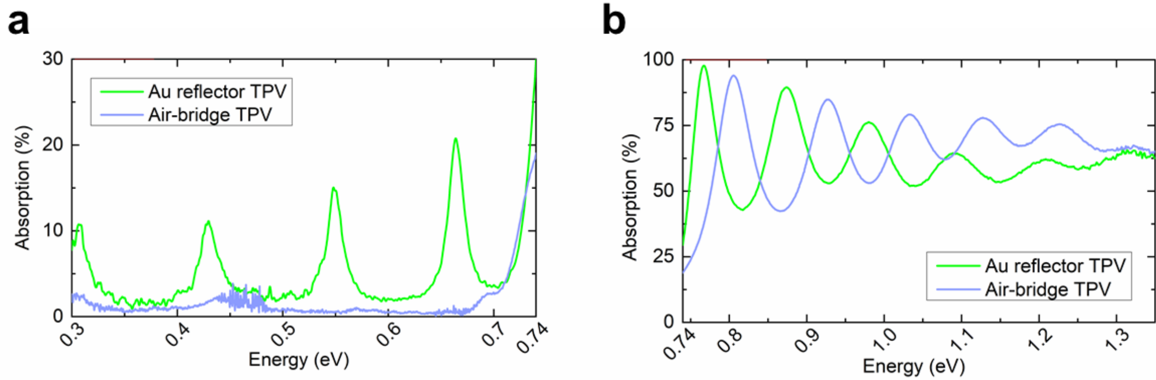

Figure 6.5: Spectral properties of the Au reflector and the air-bridge TPVs.

(a) Out-of-band (OOB, $E < E_g = 0.74$ eV) and (b) In-band (IB, $E \geq E_g$) absorption spectra of Au reflector (green) and air-bridge TPVs (blue).

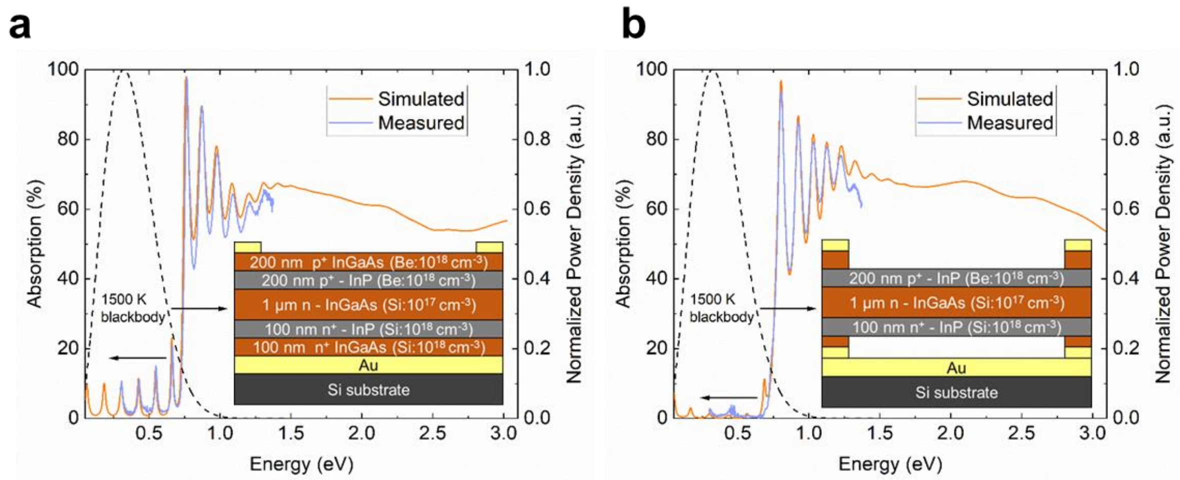

Figure 6.6: Absorption spectra of Au reflector and air-bridge TPV.

(a) Simulated (orange) and measured (blue) absorption spectra of the Au reflector TPV (structure in inset) using Fourier-transform infrared (FT-IR) spectroscopy. The optical cavity formed by the Au reflector and the TPV thin films leads to increased absorption by the Au reflector by creating several interference peaks. (b) Simulated (orange) and measured (blue) absorption spectra of the air-bridge TPV (structure in inset) using FT-IR. The air-bridge TPV features a lossless reflective semiconductor/air interface, effectively eliminating most parasitic out-of-band absorption.

Figure 6.7 presents the simulated absorption spectrum and the measured IB external quantum efficiency (*EQE*) spectrum for normal incident light on the air-bridge TPV cell. From

these results and the measured absorption, we obtain an average *IQE* = 98.4% for the air-bridge cell. *EQE* is measured using monochromatic illumination chopped at 200 Hz and coupled into a multimode SMA to bare fiber optic patch cable (Part Number: M118L02, Thorlabs, NJ, 07860) oriented normal to the TPV cell. The output signal is collected by a SR830 lock-in amplifier. The light illumination power is calibrated using a reference 818-UV/DB Si detector (Newport, CA, 92606) from 400 to 900 nm, a reference 818-IG InGaAs detector (Newport, CA, 92606) from 900 to 1650 nm, and a reference FDG03 Ge detector (Thorlabs, NJ, 07860) from 1650 to 1800 nm.

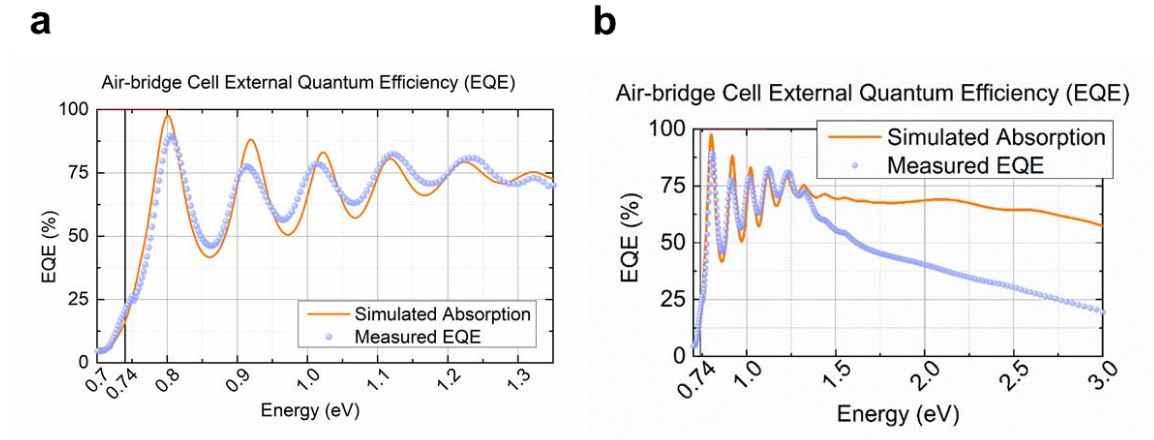

Figure 6.7: External quantum efficiency (EQE) of the air-bridge cell.

(a) Simulated absorption spectrum (orange line) using transfer matrix methods and measured external quantum efficiency (blue dots) of the air-bridge TPV cell from 0.7 eV to 1.35 eV (b) Extended data from 0.7 eV to 3.1 eV. The discrepancy is due to absorption of the front InP (bandgap energy E_g = 1.35 eV) window layer. Photons with E > 1.35 eV are partially absorbed in the 200 nm front InP window layer and do not contribute to current in the TPV active material (InGaAs).

The spectral enhancements of the air-bridge architecture are accurately described by the spectral efficiency, *SE*, which captures the combined effects of the enhancement of IB and suppression of OOB radiative transport [17]. $SE = \frac{E_g \cdot \int_{E_g}^{\infty} \varepsilon_{eff}(E) \cdot b(E,T_h)\, dE}{\int_0^{\infty} \varepsilon_{eff}(E) \cdot E \cdot b(E,T_h)\, dE}$ where $b(E,T_h)$ is the

spectral photon flux of the emitter, and $\varepsilon_{eff}(E) = \frac{\varepsilon_e \varepsilon_c}{\varepsilon_e + \varepsilon_c - \varepsilon_e \varepsilon_c}$ is the effective emissivity, where ε_e is the emissivity of the emitter, and ε_c is the emissivity/absorptivity of the cell. *SE* captures the dependence of the performance metric on the spectral properties of both the emitter and the cell and corrects for multiple reflections across the emitter/cell cavity. *SE* is penalized by spectral losses associated with parasitic out-of-band absorption, the reflectance of usable, in-band absorption, and thermalization of high energy photons. Also, we define average in-band absorption as $A_{in} = \frac{\int_{E_g}^{\infty} \varepsilon_c(E) \cdot E \cdot b(E,T_h)\, dE}{\int_{E_g}^{\infty} E \cdot b(E,T_h)\, dE}$, and average out-of-band reflectance as $R_{out} = \frac{\int_0^{E_g} (1-\varepsilon_c(E)) \cdot E \cdot b(E,T_h)\, dE}{\int_0^{E_g} E \cdot b(E,T_h)\, dE}$. We find *SE* = 58.1% and 72.9% for the Au reflector and the air-bridge TPV cells, respectively (Figure 6.8, denoted by stars). The dashed curve through the top red star represents simulated *SE* with an IB absorption of A_{in}= 0.61 and OOB reflectance of R_{out} = 0.99, consistent with measurements of the air-bridge cell. We also present previous results of Wernsman *et al.*[21] (circle) and Omair *et al.*[20] (square) for comparison, along with the simulated *SE* for A_{in}= 1 and various R_{out}. Within the common range of source temperatures, OOB loss dominates with increasing bandgap. However, when R_{out} > 0.99 (orange region), this dependence vanishes, suggesting that the cell design becomes insensitive to E_g and emitter temperature. Thus, the nearly perfect reflectance of the air-bridge design may allow low cost materials like Si to be used as TPV cells while maintaining a high *SE* at relatively low emitter temperatures (< 2000 K).

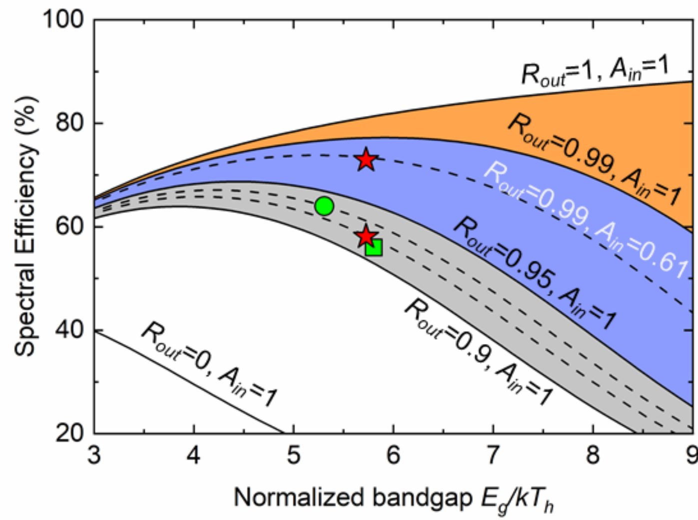

Figure 6.8: Spectral efficiency.

Measured spectral efficiency of the Au reflector and air-bridge TPVs (stars). Also shown are previous results (circle[21] and square[20]). The simulated spectral efficiencies are calculated for with various OOB reflectance (R_{out}) and IB absorptions (A_{in}) shown by lines.

6.4. Power Conversion Efficiency

The power conversion efficiency (PCE) is defined by:

$$PCE = \frac{P_{electrical}}{P_{incident} - P_{reflected}} \tag{6.1}$$

where $P_{electrical}$ is the electrical power generated, $P_{incident}$ is the incident power, and $P_{reflected}$ is the power reflected by the cell. Here, $P_{electrical} = V_{oc} \cdot I_{sc} \cdot FF$, where V_{oc} is the open-circuit voltage, I_{sc} is short-circuit current, and FF is the fill factor. The electrical power generated under illumination can be obtained directly from the cell current-voltage (I-V) characteristics while the incident and reflected power can be calculated from the spectral emissivity of the cell and emitter.

The difference between the incident and reflected power on the cell (i.e., absorbed power) can be expressed as[20]:

$$P_{incident} - P_{reflected} = A \cdot VF \cdot \int_0^\infty \varepsilon_{eff}(E) \cdot E \cdot b(E, T_h)\, dE \tag{6.2}$$

where A is the cell area, and VF is the geometric view factor accounting for the fractional solid angle subtended by the emitter as viewed from the cell. VF can be calibrated from the measured short-circuit current via:

$$I_{sc} = q \cdot A \cdot VF \cdot \int_{E_g}^\infty \varepsilon_{eff}(E)/\varepsilon_c(E) \cdot EQE(E) \cdot b(E, T_h)\, dE \tag{6.3}$$

where q is the unit charge. With a known emitter spectrum, the integral is a fixed value. Then, for each measurement, VF can then be calculated from the measured I_{sc}. The total power is integrated from 0.05 eV to 3.1 eV. The amount of power out of this range is negligible (< 0.3 %) for a ~1500K emitter.

The PCE of each cell under various illumination conditions is measured using the setup shown in Figure 6.9. The cell is mounted on a customized water-cooling stage. A close-loop chiller (Part Number: Isotemp 4100 R20, Fisher Scientific PA, 15275) flows water through the stage to keep the temperature at 20°C. The thermal emitter (SiC globar or cavity blackbody source) is mounted on a 3-axis translational stage (not shown). View factors can be varied by changing the distance between the TPV and the thermal emitter. View factors achieved by using the cavity blackbody source are limited due to the large dimension (8 inches in diameter) of its housing.

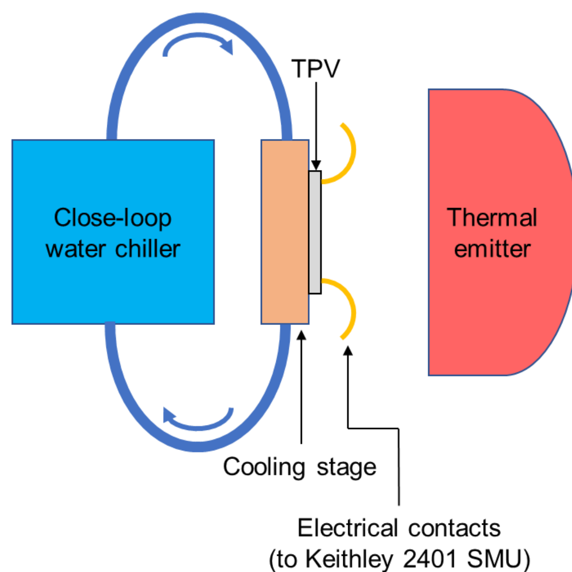

Figure 6.9: Schematic of the TPV efficiency measurement setup.

The results are presented in Figure 6.10. The maximum PCE of our Au reflector cell is 22.3% at 323 mA/cm^2 under illumination by a globar emitter at 1500 K (view factor VF = 0.162), whereas the air-bridge device exhibits PCE = 31.2 ± 0.2 % at 1006 mA/cm^2 (VF = 0.507). The PCE of the air-bridge cell exhibits an > 8 % absolute improvement compared to the same cell fabricated on the Au reflector at a similar photocurrent under globar illumination. Given that these two cells have similar IB absorption (~60%), this improvement is primarily attributed to the reduction of OOB absorptance loss from ~5% to ~1%.

A complete parametric set of measured J_{sc}, VF, V_{oc}, FF, and PCE is provided in Figure 6.11 and Table 6.1. We also measured the air-bridge TPV cell under illumination from a true blackbody source with emissivity > 0.99 at 1473 K, achieving a maximum PCE = 31.3 ± 0.1 % at J_{sc} = 337 mA/cm^2 (VF = 0.134).

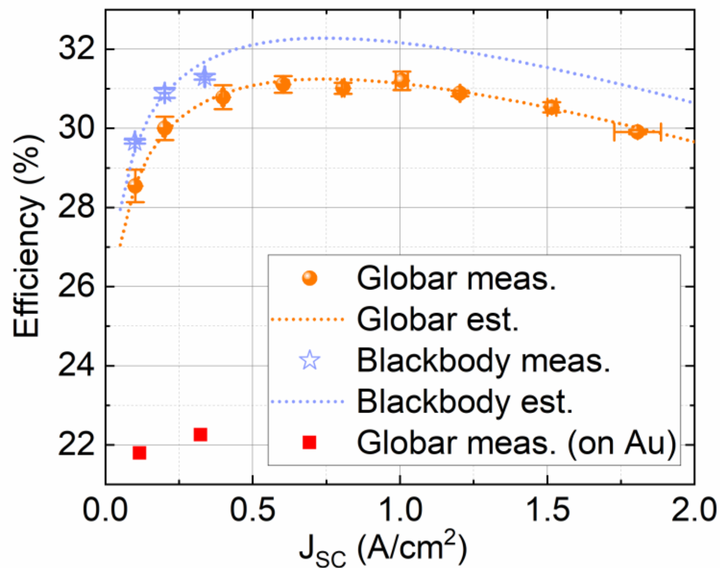

Figure 6.10: TPV power conversion efficiency (PCE)

PCE vs. short circuit current density (J_{sc}) of the Au reflector (squares) and the air-bridge TPV (circles) under 1500 K SiC globar illumination, and *PCE* of air-bridge TPV under 1473 K true blackbody illumination (stars). Also shown are the simulated *PCE*-J_{sc} curves of the air-bridge TPV.

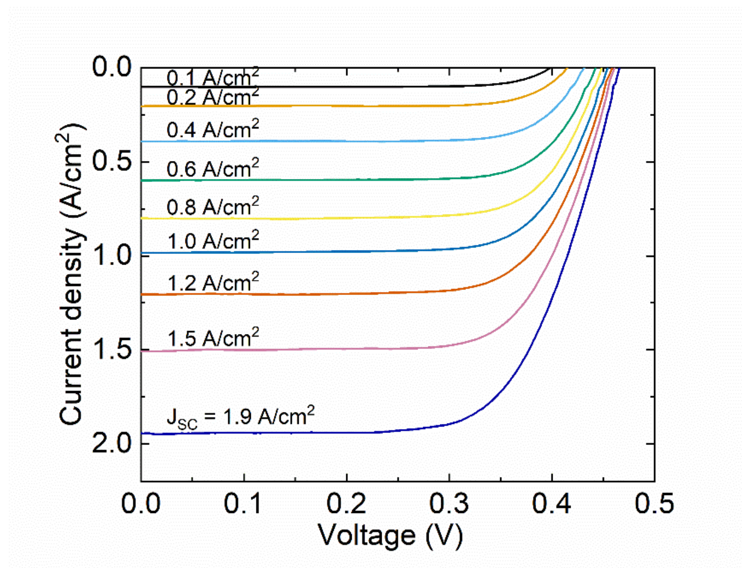

Figure 6.11: Current density (*J*)-voltage (V) characteristics of the air-bridge TPV measured under 1500 K SiC globar illumination with varying view factors.

Table 6.1: Parameters of Au reflector cell and air-bridge cell under illuminations.

Au reflector TPV: SiC globar (1500 K)				
VF	J_{sc} *(mA/cm²)*	V_{oc} *(mV)*	*FF (%)*	*PCE (%)*
0.058	116.12	394.0	73.26	21.79
0.162	323.06	419.5	70.27	22.26
Air-bridge TPV: SiC globar (1500 K)				
VF	J_{sc} *(mA/cm²)*	V_{oc} *(mV)*	*FF (%)*	*PCE (%)*
0.051	101.40 ± 0.54	397.9 ± 1.4	74.84 ± 0.88	28.54 ± 0.41
0.102	201.63 ± 2.49	416.3 ± 1.8	75.20 ± 0.82	30.00 ± 0.30
0.201	398.96 ± 4.80	432.4 ± 0.8	74.28 ± 0.66	30.79 ± 0.30
0.304	603.52 ± 2.30	442.8 ± 0.6	73.30 ± 0.49	31.11 ± 0.21
0.406	806.78 ± 4.49	449.6 ± 0.2	71.96 ± 0.32	31.01 ± 0.14
0.507	1005.97 ± 20.39	454.5 ± 1.5	71.44 ± 0.38	31.20 ± 0.23
0.606	1203.60 ± 1.34	457.8 ± 1.4	70.39 ± 0.21	30.88 ± 0.07
0.763	1515.05 ± 14.93	460.5 ± 0.9	69.17 ± 0.25	30.53 ± 0.13
0.910	1806.30 ± 79.11	464.1 ± 1.1	67.23 ± 0.25	29.91 ± 0.05
Air-bridge TPV: True blackbody (1473 K)				
VF	J_{sc} *(mA/cm²)*	V_{oc} *(mV)*	*FF (%)*	*PCE (%)*
0.040	100.00 ± 0.12	400.5 ± 1.0	74.80 ± 0.13	29.66 ± 0.05
0.080	201.08 ± 0.61	415.4 ± 1.5	75.12 ± 0.15	30.90 ± 0.13
0.134	336.76 ± 1.29	424.5 ± 1.4	74.47 ± 0.10	31.30 ± 0.07

We also modeled the performance of the air-bridge cell at higher blackbody illumination levels by fitting the measured, dark *I*-*V* characteristics to the diode equation. The *J*-*V* characteristic of the TPV with no illumination (dark) is expressed as:

$$J = J_{diff} + J_{SRH} + J_{sh} + J_{tun} \tag{6.4}$$

where $J_{diff} = J_0 \times \left(exp\left(\frac{qV}{kT}\right) - 1\right)$ is the diffusion current. J_0 is the diffusion saturation current that can be extrapolated from the forward linear region of a log(*J*)-*V* curve in the dark. $J_{SRH} = J_{GR} \times \left(exp\left(\frac{qV}{2kT}\right) - 1\right)$ is Shockley Read Hall (*SRH*) generation and recombination current. In

reverse bias, $J_{SRH} \approx J_{GR} = \frac{qn_iW}{\tau_{SRH}}$, where n_i is intrinsic doping concentration of the active material, W is the depletion width, and τ_{SRH} is the *SRH* lifetime. J_{GR} can be fit from the forward log(*J*)-*V* curve in the dark. $J_{sh} = V/R_{sh}$ is the current for device with shunt resistance R_{sh}, and J_{tun} is reverse tunneling current arising from the small bandgap[27] and trap levels[28] of the active materials. At large current, series resistance (R_s) is also important. Thus, V should be substituted by $(V - J \times R_s)$ in the above equations. By fitting the measured dark *J*-*V* curve (Figure 6.12) of the air-bridge TPV cell, we get: J_0 = 22.6 nA/cm^2, J_{GR} = 707.4 nA/cm^2, $R_{sh} > 2\times10^6$ Ω, $\tau_{SRH} > 4$ µs, and R_s = 26 mΩ·cm^2.

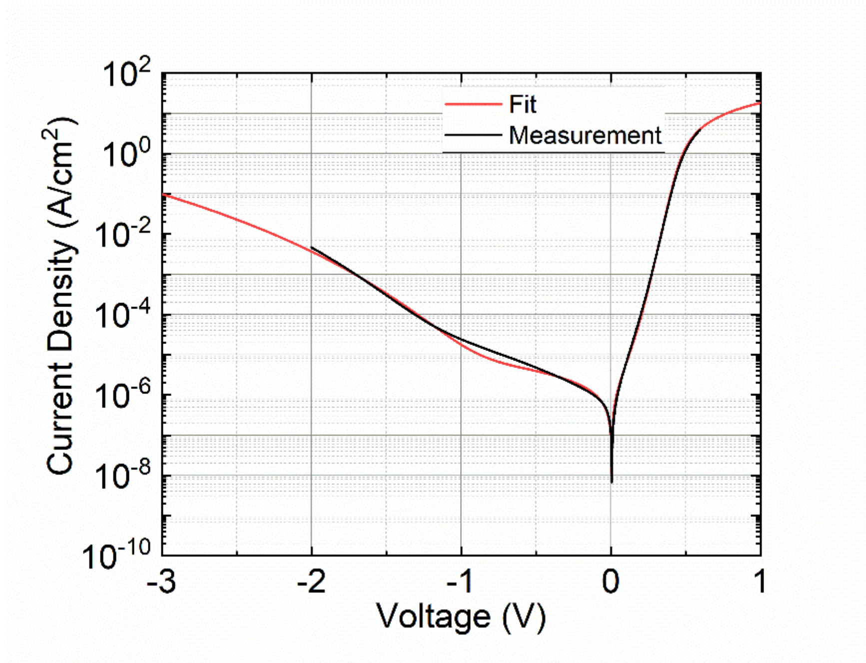

Figure 6.12: *J-V* characteristics of the air-bridge TPV under dark condition.

The reverse bias dark current is dominated by tunneling from -3 to -1 V, and by shunt resistance and generation and recombination of electron-hole pairs from -1 to 0 V. The forward bias dark current is dominated by generation and recombination from 0 to 0.2 V, by diffusion current from 0.2 to 0.5 V, and by series resistance above 0.5 V.

Under illumination, the *J*-*V* characteristic is: $J = J_{diff} + J_{SRH} + J_{sh} + J_{tun} - J_{ph}$, where J_{ph} is the photocurrent density. With the above parameters, the *J*-*V* curves are simulated at various J_{ph}. To within error, our measurement results agree with simulations which predict a maximum *PCE* = 32.3% at J_{sc} = 750 mA/cm^2.

The measured, voltage-dependent current density and power density at the highest measured efficiency (using the 1473 K blackbody source) are provided in Figure 6.13. We find J_{sc} = 337 mA/cm^2, V_{oc} = 0.425 V, FF = 74.47%, and the maximum power output P_{max} = 106.46 mW/cm^2. Results for the air-bridge cell using the 1500 K globar and 1473 K true blackbody source in Figure 6.14 (a) indicate that V_{oc} increases linearly with $\log(J_{sc})$, except at the highest currents where cell heating may become significant. FF increases at relatively low J_{sc} (<200 mA/cm^2) and drops dramatically with increasing J_{sc} due to series resistance, R_s (Figure 6.14 (b)).

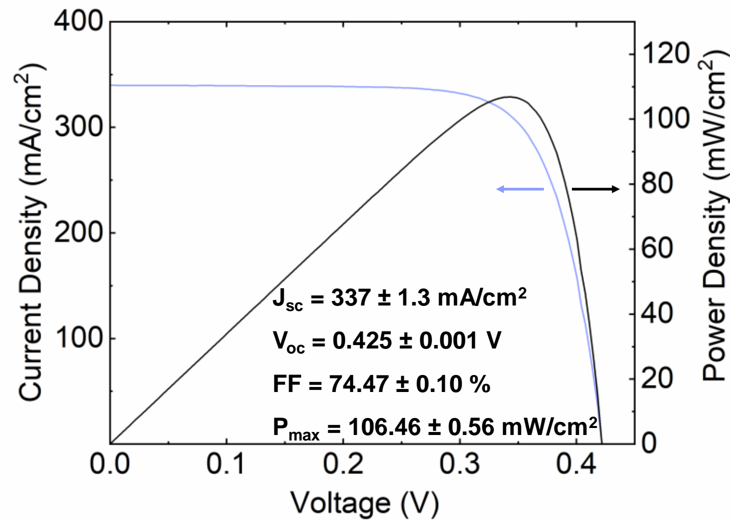

Figure 6.13: *J-V* and power density-voltage curves of the air-bridge TPV at maximum measured PCE.

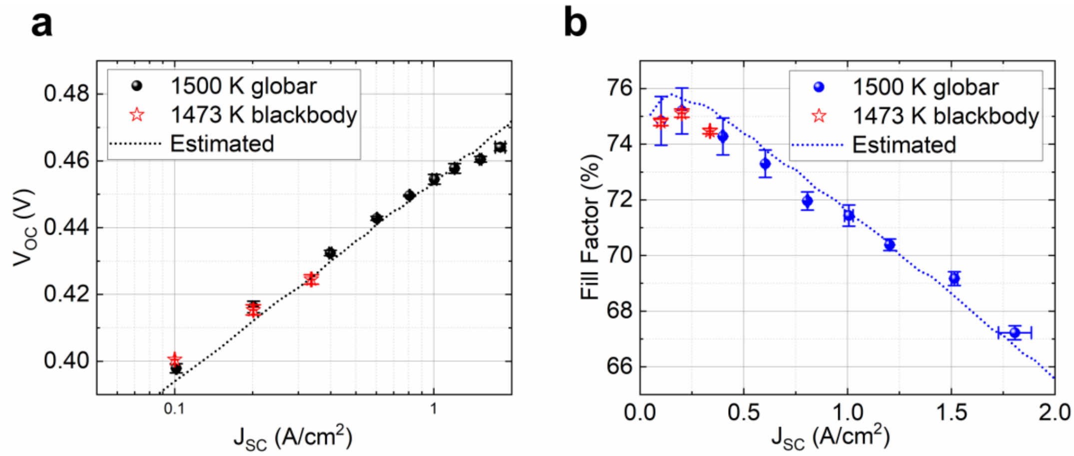

Figure 6.14: Open circuit voltage and fill factor.

(a) Measured open circuit voltage (V_{oc}) and (b) fill factor (*FF*) of the of the air-bridge TPV under 1500 K globar (black circles in (a), blue circles in (b)) and 1473 K true blackbody (stars) illumination. Also shown are the simulated V_{oc}-J_{sc} (dashed line in (a)) and *FF*-J_{sc} (dashed line in (b)) characteristics of the air-bridge TPV.

Details of R_s and other loss mechanisms that limit the efficiency of the air-bridge cell are provided in Figure 6.15[8,20]. Red stars represent the measured *PCE* of the air-bridge TPV. Figure 6.15 (a) shows the simulated *PCE* (black) with $VF = 0.134$, $A_{in} = 0.61$, $R_{out} = 0.99$, and $R_s = 26$ mΩ·cm^2. Other curves show the change of *PCE* when varying one of the above parameters. When $T < 1200$ K, *PCE* increases with T, while improving R_{out} provides the highest improvements to *PCE*. At $T > 1500$ K, *PCE* is limited by R_s. Without improving R_s, changes that increase the current will decrease *PCE*. Figure 6.15 (b) shows the simulated *PCE* with $R_s = 1$ mΩ·cm^2. R_{out} benefits *PCE* the most at $T < 1200$ K, while *VF* dominates at $T > 1200$ K. Thus, positioning the cell closer to the emitter is important at high T. Figure 6.15 (c) shows the simulated *PCE* curves with $R_s = 1$ mΩ·cm^2. $VF = 1$. Still, R_{out} benefits *PCE* the most at low T, while R_{out} and A_{in} are equally important when T is high. Further enhancement of *PCE* requires improving TPV materials quality by decreasing diffusion saturation current, generation and recombination lifetime, shunt resistance, etc.

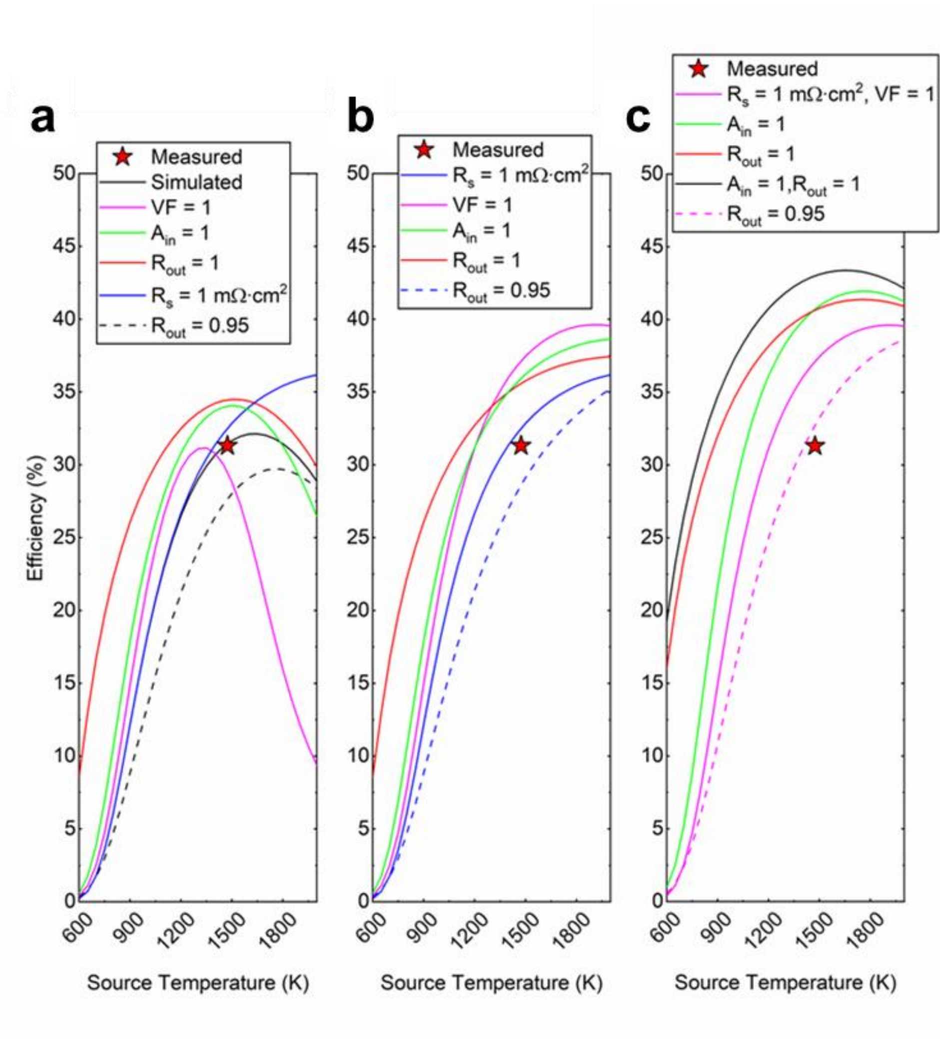

Figure 6.15: Power conversion efficiency (*PCE*) vs. source temperature (*T*).
Simulated *PCE* (black) with (a) $VF = 0.134$, $A_{in} = 0.61$, $R_{out} = 0.99$, and $R_s = 26$ mΩ·cm². (b) $R_s = 1$ mΩ·cm². (c) $R_s = 1$ mΩ·cm². $VF = 1$.

6.5. Conclusion

In summary, we demonstrate a TPV cell with nearly perfect spectral utilization, where loss of photogenerated carriers and parasitic absorption account for less than 3% of the power radiated by a ~1500 K blackbody. This was achieved by introducing an air layer within the thin-film TPV

cell, and represents a four-fold reduction in absorption of low-energy photons relative to the prior best TPV cells. By recuperating ~99 % of out-of-band radiated power, the efficiency of the air-bridge cell exhibits an > 8 % absolute improvement compared to the same cell fabricated on the Au reflector, and > 31% *PCE* for a 1500 K thermal emitter. Nearly perfect photon utilization enabled by the air-bridge design provides a potential pathway to use low cost cells and heat sources for TPV power conversion.

CHAPTER 6

Bibliography

1. Amy, C., Seyf, H. R., Steiner, M. A., Friedman, D. J. & Henry, A. Thermal energy grid storage using multi-junction photovoltaics. *Energy Environ. Sci.* **12**, 334–343 (2019).

2. Datas, A., Ramos, A., Martí, A., del Cañizo, C. & Luque, A. Ultra high temperature latent heat energy storage and thermophotovoltaic energy conversion. *Energy* **107**, 542–549 (2016).

3. Lenert, A. *et al.* A nanophotonic solar thermophotovoltaic device. *Nat. Nanotechnol.* **9**, 126–130 (2014).

4. Bierman, D. M. *et al.* Enhanced photovoltaic energy conversion using thermally based spectral shaping. *Nat. Energy* **1**, 16068 (2016).

5. Ungaro, C., Gray, S. K. & Gupta, M. C. Solar thermophotovoltaic system using nanostructures. *Opt. Express* **23**, A1149–A1156 (2015).

6. Rephaeli, E. & Fan, S. Absorber and emitter for solar thermo-photovoltaic systems to achieve efficiency exceeding the Shockley-Queisser limit. *Opt. Express* **17**, 15145–15159 (2009).

7. Harder, N.-P. & W rfel, P. Theoretical limits of thermophotovoltaic solar energy conversion. *Semicond. Sci. Technol.* **18**, S151–S157 (2003).

8. Seyf, H. R. & Henry, A. Thermophotovoltaics: a potential pathway to high efficiency concentrated solar power. *Energy Environ. Sci.* **9**, 2654–2665 (2016).

9. Fraas, L. M., Avery, J. E. & Huang, H. X. Thermophotovoltaic furnace–generator for the home using low bandgap GaSb cells. *Semicond. Sci. Technol.* **18**, S247–S253 (2003).

10. Bianchi, M., Ferrari, C., Melino, F. & Peretto, A. Feasibility study of a Thermo-Photo-Voltaic system for CHP application in residential buildings. *Appl. Energy* **97**, 704–713 (2012).

11. Durisch, W. & Bitnar, B. Novel thin film thermophotovoltaic system. *Sol. Energy Mater.*

Sol. Cells **94**, 960–965 (2010).

12. Licht, A., Pfiester, N., DeMeo, D., Chivers, J. & Vandervelde, T. E. A Review of Advances in Thermophotovoltaics for Power Generation and Waste Heat Harvesting. *MRS Adv.* **4**, 2271–2282 (2019).

13. Zhiguang, Z., Enas, S., Yubo, S. & Peter, B. Solar thermophotovoltaics: reshaping the solar spectrum. *Nanophotonics* vol. 5 1 (2016).

14. Ferrari, C., Melino, F., Pinelli, M., Spina, P. R. & Venturini, M. Overview and Status of Thermophotovoltaic Systems. *Energy Procedia* **45**, 160–169 (2014).

15. Daneshvar, H., Prinja, R. & Kherani, N. P. Thermophotovoltaics: Fundamentals, challenges and prospects. *Appl. Energy* **159**, 560–575 (2015).

16. Sakakibara, R. *et al.* Practical emitters for thermophotovoltaics: a review. *J. Photonics Energy* **9**, 1 (2019).

17. Bauer, T. *Thermophotovoltaics*. *Green Energy and Technology* vol. 7 (Springer Berlin Heidelberg, 2011).

18. Werth, J. J. Thermo-photovoltaic converter with radiant energy reflective means. 3,331,707 (1963).

19. Swanson, R. M. Recent developments in thermophotovoltaic conversion. in *1980 International Electron Devices Meeting* 186–189 (IRE, 1980).

20. Omair, Z. *et al.* Ultraefficient thermophotovoltaic power conversion by band-edge spectral filtering. *Proc. Natl. Acad. Sci.* **116**, 15356–15361 (2019).

21. Wernsman, B. *et al.* Greater Than 20% Radiant Heat Conversion Efficiency of a Thermophotovoltaic Radiator/Module System Using Reflective Spectral Control. *IEEE Trans. Electron Devices* **51**, 512–515 (2004).

22. Fourspring, P. M., Depoy, D. M., Rahmlow, T. D., Lazo-wasem, J. E. & Gratrix, E. J. Optical coatings for thermophotovoltaic spectral control. 1–3 (2006).

23. Shemelya, C., Demeo, D. F. & Vandervelde, T. E. Two dimensional metallic photonic crystals for light trapping and anti-reflective coatings in thermophotovoltaic applications.

Appl. Phys. Lett. **104**, 1–4 (2014).

24. Burger, T., Fan, D., Lee, K., Forrest, S. R. & Lenert, A. Thin-Film Architectures with High Spectral Selectivity for Thermophotovoltaic Cells. *ACS Photonics* **5**, 2748–2754 (2018).

25. Lee, K., Shiu, K.-T., Zimmerman, J. D., Renshaw, C. K. & Forrest, S. R. Multiple growths of epitaxial lift-off solar cells from a single InP substrate. *Appl. Phys. Lett.* **97**, 101107 (2010).

26. Chancerel, F. *et al.* Epitaxial lift-off of InGaAs solar cells from InP substrate using a strained AlAs/InAlAs superlattice as a novel sacrificial layer. *Sol. Energy Mater. Sol. Cells* **195**, 204–212 (2019).

27. Forrest, S. R., Leheny, R. F., Nahory, R. E. & Pollack, M. A. $In_{0.53}Ga_{0.47}As$ photodiodes with dark current limited by generation-recombination and tunneling. *Appl. Phys. Lett.* **37**, 322–325 (1980).

28. Riben, A. R. & Feucht, D. L. Electrical Transport in nGe-pGaAs Heterojunctions†. *Int. J. Electron.* **20**, 583–599 (1966).

29. Peumans, P., Yakimov, A. & Forrest, S. R. Small molecular weight organic thin-film photodetectors and solar cells. *J. Appl. Phys.* **93**, (2003).

Chapter 7

Conclusion and Outlook

7.1. Conclusion

High performance optoelectronic devices made of III-V compound semiconductors are preferred over elemental semiconductors due to their bandgap tunability and strong light absorption. Thin-film optoelectronics on *unconventional surfaces* with superior mechanical flexibility, conformability, and integration with dissimilar materials are demanded in the current electronic market. In this thesis, we demonstrated novel fabrication techniques that transfer the III-V optoelectronic devices, especially high-performance photodetector focal plane arrays, from conventional bulky and rigid crystalline substrate, to lightweight, flexible, conformal, and non-developable surfaces without systematic performance degradation. In addition, we integrated an energy harvesting type of photodetector, an InGaAs-based thin-film thermophotovoltaic (TPV) cell, with dissimilar materials such as low index dielectrics and even air for enhanced out-of-band photon recycling, leading to a record-high TPV power conversion efficiency. The high performance III-V thin-film photodetectors on *unconventional surfaces* in this thesis unlock possibilities for future optoelectronic applications to think outside the conventional planar and lattice-matched architectures. In this chapter, we propose a new molecular beam epitaxy (MBE) system design, which is promising for increasing the epitaxial growth throughput and may thus reduce the production cost of optoelectronic devices using the technique of pipelining. We also

propose two TPV applications that have the potential to achieve highly efficient radiation power conversion and low-cost production.

7.2. A High Throughput, Linear Molecular Beam Epitaxy System

As discussed in Chapters 1 and 2, optoelectronic devices made of III-V compound semiconductors show superior performance compared to that made of elemental semiconductors such as Si and Ge. However, the production cost of these devices is prohibitive when compared with Si technologies. One significant differentiator is the high cost required to grow the epitaxial layers. Taking solar cells as an example, despite the high power conversion efficiency (*PCE*) of GaAs solar cells[1], their widespread adoption for solar-to-electricity energy conversion has been limited due to the exceptionally high cost of materials and epitaxial growth of the active solar cell layers. Here, we propose an MBE system design that has the potential to increase the epitaxial layer growth throughput using the technique of pipelining, thereby significantly reducing production costs. A linear transfer system sequentially transfers multiple substrate platens between interconnected growth positions within the chamber, thereby synchronously growing layers upon many wafers in the desired order and at the required thicknesses. The proposed linear MBE (LMBE) platform, therefore, has potential for the high-volume production of III-V optoelectronics with reduced cost.

A schematic top view of a conventional, production-scale MBE cluster tool is shown in Figure 7.1 (a)[2]. The system consists of a growth chamber, buffer chamber, and loading and unloading chambers. The substrate platen holds 7, six-inch diameter wafers. The platen is transferred into and out of the central distribution chamber via a manipulator arm. During a growth

cycle, the platen is mounted on a substrate heater in the growth chamber facing downwards towards the Knudsen cells containing the elemental source materials. Since there are several different layers comprising the device structure, multiple effusion cells are continuously heated, with the material flux from each cell controlled by individual shutters.

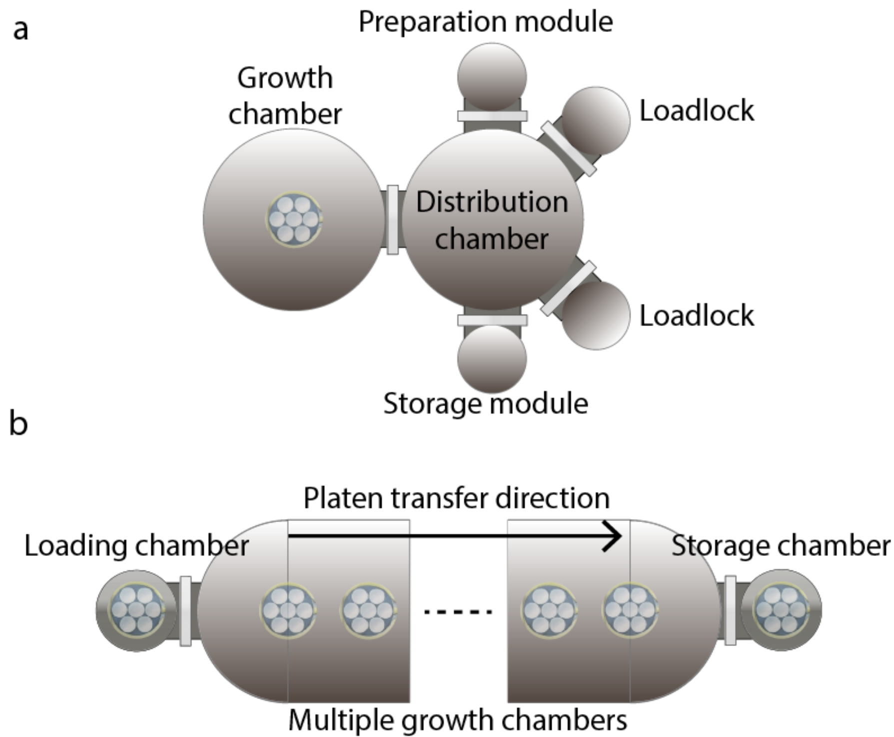

Figure 7.1: Schematic illustration of a conventional production scale MBE vs. a linear MBE. (a) Schematic illustration of a top view of a conventional production scale MBE machine comprising a distribution chamber, growth chamber and small peripheral chambers. (b) Proposed linear MBE machine with expanded growth chamber.

Figure 7.1 (b) shows a top schematic view of the proposed LMBE system comprising a main chamber with multiple, interconnected growth positions along a row, and loading and unloading chambers at each end. The substrate preparation and storage chambers can also be placed in-line or vertically relative to the loading and unloading chambers. The desired epitaxial structure is realized by growing layers of similar thicknesses and growth times at each position to

prevent delays incurred by the entire line while a particularly thick layer is grown. For example, if the typical layer thickness required in the device is *d*, but the active region thickness is larger, e.g. 3*d*, then each of the layers are grown at separate positions within the line, whereas the active region is grown by consecutive steps at three adjacent positions. Thus, the throughput (*TP*) of this example line is: $TP = N/(d/r+t_{tr})$, where r is the rate of growth of a layer (in µm/h), $N = 7$ is number of wafers per platen, and t_{tr} is the cumulative transfer time from loading, to transfer between growth sections, to unloading. Since each growth position is used to grow layers of approximately equal thickness, *N* wafers are produced at each the position.

Substrate platens with the same nominal size as used in a conventional MBE system are transferred in a "bucket brigade" fashion from the loading chamber, through the several growth positions, to the unloading chamber. After each layer growth, the substrates are transferred in unison from their current positions to the next position, and the growth cycle starts again. The complete multilayer structure is obtained after a platen transits the length of the system from loading to unloading. This configuration allows for increased utilization of effusion cells, and replaces multiple manipulator arms with a simple linear transfer system. Each growth position consists of a substrate heater with only those effusion cells required for the growth of a particular layer. As a consequence, the total chamber volume occupied by a growth section is smaller than that of a conventional MBE system. Therefore, supporting equipment such as pumps and electronics is shared between multiple sections.

Conventional MBE systems use a complex manipulator arm to transfer the substrate platen between the main growth and buffer chambers. The LMBE eliminates the need for a manipulator arm between growth sections, since platen transfer occurs via a linear movement, thereby reducing machine cost and footprint. Figure 7.2 (a) shows a schematic of the linear transfer mechanism. A

rack-and-pinion track transfers platens between growth positions distributed along the system length (the x-axis). Platen holders, or tabs, are placed in the rack at intervals equal to the distance between growth positions. Platens have protrusions, or "ears" that fit into the tabs attached to the rack. A rotating substrate heater whose axis is along the z-direction is located each growth position. A schematic of the substrate heater with sidewall openings and a substrate platen with ears is shown in Figure 7.2 (b).

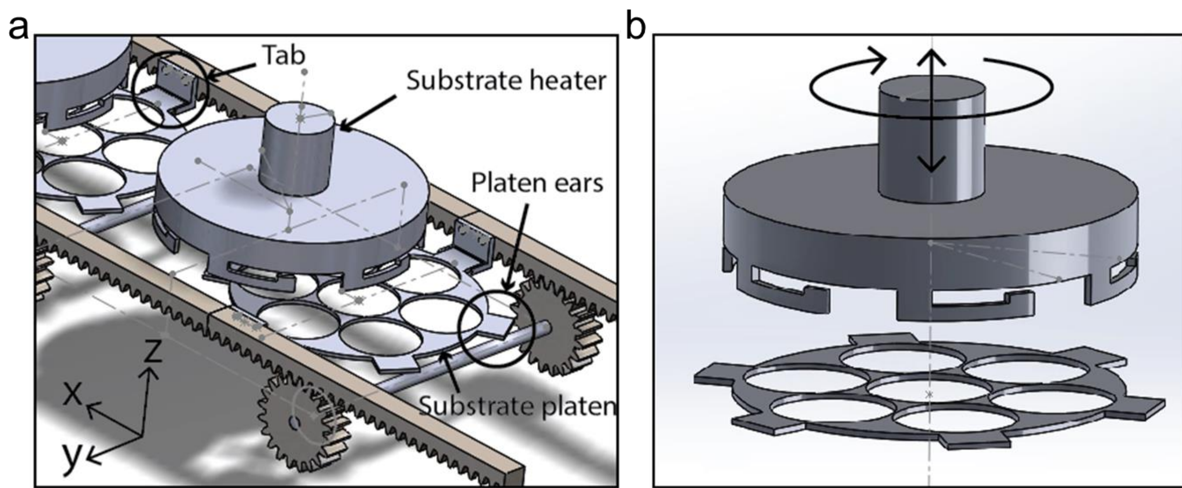

Figure 7.2: Schematic illustration of a rack and pinion linear transfer system.
(a) Schematic illustration of a rack and pinion linear transfer system with tabs attached to the rack and substrate heaters at growth positions. (b) Substrate heater and platen, showing the range of motion of the heater for picking up and laying down of the platen.

Vertical and rotational movements of the substrate heater lock the platen into the heater by holding the platen ears in the sidewall openings. Unlocking the platen from the heater entails the reverse of the locking sequence. During growth, substrate platens are held by the substrate heaters. The tabs are located at the midpoints of the growth positions, as shown in Figure 7.3 (a). After each layer is grown, the "transfer in" step commences. The rack moves in the *-x* direction by half the distance between growth positions. Then the $(N+1)^{\text{th}}$ tab is aligned with N^{th} growth position

(Figure 7.3 (b)). Substrate platen heaters move down along the *z*-axis, leave the platen at the tabs by unlocking, and then retract. A new substrate platen is transferred from the loading chamber to the first platen holder, which is now empty. In the final step – "transfer out"— the rack moves in the +*x* direction by the distance between each growth position until the first platen tab is aligned with first growth position, as shown in Figure 7.3 (c). Once growth is complete, the platen at the end of the rack is transferred to the unloading chamber, and the rack moves in the -*x* direction by half the distance between growth chambers, returning to the first step of the growth cycle.

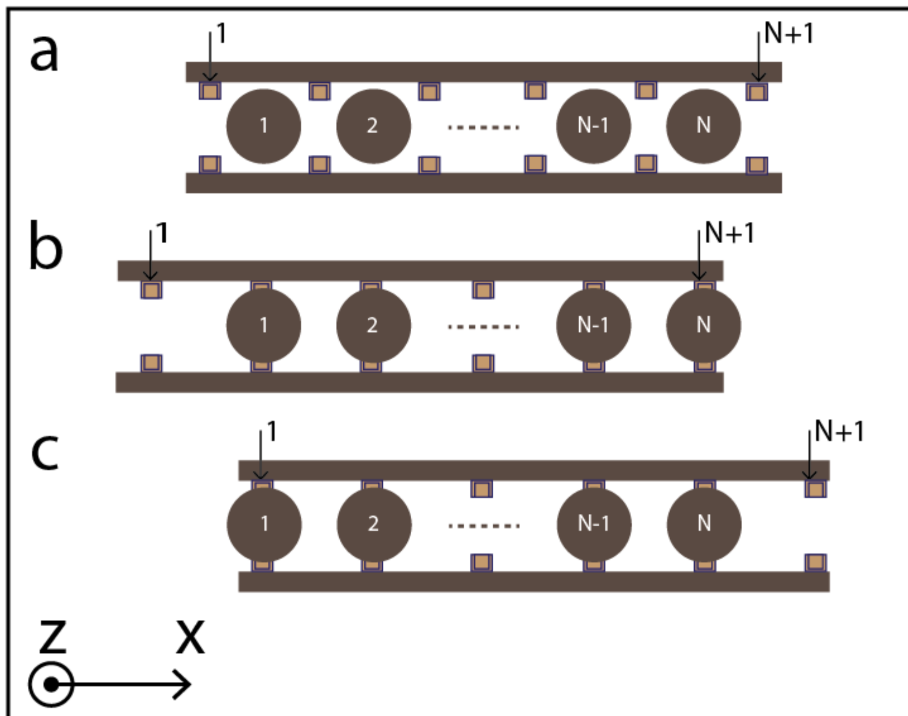

Figure 7.3: Schematic illustration of a linear transfer system.
Schematic illustration of a linear transfer system, with rack at (a) the growth position, (b) the transfer into the growth position, shifted by half the distance between growth positions in the backwards direction, and (c) the transfer-out position, shifted by the distance between growth positions in the forward direction.

The number of growth positions is determined by the particular structure being grown. An example inverted GaAs single junction photovoltaic cell used for ND-ELO processing is shown in

Figure 7.4 (a). The structure can be divided into three different sections: sacrificial and protection layers used to separate the epitaxy from the parent wafer, the emitter/front contact, and the base/back contact layers. The ND-ELO structure comprises a 425 nm thick sacrificial-plus-protection layer structure (blue rows). The emitter/front contact (green rows) layers are 335 nm thick, and the 2.82 μm thick base/back contact layers (yellow and orange rows) are divided into 6 identical, 470 nm thick sections to equalize the time spent growing each layer in the sequence. The growth chamber thus requires 8 growth positions starting with AlAs and InGaP sacrificial and protection layers, then the emitter layer, and 6 base layers. Figure 7.4 (b) shows the LMBE chamber configuration and the 30 effusion cells required for this single-junction device.

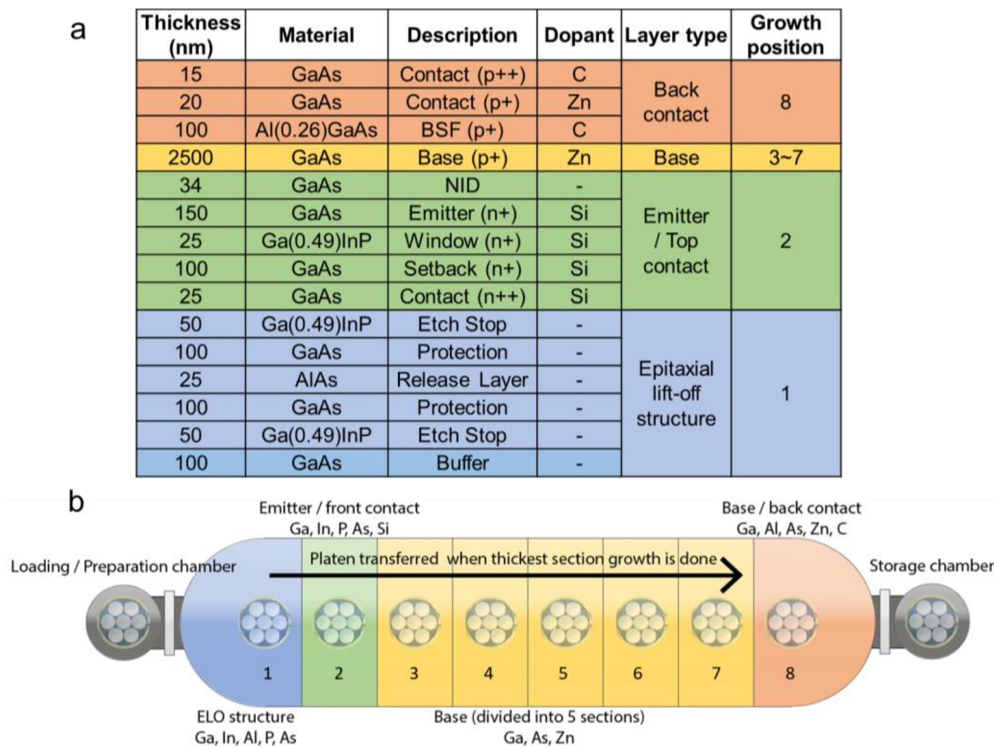

a

Thickness (nm)	Material	Description	Dopant	Layer type	Growth position
15	GaAs	Contact (p++)	C	Back contact	8
20	GaAs	Contact (p+)	Zn		
100	Al(0.26)GaAs	BSF (p+)	C		
2500	GaAs	Base (p+)	Zn	Base	3~7
34	GaAs	NID	-	Emitter / Top contact	2
150	GaAs	Emitter (n+)	Si		
25	Ga(0.49)InP	Window (n+)	Si		
100	GaAs	Setback (n+)	Si		
25	GaAs	Contact (n++)	Si		
50	Ga(0.49)InP	Etch Stop	-	Epitaxial lift-off structure	1
100	GaAs	Protection	-		
25	AlAs	Release Layer	-		
100	GaAs	Protection	-		
50	Ga(0.49)InP	Etch Stop	-		
100	GaAs	Buffer	-		

Figure 7.4: An analysis of an inverted single junction GaAs photovoltaic cell.

(a) An inverted single junction GaAs photovoltaic cell structure used for analysis. The sacrificial layer used in epitaxial lift off with protection layers (blue), emitter and front contact layers (green), base layers (yellow) and back contact layers (orange) are indicated. (b) Schematic of linear MBE system chamber configuration designed for inverted single junction GaAs photovoltaic cells with the number of effusion cells at each growth position.

The key improvement of the LMBE compared to conventional MBE is that for all of components employed in the machine, the cost of ownership is reduced, and the utilization efficiency is improved through the technique of pipelining growth. A limitation of the LMBE architecture is that its flexibility in growing a variety of different structures is restricted, since each growth position is optimized to achieve a pre-determined layer composition within a designated device structure. Changing the number of growth positions (and hence the total number of layers) requires an extension of the main chamber. Flexibility can be improved by inserting blank effusion cells and growth sections along the system length that can be activated as needed at a low incremental expense.

7.3. Tandem Thermophotovoltaic Cell

As described in Chapters 5 and 6, it is possible for TPV cells to achieve *PCE* exceeding 50% and inserting an embedded air-bridge reflector can improve the *PCE* by a significant amount. The *PCE* of the air-bridge TPV cell, however, is still limited to ~30% at relatively high current density due to series resistance R_s loss. To overcome this limitation, making tandem TPV cells is a more advantageous approach to high power densities since as the voltage increases, the current, and consequently the R_s loss decrease.

A tandem TPV cell structure can be achieved by utilizing a high bandgap (0.95 eV) InGaAsP sub-cell and a low bandgap (0.74 eV) InGaAs sub-cell. Such tandem structures have been demonstrated in solar PV applications[3], but remain to be studied in a thin-film TPV device. The InGaAs sub-cell consists of an InP/$In_{0.53}Ga_{0.47}As$ heterojunction, while the InGaAsP sub-cell uses an InGaAsP homojunction. These two sub-cells are connected through a degenerately doped InGaAs tunnel junction. Preliminary optimization suggests that the thicknesses of InGaAs and

InGaAsP should be ~800 nm and ~2.7 µm to achieve current matching in the tandem. This tandem structure can be readily integrated with the ND-ELO process.

Here, we propose a tandem TPV structure that has the potential to achieve high efficiency under high power density conditions. The designed epitaxial structure of this tandem TPV cell is shown in Figure 7.5. First, a 100 nm InP buffer is grown on a Zn-doped InP substrate, followed by a 50 nm InGaAs protection layer. Then, a 5 nm lattice-mismatched AlAs sacrificial layer is grown. The $In_{0.69}Ga_{0.31}As_{0.67}P_{0.33}$ sub-cell is then grown followed by an InGaAs tunnel junction. Finally, InP/$In_{0.53}Ga_{0.47}As$ sub-cell is grown on top. The growth of the all-InGaAs device will follow a similar procedure, expect that the first sub-cell will also consist of InP/$In_{0.53}Ga_{0.47}As$.

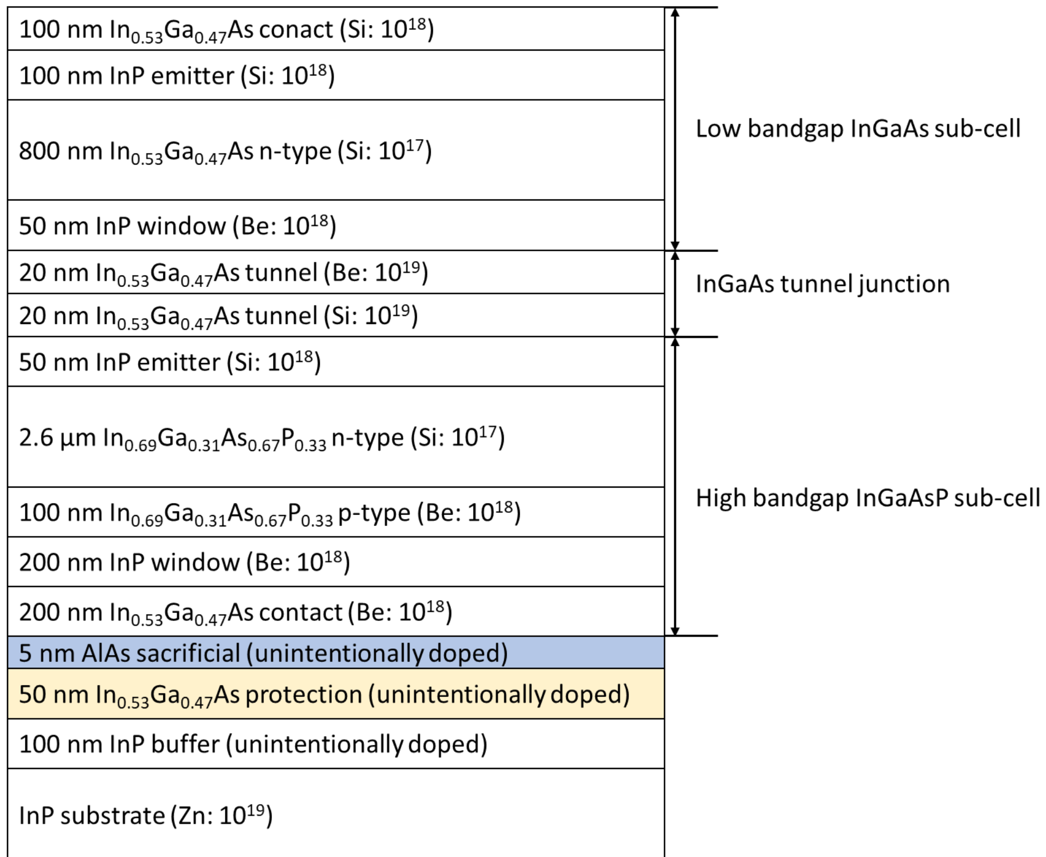

Figure 7.5: InGaAsP / InGaAs tandem TPV design.

After the growth, the air-bridge supports are patterned on top of the epitaxial wafer. The wafer is then cold-weld bonded to an external host substrate coated with Au. The entire sample is soaked in dilute HF to etch the AlAs sacrificial layer and epitaxially lift off the tandem TPV cell structure from its parent InP substrate. It has been demonstrated that the lattice-mismatched AlAs does not impair the device performance fabricated from the lifted-off active layer grown above, as long as the AlAs thickness is kept thin enough[4]. After liftoff, the active epi-layers can be fabricated into tandem TPV cell, and the parent InP substrate can be recycled by simply wet etch the InGaAs protection layer to get a pristine InP surface for the regrowth[5]. The quality of the recycled parent wafer can also be improved by employing InGaAs/InAlAs superlattice protection layers[6].

7.4. Thin-Film Air-Bridge Si Thermophotovoltaic Cell

As discussed in Chapter 6, within the common range of source temperatures of a TPV system, out-of-band (OOB) loss dominates with increasing bandgap. However, when OOB reflectance approaches unity, this dependence vanishes, suggesting that the cell design becomes relatively insensitive to the bandgap (E_g) of active materials and temperature of emitters. Thus, the nearly perfect reflectance of the air-bridge design potentially allows for the exploitation of low-cost semiconductors such as Si in TPV cells while maintaining a high spectral efficiency (*SE*) at relatively low emitter temperatures.

Here, we simulate the spectral properties, especially the OOB reflectance of a thin-film air-bridge TPV cell using 2 μm Si epilayer as active absorption material (Figure 7.6). As weighted by the 1500 K blackbody emission spectrum, the average OOB power reflectance of this TPV cell is calculated for various air gap thicknesses as shown in Table 7.1. The maximum OOB power reflectance reaches 99.46% when air cavity thickness is 500 nm.

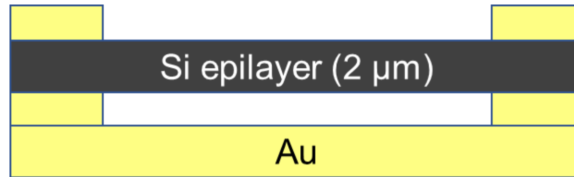

Figure 7.6: Schematic of an air-bridge Si TPV cell.

Table 7.1: Calculated out-of-band power reflectance of the air-bridge Si TPV cell with 2 μm Si epi for various air cavity thicknesses when operated using a 1500 K blackbody source.

Air cavity thickness (nm)	Out-of-band power reflectance (%)
100	98.06
200	98.83
300	99.21
400	99.40
500	99.46
600	99.38
700	99.31
800	99.25
900	99.20
1000	99.17

The maximum power reflectance is 99.46% when air cavity thickness is 500 nm.

The simulated OOB (E_g <1.12 eV) absorption spectrum of the air-bridge TPV cell with 500 nm air gap and 2 μm Si epilayer is presented in Figure 7.7. Assuming a perfect in-band absorption, the spectral efficiency of this air-bridge Si TPV is $SE = 89.95\%$.

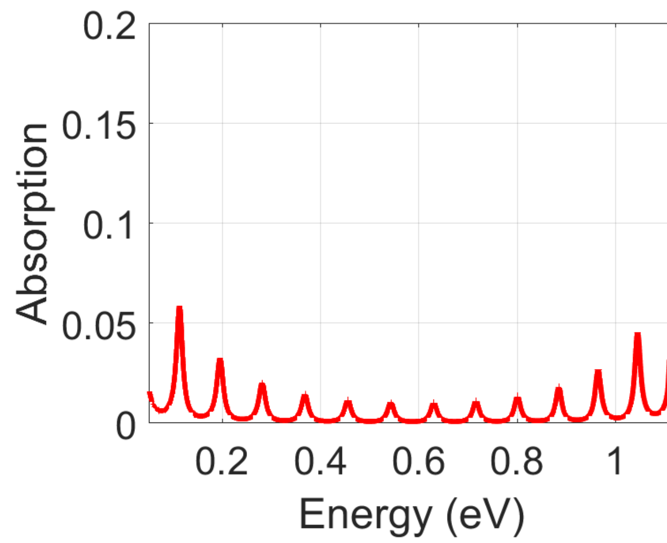

Figure 7.7: Simulated spectral properties of the air-bridge Si TPV cell with 2 µm Si epi and 500 nm air gap.

Out-of-band (OOB, $E < E_g = 1.12$ eV) absorption of the air-bridge Si TPVs.

CHAPTER 7

Bibliography

1. Green, M. A. *et al.* Solar cell efficiency tables (Version 55). *Prog. Photovoltaics Res. Appl.* **28**, 3–15 (2020).

2. O'Steen, M., Readinger, E., Doran, M. & Hanser, D. *Systems and technology for production-scale molecular beam epitaxy*. *Molecular Beam Epitaxy* (Elsevier, 2013).

3. Zhao, Y. *et al.* InGaAsP/InGaAs tandem photovoltaic devices for four-junction solar cells. *J. Semicond.* **36**, 044011 (2015).

4. Shen, G. & Fan, Z. *Flexible Electronics*. (World Scientific Publishing Co, 2016).

5. Lee, K., Shiu, K.-T., Zimmerman, J. D., Renshaw, C. K. & Forrest, S. R. Multiple growths of epitaxial lift-off solar cells from a single InP substrate. *Appl. Phys. Lett.* **97**, 101107 (2010).

6. Chancerel, F. *et al.* Epitaxial lift-off of InGaAs solar cells from InP substrate using a strained AlAs/InAlAs superlattice as a novel sacrificial layer. *Sol. Energy Mater. Sol. Cells* **195**, 204–212 (2019).